Microfabrication of Photonic Devices for Mid-Infrared Optical Applications

James Matthew Harold Dodd Morris

Submitted for the degree of Doctor of Engineering

Heriot-Watt University

Institute of Photonics and Quantum Sciences

School of Engineering and Physical Sciences

September 2018

Abstract

This thesis details research into the microfabrication of photonic devices for mid-infrared optical applications using the technique of ultrafast laser inscription. A diverse range of devices and materials is explored, including the first fabrication and development of an ultrafast laser inscribed mid-infrared waveguide laser source in thulium-doped sesquioxide ceramic gain media. The source produced 81 mW of output power at 1942 nm with a maximum slope efficiency of 9.5% demonstrating progress towards compact, low-threshold and efficient ultrafast laser written waveguide laser sources near 2 μm with the potential for high pulse repetition rate and ultrashort pulse operation.

Also shown is the first demonstration of ultrafast laser inscription enabled selective chemical etching of chalcogenide glass. Investigations into the etching of modified regions in gallium lanthanum sulphide glass showed they could be etched at a rate ~13.3 times greater than the un-modified bulk. This result was explored further as a potential route to the production of optofluidic sensors for gas, liquid chemical or biomedical samples. The first demonstration and characterisation of ultrafast laser written waveguides in the chalcogenide glass GASIR-1 is also described. The waveguides were employed for chip scale supercontinuum generation producing the broadest and deepest Infrared supercontinuum from an ultrafast laser inscribed waveguide to-date, spanning ~4 μm from 2.5 to 6.5 μm, which has applications in remote sensing. Finally, the design, build and commissioning of an advanced laser processing setup suitable for ultrafast laser inscription is also detailed.

To Marion

As an aside and before my acknowledgements, I would like to briefly comment on the merits of thesis writing whilst looking after a dog, in this instance our Dachshund called Dorris. Her complete lack of understanding or interest in letting me work helped keep things in perspective when writing got particularly tough.

Acknowledgements

Firstly, I would like to thank my supervisors, Professor Ajoy Kar and Doctor Henry Bookey for the chance to carry out the work described in this thesis. Their encouragement, guidance and support have been much appreciated.

I would also like to thank all the colleagues, classmates and friends that I have met throughout my Doctoral studies: from my classmates at St. Andrews, past and present members of the Nonlinear Optics Group at Heriot Watt, colleagues at the Fraunhofer Centre For Applied Photonics, to my MBA course classmates from the Edinburgh Business School. You have all made a positive contribution to my time as an Engineering Doctorate student and helped me to get the most of this opportunity. I would like to extend specific thanks to Doctor Adam Lancaster for his advice on waveguide lasers and optical characterisation, Doctor Mark McKenzie for showing me the ropes on chemical etching, areobasic code and microfluidics, Doctor Giorgos Demetriou for introducing me to ultrafast laser inscription, optical parametric amplifier systems and the Z-scan technique, and Neil Stevenson for sharing his expertise in mid-infrared solid-state lasers.

I wish to thank my collaborators at the Opto-electronics Research Centre, in particular the group headed by Professor Dan Hewak, including Andrea Ravagli and Christopher Craig, who fabricated the doped and un-doped gallium lanthanum sulphide samples studied in this work. I would also like to thank collaborators at the Technical University of Denmark, specifically the group headed by Professor Ole Bang, including Doctor Christian Petersen, for the dispersion measurements on GASIR-1 samples and assisting with waveguide supercontinuum experiments. I also thank John Franks from Umicore for providing the GASIR-1 samples.

I would like to thank family and friends for their encouragement and support, particularly my parents, Charles and Susan, and my brother, Paul.

Lastly and most importantly I wish to thank my wife Marion for the understanding, patience and unwavering support which she has given me for as long as we've known each other. Without her I would not be where I am today and undoubtedly this thesis would not have been written.

ACADEMIC REGISTRY

Research Thesis Submission

Name*:*			
School:			
Version: *(i.e. First, Resubmission, Final)*		Degree Sought:	

Declaration

In accordance with the appropriate regulations I hereby submit my thesis and I declare that:

1) the thesis embodies the results of my own work and has been composed by myself
2) where appropriate, I have made acknowledgement of the work of others and have made reference to work carried out in collaboration with other persons
3) the thesis is the correct version of the thesis for submission and is the same version as any electronic versions submitted*.
4) my thesis for the award referred to, deposited in the Heriot-Watt University Library, should be made available for loan or photocopying and be available via the Institutional Repository, subject to such conditions as the Librarian may require
5) I understand that as a student of the University I am required to abide by the Regulations of the University and to conform to its discipline.
6) I confirm that the thesis has been verified against plagiarism via an approved plagiarism detection application e.g. Turnitin.

* *Please note that it is the responsibility of the candidate to ensure that the correct version of the thesis is submitted.*

Signature of Candidate*:*		Date:	

Submission

Submitted By *(name in capitals):*	
Signature of Individual Submitting:	
Date Submitted:	

For Completion in the Student Service Centre (SSC)

Received in the SSC by *(name in capitals):*			
1.1 Method of Submission *(Handed in to SSC; posted through internal/external mail):*			
1.2 E-thesis Submitted (**mandatory for final theses)**			
Signature:		Date:	

Please note this form should be bound into the submitted thesis.

Table of Contents

Chapter 1 Introduction 1

1.1 Background 1

1.2 Motivation 10

1.3 Thesis Summary and Outline 11

Chapter 2 Light-Matter Interactions and Optical Materials 14

2.1 Waveguides 14

2.2 Nonlinear Light-Matter Interactions 18

2.2.1 Non-Resonant Nonlinear Light-Matter Interactions 18

2.2.2 Supercontinuum generation 21

2.2.3 Resonant Nonlinear Light-Matter Interactions 25

2.3 Ultrafast Laser Inscription 28

2.3.1 Overview 28

2.3.2 Physical Process 29

2.3.3 Waveguides and Inducing Refractive Index Change 31

2.3.4 Micro-channels and Selective Etching 33

2.4 Material Properties 37

2.4.1 Chalcogenides 37

2.4.2 Sesquioxides 41

2.5 Summary 44

Chapter 3 Laser Processing Rig 45

3.1 ULI Setup Considerations 45

3.2 System Hardware 51

3.2.1 Laser Source 53

3.2.2 Beamline 54

3.2.3 Positioning 57

3.3 Software....58
3.3.1 Original Equipment Manufacturer Software....59
3.3.2 Custom System Control Software....59
3.4 System Commissioning....63
3.5 Summary....66

Chapter 4 Germanium Arsenic Selenide Waveguides for Mid-IR Integrated Optics....67

4.1 Mid-IR Chalcogenide Glass Waveguides....67
4.2 GASIR-1 Waveguide Fabrication and Characterisation....71
4.3 The Z-scan Technique....75
4.4 Mid-IR Z-scans of GASIR-1....78
4.5 Waveguide Dispersion....82
4.6 Waveguide Supercontinuum Generation....83
4.7 Summary....86

Chapter 5 Micro-structuring of Gallium Lanthanum Sulphide for Mid-IR Optofluidics....87

5.1 Micro and Optofluidics....87
5.1.1 ULI fabricated Optofluidics....89
5.1.2 Gallium Lanthanum Sulphide as a Substrate for Mid-IR Optofluidic Devices....91
5.2 Chalcogenide Glass Wet Chemical Etching....93
5.3 Gallium Lanthanum Sulphide Selective Etching Trials....95
5.4 Optofluidic Device Design....99
5.5 Device Inscription and Etching....101
5.6 Summary....104

Chapter 6 Waveguides in Thulium-doped Lutetium Oxide for Compact Mid-IR Lasers....105

6.1 Basic Principles of Laser Operation....105
6.2 ULI waveguide lasers....110

6.3 Waveguide Fabrication and Passive Characterisation 114
6.4 Waveguide Laser Results 118
6.5 Summary 124

Chapter 7 Conclusions and Future Work 125

7.1 Introduction 125
7.2 Conclusions 125
7.3 Future Work 128
7.3.1 Multi-octave Spanning ULI Waveguide Supercontinuum Sources 128
7.3.2 Broadband Mid-IR Optofluidic Sensors 129
7.3.3 Novel Mid-IR Sesquioxide ULI Waveguide Lasers 130
7.4 Closing remarks 131

References 132

Appendix A Laser Processing Rig User Guide A-1

A.1 Overview A-1
A.2 Setup A-2
A.3 Usage A-9
A.4 Start Next Run or Shutdown A-11

List of Tables

Table 2-1 Nonlinear optical constants for a selection of chalcogenide glasses. Where λ_m is the wavelength used for measurement, n_0 and n_2 are the linear and nonlinear refractive indices respectively, β is the two-photon absorption coefficient and FOM is the figure of merit given by the ratio $n_2 / \beta\lambda$ which parametrises the nonlinear phase shift attainable over one two-photon absorption length. Experimental uncertainty for the measurements where given: a ± 18 %, b ± 3 nm, c ± 1.6 %, d ± 17 %, e ± 1.7 %. 39

Table 2-2 Summary of important properties of lutetia, scandia, yttria and yttrium aluminium garnet for photonics applications. Superscripts refer to dopant ions where: a - thulium-doped, b holmium-doped, c - average across common rare earth dopants. Doping concentrations are stated in atomic percentages signified using %at. notation. * - values correspond to double the atomic percentage doping in sesquioxides as this provides a comparable dopant ion density.....42

Table 3-1 Summary of key components in each system section. All transmissive optics coated for low loss at 1030nm.Components from Thorlabs unless otherwise indicated. 52

Table 5-1 Summary of the bulk and maximum modified region etch rates for the collection of etchants tested. These were used to determine the etchants' selectivity and hence suitability for FLICE fabrication techniques. Diisopentylamine, morpholine and nitric acid are listed by their chemical formulas which are $C_{10}H_{23}N$, C_4H_9NO and NHO_3 respectively. Also included are the results from etching trials of neat amines, i.e. 100%, amine etchants with no solvent. 98

Table 6-1 Summary of the guiding characteristics of inscribed track waveguides in Tm:Lu_2O_3 for different pulse energy and track separation combinations, where SM signifies single mode guiding behaviour and MM signifies multi-mode guiding behaviour. 118

List of Figures

Figure 1-1 Mid-IR transmission spectra of propan-1-ol and propan-2-ol, and a simulated transmission spectra of the atmosphere. The red box marks the functional group region and the green box marks the molecular fingerprint region. Propan-1-ol and propan-2-ol spectral data provided by the National Institute of Standards and Technology (NIST) and begins at 2.5 μm [9]. Atmospheric transmission spectra was simulated using the Atmospheric Transmission software tool (ATRAN) with the High-resolution Transmission molecular absorption database (HITRAN) [10]. Simulation output was smoothed using a moving average filter for clarity. 3

Figure 1-2 RHS: A generalised flow diagram of the process steps for mid-IR thin film channel waveguide fabrication. Starting with a substrate, each device layer can be fabricated by an appropriate sequence of device layer and masking layer deposition, patterning, developing and striping. Numerous sequences are needed if multiple final device layers are required, for instance in the case of a buried channel waveguide with top and bottom cladding layers. LHS: shows a schematic for the creation of air clad $GeTe_4$ thin-film channel waveguides following the procedure described in ref [26]. 8

Figure 2-1 Nonlinear absorption processes in the opposite extremes of high photon energy low field strength, (a) tunnelling process, and low photon energy high field strength, (b) MPA process. VB signifies the valence band and CB signifies the conduction band. Adapted from [48]. 28

Figure 2-2 Avalanche ionisation - the two-step process of free carrier absorption followed by impact ionisation. VB signifies the valence band and CB signifies the conduction band. Adapted from [48].....30

Figure 2-3 Laser inscription of guiding structures with magnified inserts of waveguide cross-sections for (a) type I, (b) type II, and (c) depressed cladding waveguide structures. The guiding region for each type is indicated using red dashed lines. It is important to remember that the achievable modification type is material dependent as well as a function of fabrication parameters. Therefore, it is often not possible to fabricate all three types of waveguides in the same sample. Adapted from [62]. 33

Figure 2-4 Top: Asymmetric field enhancement at two locations on a nanoplasma under the influence of the laser electric field, E. The relative permittivity, ε, is the ratio of the real part of the nanoplasma permittivity to the dielectric function of the medium that

surrounds the nanoplasma. N_e is the plasma density and N_{cr} is the critical plasma density. For an under-dense plasma, i.e. $N_e<N_{cr}$, field enhancement occurs as seen in the central graph. Bottom: Evolution of nanoplasmas into nanoplanes. Randomly distributed under-dense nanoplasma droplets (droplet size is a few tens of nanometres) grow asymmetrically in the presence of the laser field over hundreds of laser pulses to become ellipsoidal and finally flatten and merge to become micrometer sized nanoplanes. Adapted from [71].....36

Figure 2-5 Infrared transmission for bulk glass samples of SiO_2 (fused silica), ZBLAN (a multicomponent fluoride glass) and representative chalcogenide glasses. Silicon, not shown in this figure, has a long wavelength cut-off at around 7 μm. Reduction in the overall transmission for heavier chalcogen containing glasses is tied to Fresnel losses due to their higher refractive indices.....38

Figure 3-1 Block diagram of a generic ULI setup, where: S - shutter, HWP - half-wave plate, PBS - polarisation beam splitter, BD - beam dump, BS - beam splitter, D - detector, AOM - acousto-optic modulator, QWP - quarter-wave plate, L - lens, SUB - substrate material, TS - translation stages. Green box contains power control optics and blue box contains polarisation control optics. Adapted from [99]. 47

Figure 3-2 Modelling of beam profiles and energy distribution for focussed beams into glass with n = 1.54 using a microscope objective with NA = 0.46 and 500 μm wide slit. (a) beam evolution near focus not using slit, (b) energy distribution in YZ plane not using slit (c) beam evolution near focus using slit, (d) energy distribution in YZ plane using slit where x corresponds with the direction of the beam translation (parallel axis). Adapted from [106]. 50

Figure 3-3 Block diagram of the laser processing rig beamline, with components: HWP - half wave plate, PBS - polarising beam splitter, BD - beam dump, QWP - quarter wave plate, PS - periscope, OT – optics turret. Green and blue boxes group components together into the system sections listed in Table 3-1, where: POW - power control, POL – polarisation control, TEL – telescope, IMG – imaging and INS – inscription head.....54

Figure 3-4 Waveplate calibration results. a) measurements and fit for power waveplate, b) measurements and fit for circular polarisation waveplate. In both instances a good fit to the adapted versions of Malus's law was observed. 55

Figure 3-5 A generalised flow diagram of the event driven state machine design used for the FCAP ULI control software. Upon program launch the initialise state runs and once complete the program proceeds to the wait for event state. The next state to execute is triggered by user input either from interactions with the FCAP ULI control software front panel or calls from running Aerobasic programs. Upon state execution the program returns to the wait for event state in all instances except for the stop state. 60

Figure 3-6 Barebones block diagram for an event driven state machine in LabVIEW showing the wait for event state and the case selector option for when a front panel button called “Call User State 1” is pressed. The outermost structure is a while loop so that the program will run continuously until the stop state is executed. The stop state passes a Boolean true constant to the stop condition of the while loop, seen in the bottom right of the diagram to end the program. The coloured wires and associated shift registers allow data to passed between states and around the main program loop where pink, blue and yellow colour coding refers to strings, integer and error data types respectively. 61

Figure 3-7 Excerpt from an Aerobasic program demonstrating the syntax for setting the inscription power and polarisation state, signalling for the change to be made and waiting on confirmation that the change has been implemented. 63

Figure 3-8 Acoustic resonator device at different stages of fabrication. Top: Device design illustrated by simulated stage motions. Only the outer edges of the resonator tube and tap sections are inscribed to vastly reduce the processing time; because of this, these sections fall out as rods. Bottom right: zoomed in top down view of tap section as inscribed. Bottom left: side view of tap section after device etching. 64

Figure 3-9 Sample of waveguide structures written to test system performance. Top: Type I waveguide array in GLSSe with varying scan number to change core region width. Bottom: Type II cladding waveguide structures written in fused silica.....65

Figure 4-1 Left: Supercontinuum spectrum generated with a 410 nJ incident pulse energy. The location and width of the input pulse spectrum is indicated by the broken red line. The pulse is centred at 4.26 μm near to an atmospheric CO_2 absorption peak. Right: The GLS waveguide end facet and scale bar is shown in (b) and the corresponding mode image of the below threshold pump at 4.26 μm is shown in (c) with the same scale [39]. 69

Figure 4-2 Transmission microscope images showing the resulting material modification from two fabrication parameter sweeps. a) single line scan results for increasing pulse energies from 34 to 90 nJ. b) The array of multi-scan waveguides used in this work. Written with identical laser parameters but increasing scan number to vary the waveguide core width. In both cases the inscription beam is incident from above. 72

Figure 4-3 Experimental setup for initial waveguide testing, waveguide losses and guided mode dimensions. a) Setup where: Mx, silver mirrors; VA, reflective variable ND filter; BD, beam dump; L1 and L2, BBAR-coated ZnSe objectives; WUT, waveguide under test; FM, flip mirror. Blue dotted box signifies components mounted on waveguide alignment workstation. b) Waveguide losses including coupling and propagation loss for WG2-7. c) Waveguide $1/e^2$ MFD measurements for x and z directions for WG2-7 with an insert showing the near field mode image of WG5. 74

Figure 4-4 Pictorial representation of an open Z-scan measurement for a material exhibiting a positive nonlinear refractive index, adapted from [132]. a) upstream and far from the focal region; b) upstream near the focal region; c) at the focus; d) downstream near the focal region; and e) downstream and far from the focal region. Near the focus the sample acts as a positive lens leading to a decrease in aperture transmission when the sample is upstream and near the focus, and an increase in aperture transmission when the sample is downstream and near the focus. 76

Figure 4-5 Experimental setup for Z-scan measurements where: L1 and L2, achromatic doublet lens; PH, pinhole; VA, reflective variable ND filter; BD, beam dump; Mx, silver mirror; BSx, beam splitter; PDx, photodetector; FM, flip mirror; L3, CaF_2 lens, SUT, sample under test; and ZS, Z-stage. Control electronics includes the Z-stage motion controller, custom peak-hold unit for photodetector output, function generator and control PC with DAC. 79

Figure 4-6 Z-scan measurement results. a) Representative Z-scan trace taken using 10 nJ pulses centered at 2 μm with a linear aperture transmittance of 50% and fit using the closed aperture Z-scan formula. b) Plot of measured n_2 values vs wavelength including errors (± 15%). c) Transmission spectra showing band edge with a zoomed in view insert showing the absorption tail, includes Fresnel losses. 81

Figure 4-7 Dispersion results and analysis. Top: Measured dispersion of different waveguides. The lines represent the mean of four measurements with error bars indicating

measurement uncertainty. The insert shows a zoomed in view on the long-wavelength edge of the measurement, indicating a ZDW around 4.44 μm and 4.56 μm for WG1 and WG3, respectively. Bottom: Windowed Fourier transform analysis of interference spectra from a) WG1 and b) WG5, which demonstrates that WG5 exhibits multimode beating below 1.7 μm. In this particular example the higher-order mode is dominating at short wavelengths making it difficult to measure the dispersion in this region.....83

Figure 4-8 Supercontinuum measurement setup and results. a) Setup where: Mx, gold mirrors; FSL, fused silica lens; DFG-X, DFG crystal; BFL, BF2 lens; LPx, long pass filters; WP, waveplate; POL, wire grid polariser; FMx, flip mirrors; L1 and L2, BBAR-coated ZnSe objectives or uncoated CaF2 lens; WUT, waveguide under test; MCT, MCT detector. Blue dotted box signifies components mounted on waveguide alignment workstation. b) Broadest supercontinuum measured spanning ~ 4 m at -20 dB points. Produced by pumping WG7 with 130 nJ pulses coupled and collected with CaF2 lens set. Input pulse spectrum is also shown. c) Evolution of supercontinuum with input pump power for WG5 with ZnSe objective set. Broadening is seen from pulse energies as low as 3 nJ. 85

Figure 5-1 LoC cell counter using 3D hydrodynamic focusing and optical detection. (a) Schematic rendering of microfluidic circuit. (b) Microscope image of the fabricated microfluidic circuit. (c) Zoomed in view demonstrating flow confinement of a dyed sample fluid in the horizontal and vertical directions. (d) Confined stream of red blood cells in opto-fluidic device with input and output waveguides visible. (e) Signal output from cell counter where peaks indicate passage of individual cells. Scale bars are 100 μm. Adapted from [152].....91

Figure 5-2 Scanning electron microscopy images of As_2S_3 woodpiles. a) Woodpile with rod separation distance a = 2 μm. Inset - Each rod is made from eight parallel subrods to yield a rod height-width aspect ratio of almost unity. b) Top view of a woodpile with rod separation distance a = 1 μm. c) Focused ion beam cross section of the woodpile in (b). d) Close up of (b). Adapted from [167].....94

Figure 5-3 Schematic and images of inscribed channels in GLS for etchant study. a) sample schematic showing series of sample translation speeds across a channel block which then repeats with decreasing powers. Blue hatched area signifies a double spacing so that the individual blocks could be easily identified. b) brightfield microscopy images of the 40 mW channel block from above and at the sample end facet. Channel pitch is

100 μm and a 100 μm scale bar is provided in the zoomed in image of the 4 mm/s channel. 96

Figure 5-4 Fused silica versus GLS etch trial comparison. a) Fused silica microchannels after 6 hours etching in 5 vol% HF aqueous solution. Left-to-right: 200 mW average power channel then steps of 20 to 340 mW average power channel. b) GLS microchannels written with 40 mW average power after 4 hours etching in 1 vol% HCL aqueous solution. Left-to-right: 16, 8, 4, 2, 1 mm/s translation speed. 99

Figure 5-5 Programmed stage movements showing the opto-fluidic sensor design. Top down view and zoomed in section of central section of device. Zoomed in section clearly displays elliptical inlets and waveguide crossing central channel. 100

Figure 5-6 Images of the outcome of device fabrication testing in GLS and fused silica highlighting the remaining challenges for FLICE fabrication of GLS optofluidics. a) composite microscope image of fully etched optofluidic device in fused silica showing microfluidic channel and light delivery/collection waveguides. b) and c) images of connectorised fused silica chip. d) and e) microscope images, under transmission and reflection illumination respectively, illustrating the results of GLS device fabrication trials. Breaching of the device top surface can be clearly seen on the inlet/outlet ports and the waveguide sections.....103

Figure 6-1 Energy level configurations for a two-level system and the systems suitable for providing optical gain, where: a) two-level system, b) three-level system, c) quasi-three-level, and d) four-level system. Solid arrows signify radiative electron transitions where upwards pointing arrows are photon absorption events and downward facing arrows are photon emission events. Blue arrows are transitions mediated by pump photons whereas red arrows refer to signal photons. Green dashed arrows are non-radiative electron transitions and curly braces represent coupled levels with energy separation $\leq kT$, where k is Boltzmann's constant and T is the temperature of the system. 107

Figure 6-2 Mode-locked bulk Tm:Lu_2O_3 ceramic laser. a) Cavity schematic, where: FL, focusing lens (f = 63 mm); M1 and M2, plano–concave high-reflective mirrors (r1 = −75 mm, r2 = −100 mm); OC, output coupler (T = 1% at. 2000 nm); and FS, pair of fused silica prisms. b) Tunability of the mode-locked Tm:Lu_2O_3 ceramic laser. Adapted from [82, 180] 113

Figure 6-3 Brightfield microscope images showing the resulting material modification caused by waveguide writing. Top: waveguides in the low power range from 0.4 to 0.8 μJ. Bottom: waveguides in the high power range from 1.5 to 5 μJ. The inscription laser was incident from above in both cases. Microscope images contain overlaid to-scale graticule images which have a 10 μm pitch. 116

Figure 6-4 (a) Experimental setup for initial waveguide characterisation. PC, three paddle fiber polarisation controller; L1 and L2, AR-coated aspheric lenses; M1 and M2, silver mirrors; WUT, waveguide under test; L3, ×20 objective; VA, reflective variable ND filter; BD, beam dump. Blue dotted box signifies components mounted on waveguide alignment workstation. (b) and (c) Mode images for Type I and II guiding in Tm:Lu_2O_3 waveguides with 20 μm track separations, respectively. Red dashed ellipses indicate the area of the inscribed tracks. A 10 μm scale bar is included.....117

Figure 6-5 Waveguide laser experimental setup. HWP, half-wave plate; PBS, polarising beam splitter; BD, beam dump; M1 and M2, gold mirrors; OI, optical isolator; PS, periscope; L1 and L2, AR-coated aspheric lenses; PM, pump mirror; WUT, waveguide under test; OC, output coupler; VA, reflective variable ND filter; PF, optical filter. Blue dotted box signifies components mounted on waveguide alignment workstation. Green dotted box signifies power meter or detector positions. 119

Figure 6-6 (a) Input-output power characteristics of the Tm:Lu_2O_3 waveguide laser with different output couplers at the maximum output power experimental conditions. The inset shows the laser spectrum. (b) Experimental data and a linear fit of the inverse measured slope efficiencies against inverse output coupling. 121

Figure 6-7 (a) Microscope image of the waveguide used in the laser experiments. (b) and (c) show the pump (796 nm) and the laser (1942 nm) mode images, respectively. 10 μm scale bars are included. The green dotted circle shows the unmodified guiding region. Red dashed ellipses indicate the area of the inscribed tracks. (d) and (e) are the Gaussian fits to slices through the laser mode image in x and y directions, respectively. 123

Figure A-1 Image showing the main body of the ULI system. Clockwise from the bottom: laser back end, laser head and bench beamline section, raised optical bench for secondary laser sources, bank of K-cube controllers, power routing box for Aerotech components, stage drivers, Z stage and gantry beamline section, workpiece mount, X + Y stages and

vacuum pump. Not shown: air filter bank, room compressed air supply point and control PC. A-1

Figure A-2 Image showing the machining end of the ULI system, i.e. inscription head, translation stages, mounting plate and vacuum pump which are all user accessible. Zoomed in top down view of mounting plate shows hole options for vacuum mounting and 10 by 10 by 2 mm fused silica sample. Red circle indicates the vacuum pump switch location..... A-2

Figure A-3 Images of equipment on-states and location of switches/valves: (a) inscription laser back end; (b) room compressed air supply, use regulator valve to turn on/off supply leaving shut off valve open, when regulator is fully open should read 100 psi; (c) power routing box for Aerotech stage drivers and; (d) K-cube controllers and hub. Red arrows and circles indicate switch or valve locations. A-3

Figure A-4 Image of laser driver software main window. Clockwise from the top left: selection buttons to switching between main window and diode diagnostics window or to open pop up windows for laser output paratmer control; error message panel; output power plot; laser state indicator panels; and laser on and interlock reset buttons A-5

Figure A-5 Image of the initial laser settings commonly used. Top: the compressor settings window. This will usually be set to 10120 μm which gives the minimum pulse duration for 500 kHz pulse trains entering the amplifier. As well as changing the compressor position to temporally broaden the output pulses, changing the pulse picker AOM frequency changes the amplifier dispersion and therefore requires different compressor settings for the same pulse durations. Bottom: the synchronisation settings window. In general use, only the pulse picker frequency, modulator frequency and modulator efficiency are changed. These settings determine the repetition rate for the pulse train entering the amplifier stage of the Satsuma, the repetition rate of the output beam and the output power, respectively. A-6

Figure A-6 Image of FCAP ULI control software. A tab control allows for changing between the K-cube controller window, settings and help window, and the slope finder window used to establish the offset in the workpiece sample surface to the X-Y machining plane. Clockwise starting from the upper left in the K-cube controller window: .NET control for power waveplate; .NET control for linear polarisation state rotation waveplate; .NET control for shutter; options for power, polarisation and shutter possition, stop button

and power calibration button with indicator; .NET control for elliptical polarisation state waveplate. A-7

Figure A-7 Image of the Thorcam camera software with boxed area highlighting where the back-reflection signal occurs. Top zoomed in view shows the back-reflection signal when the objective focus is in the vicinity of the sample surface with the sample surface lower than the focus and bottom zoomed in view shows the alignment condition i.e. when the focus is exactly at the surface. A-9

Figure A-8 Image of the CNC operator interface. Clockwise from the top: stage status information; GUI motion and axis controls; emergency stop, error handling and further options; aerobasic program options and diagnostics; aerobasic program viewer; and command line for immediate motion commands. A-10

Acronyms and Abbreviations

2D - Two Dimensional.

3D - Three Dimensional.

$AgGaS_2$ - Silver Thiogallate.

AOS - All Optical Switching.

ATRAN - Atmospheric Transmission software tool.

BaF_2 - Barium Fluoride.

CaF_2 - Calcuim Flouride.

CO - Carbon Monoxide.

CO_2 - Carbon Dioxide.

CW - Continuous Wave.

DAC - Data Aquisition Card.

DFG - Difference Frequency Generation.

DMSO - Dimethylsulfoxide.

FCAP - Fraunhofer Centre for Applied Photonics.

FLAE - Femtosecond Laser-Assisted Etching.

FLICE - Femtosecond Laser Irradiation followed by Chemical Etching.

FSaS Group - Fiber Sensors and Supercontinuum Group.

FWM - Four Wave Mixing.

GASIR-1 - Germanium Arsenic Selenide Infrared.

GCIS - GeS_2-Ga_2S_3-CsI-Sb_2S_3-SnS.

GLS - Gallium Lanthanum Sulphide.

GLSSe - Gallium Lanthanum Sulphide Selenide.

GNLSE - Generalised Nonlinear Schrödinger Equation.

GPNG - $56GeO_2 – 31PbF_2 – 9Na_2O – 4Ga_2O_3$.

HAZ - Heat Affected Zone.

HCL - Hydrochloric Acid.

He-Ne - Helium-Neon.

HF - Hydroflouric acid.

HITRAN - High-resolution Transmission molecular absorption database.

HMFG - Heavy Metal Flouride Glass.

KLM - Kerr Lens Modelocking.

KOH - Potassium Hydroxide.

LoC - Lab-on-a Chip.

Lu_2O_3 - Lutetia.

MCN - Mean Co-ordination Number.

MFD - Mode Field Diameter.

MgF_2 - Magnesium Fluoride.

MI - Modulation Instability.

mid-IR - mid-Infrared.

MPA - Multiphoton Absorption.

ND - Neutral Density.

near-IR - near-Infrared.

NIST - National Institute of Standards and Technology.

NLO Group - Nonlinear Optics Group.

OPA - Optical Parametric Amplification.

OPG - Optical Parametric Generation.

OPO - Optical Parametric Oscillation.

PRF - Pulse Reptiton Frequency.

PTFE - Polytetrafluoroethylene.

QCL - Qauntum Cascade Laser.

Sc_2O_3 - Scandia.

SFG - Sum Frequency Generation.

SHG - Second Harmonic Generation.

SLM - Spatial Light Modulator.

SM - Single Mode.

SNR - Signal to Noise Ratio.

SPM - Self Phase Modulation.

SRS - Stimulated Ramn Scattering.

SWaP - Size, Weight and Power.

THG - Third Harmonic Generation.

ULI - Ultrafast Laser Inscription.

WD - Working Distance.

XPM - Cross Phase Modulation.

Y_2O_3 - Yttria.

YAG - Yttrium Aluminium Garnet.

ZBLAN - Zirconium-Barium-Lanthanum-Aluminum-sodium fluoride.

ZDW - Zero Dispersion Wavelength.

ZnS - Zinc Sulphide.

ZnSe - Zinc Selenide.

List of Publications

Peer Reviewed Journals and Conferences

M. D. Mackenzie, J. M. Morris, C. R. Petersen, H. T. Bookey, O. Bang, and A. K. Kar, "GLS and GLSSe Ultrafast Laser Inscribed Waveguides for Mid-IR Supercontinuum Generation," Optical Materials Express (Under preparation).

J. M. Morris, M. D. Mackenzie, C. R. Petersen, A. K. Kar, O. Bang, and H. T. Bookey, "Mid-IR Supercontinuum Generation in Ultrafast Laser Inscribed Waveguides," in Conference on Lasers and Electro-Optics, OSA Technical Digest (2018) (Optical Society of America, 2018), SM3D.2.

J. M. Morris, M. D. Mackenzie, C. R. Petersen, G. Demetriou, A. K. Kar, O. Bang, and H. T. Bookey, "$Ge_{22}As_{20}Se_{58}$ glass ultrafast laser inscribed waveguides for mid-IR integrated optics," Optical Materials Express 8, 1001 (2018).

J. Morris, N. K. Stevenson, H. T. Bookey, A. K. Kar, C. T. A. Brown, J. M. Hopkins, M. D. Dawson, and A. A. Lagatsky, "1.9 μm waveguide laser fabricated by ultrafast laser inscription in Tm:Lu_2O_3 ceramic," Optics Express 25, 14910 (2017).

N. K. Stevenson, J. Morris, H. Bookey, A. K. Kar, C. T. A. Brown, J. M. Hopkins, M. D. Dawson, and A. A. Lagatsky, "Waveguide Tm:Lu_2O_3 ceramic laser fabricated by ultrafast laser inscription," in 2017 Conference on Lasers and Electro-Optics Europe & European Quantum Electronics Conference (CLEO/Europe-EQEC), 2017).

J. Morris, G. Demetriou, A. Lancaster, A. Kar, and H. Bookey, "3D Optical Waveguides in $Ge_{22}As_{20}Se_{58}$ Glass - a Highly Nonlinear Material for the Mid-IR," in Conference on Lasers and Electro-Optics, OSA Technical Digest (2016) (Optical Society of America, 2016), JTh2A.82.

J. M. Morris, A. Kar, and H. Bookey, "Gallium Lanthanum Sulphide Glass for Ultrafast Laser Inscribed Optofluidic Devices," in Photon 16, (IOP, 2016).

Other Conferences and Workshops

A. Ravagli, B. Moog, Jean, F. Guzman Cruz, Alberto, C. Craig, A. Kar, M. Mackenzie, J. Morris, and D. Hewak, "Chalcogenide materials: Novel compositions and new applications," in Advanced Architectures in Photonics 2018, (Cambridge, 2018).

J. M. Morris, A. K. Kar, and H. T. Bookey, "Supercontinuum In Laser Fabricated Ge-As-Se Glass Waveguides; And What Is The Fraunhofer Centre For Applied Photonics?," in 2nd International Symposium on Doped Amorphous Chalcogenides and Devices, (Grasmere, 2018).

J. M. Morris, A. K. Kar, and H. T. Bookey, "Tm:Lu_2O_3 Ceramic Waveguide Laser Fabricated by Ultrafast Laser Inscription," in Workshop on Laser Device Physics & Engineering, (Edinburgh, 2017).

J. M. Morris, "Microfabrication of Photonic Devices for Mid Infrared Optical Applications," in CDT AP Conference, (St. Andrews, 2016).

J. M. Morris, "Microfabrication of Photonic Devices in Chalcogenide Glass Substrates," in CDT AP Conference, (Edinburgh, 2015).

J. M. Morris, "Microfabrication of Photonic Devices in Chalcogenide Glass Substrates," in Chalcogenide Advanced Manufacturing Partnership Open Day, (Southampton, 2014).

J. M. Morris, "Microfabrication of Photonic Devices for Mid Infrared Optical Applications," in IDC OPT Conference, (Edinburgh, 2014).

Chapter 1 Introduction

This introductory chapter aims to familiarise the reader with photonics, the utility of mid-Infrared (mid-IR) light and the microfabrication of photonic devices for optical applications in the mid-IR. The background section starts with a definition of photonics and highlights the breadth of areas where photonics is applied. Then the importance of mid-IR photonics is discussed and why developing new mid-IR photonic devices is necessary. Following this, the concept of integrated optics is introduced as are the advantages of Ultrafast Laser Inscription (ULI) for photonic device microfabrication. A penultimate section outlines the motivation for the work from the technology push from academia and the market pull from industry. Finally, in the last section, a thesis summary and chapter outline is provided.

1.1 Background

Photonics can be defined succinctly as the science and technology of light generation, manipulation and detection. Photonics has its foundations in the classical discipline of optics, which as a field of study has developed our understanding of the behaviour and properties of light over the course of almost 2000 years [1]. Consequently, the field of photonics can be considered to be a modern rejuvenation/reincarnation of optics with an applied science focus and an acknowledgement of the quantum nature of light [2].

Recently, photonics is receiving increasing recognition from the wider public because of the impact that research outputs from the field are having on our lives. In testament to this, the United Nations General Assembly proclaimed 2015 to be the International Year of Light and Light-based Technologies to celebrate the achievements of light science and its applications. The aim was to highlight the importance of photonics to humankind with over 13,000 events taking place in 147 countries to an estimated audience of over 100 million [3]. The success of this observance has led to the creation of an annual International Day of Light with an ongoing mission to support photonics awareness, education and research.

The origins and growth in importance of photonics can be chiefly attributed to the inventions of the laser [4], semiconductor optical devices [5, 6] and the developments of low loss silica optical fibre and erbium doped fibre amplifiers [7, 8]. Together, these

inventions drove the telecommunications boom of the 20th century and ultimately provided the world with the building blocks of the internet. As well as this significant contribution to the modern connected world in which we live, photonics has also found applications is areas as diverse as:

- Manufacturing – photolithography for computer chip production, and laser printing, welding, drilling, cutting and surface treatments for industries ranging from aerospace to textiles.
- Defence – directed energy weapons for area defence, night vision systems and head up displays for pilots, target acquisition, identification and tagging for smart munitions.
- Metrology – optical clocks for precision timing, and time-of-flight techniques for topological mapping and distance measurements.
- Health Care and Biology – light based therapeutics, new microscopy modalities including super resolution microscopy, and cell sorting or counting.
- Displays and Lighting – light emitting diodes and quantum dots for energy efficient lighting and flat panel displays.
- Sensing – detection of chemicals and bio-molecules; fibre sensing of temperature and strain in structures; and hyperspectral imaging.

Considering these examples alone it is plain to see that there is a vast array of opportunities for research and that there will certainly be applications where photonics could but doesn't provide an optimal or perhaps any solution. One such area is applications seeking to operate in the mid-IR parts of the electromagnetic spectrum, defined as electromagnetic radiation with wavelengths from ~2 – 20 μm in this thesis. This spectral region is of interest for a multitude of applications, some of which will now be briefly discussed.

Mid-IR photonic systems are used for the optical identification of gas, liquid chemicals and biomedical sensing, due to the characteristic absorption features that substances

exhibit across this wavelength range. An example of these absorption features is shown in Figure 1-1 for two isomers of propanol and the earth's atmosphere.

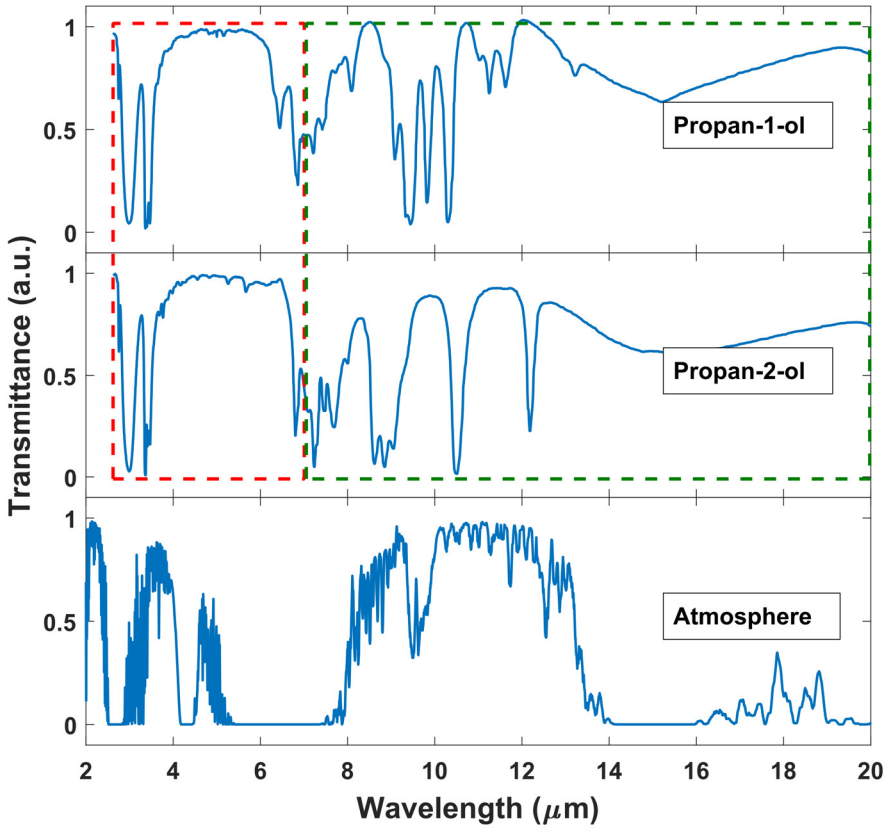

Figure 1-1 *Mid-IR transmission spectra of propan-1-ol and propan-2-ol, and a simulated transmission spectra of the atmosphere. The red box marks the functional group region and the green box marks the molecular fingerprint region. Propan-1-ol and propan-2-ol spectral data provided by the National Institute of Standards and Technology (NIST) and begins at 2.5 μm [9]. Atmospheric transmission spectra was simulated using the Atmospheric Transmission software tool (ATRAN) with the High-resolution Transmission molecular absorption database (HITRAN) [10]. Simulation output was smoothed using a moving average filter for clarity.*

For optical sensing applications, the mid-IR is split into two regions, namely the functional group region and the molecular fingerprint region, ~ 2.5 – 7 μm and ~ 7 – 20 μm, respectively. The functional group region contains features characteristic of the stretching vibrations of functional groups in a molecule which can be studied to identify the class of compound present. The fingerprint region on the other hand, encompasses features arising from complex bending vibrations in the molecule which are unique to a compound and therefore serves as a robust measurement of what molecules are present in a sample. Combined, these two regions allow for the initial classification of a

compound type and then the identification of the compound. This can be seen in the mid-IR spectra of propan-1-ol and propan-2-ol in Figure 1-1. These two compounds are isomers, and so contain identical bonds, the functional group regions of the spectra are almost indistinguishable with both showing absorption peaks distinct to the -OH functional group classifying the compounds as alcohols. Following on from this classification, the different pattern of absorption peaks in the fingerprint region for each compound allows for the identification of the specific alcohol present.

The mid-IR region also contains two transmission windows, ~ 2 – 5 μm and ~ 8 – 14 μm, which are wavelength bands of low absorption for atmospheric gasses, as can been seen in Figure 1-1. These mid-IR transmission windows are of interest in defence, free space communication and for standoff sensing because of the common requirement to be able to transmit power over long distances at wavelengths deemed to be eye-safe, i.e. > 1.4 μm retina damage is inhibited by absorption in the cornea [11]. Conversely, as many of the absorption features in the mid-IR can be attributed to water vapour, we can see how the region is useful for medical procedures requiring controlled deposition of energy such as laser scalpels used in surgery for simultaneous cutting and suturing [12].

Although applications exist that utilise mid-IR light, in general devices to generate, manipulate and detect light in the mid-IR are less developed than in the visible and near-Infrared (near-IR), ~ 0.39 – 0.7 μm and ~ 0.7 – 2 μm, respectively. This is due in part to the challenges of operating in the mid-IR spectral range, for instance thermal effects and the occurrence of atmospheric absorption, but also because of the mass-market applications driving technological advancement in other spectral ranges. For example, the low loss regions of silica fibre used for long haul data transmission appear in the near-IR which has driven decades of intensive research and heavy investment in photonics operating in this spectral regime. Even now there is a continual need for improved sources, detectors, transmission media, amplifiers and modulators in the near-IR to meet the world's ever increasing demands for data. Furthermore, in the visible spectral region, opportunities in high volume consumer markets for photonics, such as displays and imaging, has led to extensive research and development in this region as well.

The mass-market applications in the near-IR and visible have in turn led to mass production of photonic components capable of operating in these spectral ranges. This

drives down costs which itself opens up new possibilities for low-cost or even disposable products. Although currently the same cannot be said for the mid-IR, the successes of photonics in the visible and near-IR, show that if fabrication routes for mid-IR photonic systems are demonstrated which are compatible with mass production that this can drive research and development and open up new mass-market applications.

Photonic devices in any spectral region require a means of light generation but historically there have been relatively few lasers available for the mid-IR. Early sources were based on a sparse number of gas lasers such as Carbon Monoxide (CO), Carbon Dioxide (CO_2), and the mid-IR transitions of the otherwise ubiquitous Helium-Neon (He-Ne) laser, or cryogenically cooled lead salt lasers [13]. For solid state lasers, transition-metal doped Zinc Selenide (ZnSe) and Zinc Sulphide (ZnS) have been shown to offer broadband laser emission across most of the first atmospheric transmission window although lasing beyond ~ 3.7 μm still requires pulsed pumping or cryogenic cooling [14].

Many of the gaps in direct laser emission in the mid-IR can be filled by nonlinear frequency generation schemes with near-IR pump lasers, such as: Difference Frequency Generation (DFG) or Optical Parametric Amplification, Generation and Oscillation (OPA, OPG, OPO) which create discrete additional frequencies based on energy and momentum conservation conditions. Supercontinuum generation (SPG) is another nonlinear frequency generation method but in this instance, it is the action of a set of nonlinear processes in unison which creates a broad spectrum of output frequencies [15]. The common downside of these schemes is complexity. Nonlinear frequency generation requires high intensity light which is often supplied either by multi stage pump systems necessary to generate ultrashort high energy laser pulses or by resonating the one or more of the frequencies involved in the nonlinear process. This often results in elaborate system and cavity designs which can lead to stability issues, both long term and short term, increased cost and size.

Since the early 1990's III-V semiconductor diode lasers, which are well established in the near-IR, have made inroads into the mid-IR by means of the Quantum Cascade Laser (QCL) [16]. QCLs differ from traditional semiconductor lasers in that laser emission is not caused by interband transitions, i.e. an electron transferring between different electron bands, but by intersubband transitions, i.e. electrons moving through a structured

semiconductor constituting of many layers known as quantum wells. As the gain region in QCLs are engineered they offer a wide range of output wavelengths across the mid-IR as changing the quantum well layer materials and/or layer thicknesses allows for the tailoring of their emission spectrum. QCL's offer a much simpler route to generating mid-IR laser light than the nonlinear schemes mentioned but they do however have some shortfalls such as a narrow tuning range and are generally limited to low power outputs unless cryogenically cooled. The limitations on emission bandwidth and room temperature output powers can be somewhat overcome by using external cavity tuning elements and operating QCL's with duty cycles in the region of 10-20% [17]. But this is at the expense of device complexity, size and restricts device operation to pulsed output modes. From the available mid-IR sources, we can see that there are prospects for research and development to fill the gaps in direct laser emission and in establishing methods to reduce the size and complexity of mid-IR sources based on frequency conversion.

Photonic systems rely on the transmission and manipulation of light with low loss; in the mid-IR, this can be achieved with free space optics when operating in the atmospheric transmission windows but for other wavelengths or for compact devices, waveguides in mid-IR transmitting materials are required. Waveguides come in various guises but in principle all perform the same task, i.e. they confine light in at least one direction and allow it to propagate along the remaining unconfined directions. Two such broad classes of waveguides are fibres and channel waveguides and mid-IR transmitting materials have been used to fabricate both.

In the case of mid-IR fibres, chalcogenide glasses, glasses containing sulphur (S), selenium (Se) and/or tellurium (Te) as their main constituents, have been widely produced and used, as have heavy metal fluoride glass (HMFG) fibres such as those made from Zirconium-Barium-Lanthanum-Aluminium-sodium fluoride (ZBLAN) [18]. ZBLAN fibres generally outperform chalcogenides in terms of lowest loss due to the punishing extrinsic losses which can occur when impurities are introduced during the manufacture of chalcogenide fibres; this also causes a more structured transmission spectrum compared to the flatter spectra from ZBLAN fibres. On the other hand, ZBLAN and other HMFGs are hygroscopic, and therefore less stable than chalcogenides, with a shorter mid-IR absorption edge. Apart from glasses, polycrystalline silver halide fibres

and single crystal sapphire or Yttrium Aluminium Garnet (YAG) fibres are also used for mid-IR applications [18]. Finally, there has also been the recent development of semiconductor core – silica cladding optical fibres, whereby materials such as ZnSe are deposited via chemical deposition in hollow core silica fibres, offering the chance for mid-IR guiding and in-fibre optoelectronics [19, 20].

All the mid-IR fibres mentioned are delicate and/or harder to fabricate in comparison with near-IR silica fibres and little work has been done in respect to reproducing the myriad of modular fibre components that are available for near-IR inline manipulation, such as splitters, circulators and modulators [21]. Mid-IR fibres are therefore predominately used as discrete photonic components, for example as a transport fibre for light delivery, and not for creating entire photonic systems such as a fibre laser sources, inline signal processors etc.

Mid-IR channel waveguides can be classified by the techniques used to fabricate them, which is commonly either thin film or direct write methods. For the fabrication of mid-IR thin film channel waveguides semiconductors on silicon such as aluminium nitride and silica nitride, or chalcogenide glasses and diamond are suitable [22]. The creation of thin film channel waveguides can be attained by various routes, as summarised in Figure 1-2, but it is always multi-step due to the need to deposit various material layers and to pattern either the deposited layers themselves or the masking layers used. Using chalcogenide glasses can alleviate some fabrication difficulty as their solubility and low melting temperatures allow for simpler processing steps such as deposition by solution processing and patterning by hot embossing [23, 24]. The technology behind patterning, selective layer deposition and selective removal by etching although complex also allows for the simultaneous fabrication of many other photonic components on chip. Also, it is worth noting that the silicon on insulator platform being developed for the near-IR can be adapted to operate in the short wavelength side of the mid-IR up to around 5 μm by limiting the overlap of waveguide modes with the oxide insulator layer. Two such examples are using pedestal or slot waveguides [25].

Thin film techniques offer one well-established route towards mid-IR channel waveguides and component production with advantages such as an inherent capability for parallelisation for mass production. They do however have some distinct disadvantages

as well, chiefly: their process complexity and inability to perform rapid prototyping. Direct write techniques can overcome these shortfalls and have some other significant advantages of their own. These fabrication methods all rely on locally modifying the material either through doping, as in ion implantation, or by inducing material changes, as in ULI.

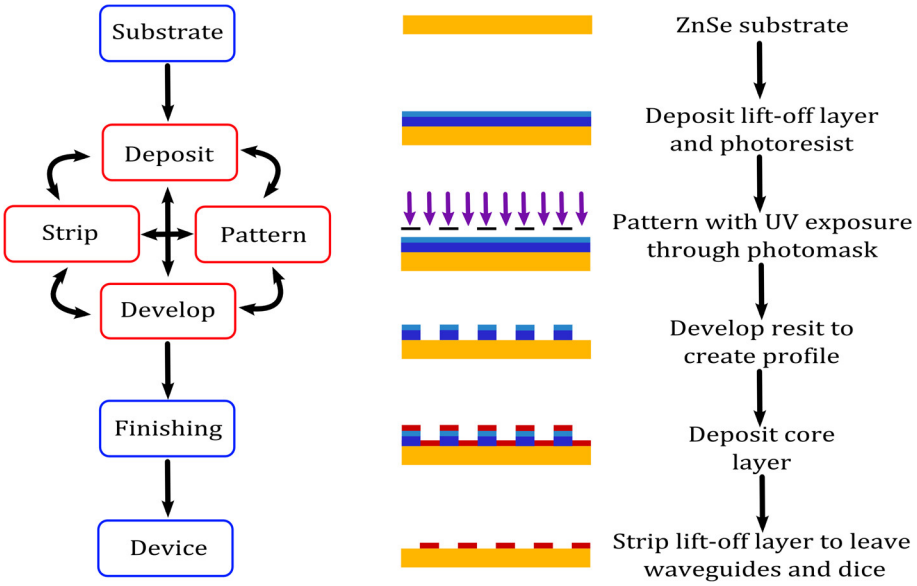

Figure 1-2 *RHS: A generalised flow diagram of the process steps for mid-IR thin film channel waveguide fabrication. Starting with a substrate, each device layer can be fabricated by an appropriate sequence of device layer and masking layer deposition, patterning, developing and striping. Numerous sequences are needed if multiple final device layers are required, for instance in the case of a buried channel waveguide with top and bottom cladding layers. LHS: shows a schematic for the creation of air clad* $GeTe_4$ *thin-film channel waveguides following the procedure described in ref [26].*

ULI in particular, has been shown to have the broadest materials library of any waveguide writing technique, with waveguides and other photonic components produced in materials where fibre drawing and/or thin film deposition and patterning is impossible or undeveloped. ULI also allows for the micro-structuring of materials by the modification of an irradiated region's resistance to removal by chemical etchants which has utility in areas such as microfluidic manipulation and sensing [27]. ULI can be used independently to fabricate entire photonic systems and can also produce interfacial modules to link fibre and chip components to create hybrid integrated systems [28, 29]. Uniquely, ULI gives a true three dimensional (3D) design freedom which can be used for on chip vertical

stacking of components, arbitrary free space outputs [30], free form micro-structuring [31] and adding functions to existing photonic components such as waveguides in fibre claddings for stress-independent torsion sensors [32].

The strengths of ULI allows for fabricating channel waveguide based solutions to address some of the mentioned shortfalls and gaps in currently demonstrated mid-IR photonics devices. For instance, the size and complexity of mid-IR sources based on nonlinear frequency conversion, such as supercontinuum sources, can be lessened by using channel waveguides to reduce their threshold power and increase their nonlinear interaction length. This would allow for cheaper lower power single stage pump sources to be used and potentially remove the need for complex cavities. For mid-IR direct laser emission, channel waveguides in novel materials that are not able to be deposited for thin film waveguides or drawn into fibres for fibre lasers could lead to new compact sources. Another option for improving mid-IR lasers could be using channel waveguides to combine arrays of QCL's to broaden the output of integrated QCL sources and/or create higher output powers. The ability of ULI to add channel waveguides to other photonic components could also lead to new functionality from mid-IR fibres in the absence of available mid-IR fibre components.

Moreover, ULI's ability to produce channel waveguides and photonic components with a common substrate makes it suitable for the microfabrication of mid-IR integrated optical systems. Integrated optics seeks to couple two or more optical components on a single chip to fulfil some more or less complex function. These integrated optical systems aim to give the same functionality as systems constructed from discrete optical components but with reduced size, cost and component number. Channel waveguides provide the means for linking these components on a single chip allowing for the combination of multiple photonic components and the creation of integrated optical systems. One such example is on-chip resonators, which when coupled to waveguides can be used to create photonic systems for processes such as filtering broadband signals into harmonics of the resonating frequency or enhancing chemical detection by creating a longer effective path length for light propagating through the system [33, 34].

The microfabrication of mid-IR photonic devices using techniques compatible with the integrated optics approach, such as ULI, provides a clear route by which mid-IR photonic

system fabrication can be scaled up towards mass production. The previously mentioned benefits of mass production to photonics in the near-IR and visible in terms of reduced system cost and increased breath of available devices would then also be enjoyed by those applications seeking to work in the mid-IR, driving the development of mid-IR photonics.

1.2 Motivation

The goal for my research has been to use ULI to fabricate photonic devices in mid-IR transmitting and/or highly nonlinear novel materials. These devices are based on waveguide writing and selective material removal using different etching techniques. The investigations carried out aim to further establish these techniques as an enabling technology for microfabrication of photonic devices in the mid-IR that is compatible with the integrated optics approach.

From the background section, we can see that there is scope for scientific enquiry in the area of mid-IR photonics due to it being less developed than visible or near-IR photonics and because of the utility of the mid-IR spectral region for many applications. ULI was chosen as the fabrication method due to its unparalleled freedom in host materials and for its aforementioned advantages over other manufacturing techniques compatible with the ethos of integrated optics.

As well as the technology push for mid-IR photonics from academia this work has also been driven by market pull from the photonics industry. This is reflected in the nature of the Engineering Doctorate degree which this thesis is submitted towards. The Engineering Doctorate is an alternative to the traditional PhD which combines the usual PhD level research project with additional Master's level technical and business courses with students spending the majority of their time working directly with a company. To ensure that the work will be industrially relevant the research projects are proposed by the industrial partner with much of the research undertaken at research and development facilities based at the partner company.

This work has been supported by the Fraunhofer Centre for Applied Photonics (FCAP) in Glasgow. As one of the research centres of the wider Fraunhofer Society, FCAP has a remit to provide professional research and development services to industry with demand driven, applied research combined with scientific excellence, strong integration with

academia and autonomy to pursue areas of research that benefit the industry each centre/institute supports [35]. FCAP provides assistance to the UK photonics industry as a not-for-profit entity whose long-term survival is dependent on being at the forefront in areas of photonics research that best serve the needs of industry. It is worth highlighting that this work closely aligns with their core technical offering of advanced mid-IR laser sources which they have identified as an area of interest for UK photonics.

Apart from the market pull from interest in mid-IR photonics there has also been a recent surge in investment in advanced laser fabrication techniques. Taking ULI alone as an example in the last 10 years companies, such as: Optoscribe, LightFab, Femtoprint, Optofab and Workshop of Photonics, based in the UK, Germany, Switzerland, Australia and Lithuania respectively, have successfully commercialised ULI techniques for their businesses. For this reason, the outputs from this work are also of interest to FCAP in giving them the capability and experience to perform this type of advanced laser processing. Having an in-house toolbox of previously fabricated photonic components and known fabrication parameters for mid-IR transmitting materials is another motivation for this work.

1.3 Thesis Summary and Outline

This thesis details research into the microfabrication of photonic devices for mid-IR optical applications. In this work, the fabrication and demonstration of ULI mid-IR waveguide laser sources were investigated due to their utility in remote sensing. ULI enabled selective chemical etching of mid-IR transmitting glass was also studied due to its potential in integrated optical sensing for gas, liquid chemical or biomedical samples. ULI waveguides in highly nonlinear materials were manufactured, studied and employed for chip scale nonlinear frequency conversion. In tandem with this fabrication and applications research a custom advanced laser processing setup suitable for ULI fabrication was designed, built and commissioned. This thesis is structured as follows:

Chapter 1 has given a background to this research topic by establishing the importance of photonics to the modern world and the opportunities for new solutions in mid-IR photonics. The benefits of the manufacturing method used are highlighted, as is the concept of integrated optics and why developing mid-IR integrated optics components

for mid-IR sources and mid-IR sensors is important. The motivation for the work from the technology push from academia and the market pull from industry has been discussed.

Chapter 2 details the theory of waveguides from the physics of light confinement to the mathematical description of waveguide modes. Following this, nonlinear light-matter interactions are discussed and it is shown how a material's nonlinear optical response leads to the generation of new optical frequencies. Next, the energy absorption processes which underpin ULI and how they lead to refractive index change, necessary for guiding light, and structural changes, necessary for increasing chemical etching rates, are discussed. Finally, the relevant properties of the main mid-IR transmitting materials used in this work are detailed.

Chapter 3 describes the design, build and commissioning of an advanced laser processing setup at FCAP suitable for ULI. An overview of the practical considerations concerned with ULI fabrication is given. The hardware procured and control software design is discussed with each decision supported by a reasoned argument as to why that choice was made. Initial outputs from the system are then presented.

Chapter 4 discusses the first demonstration of inscription and testing of waveguides in GASIR-1 (Germanium Arsenic Selenide Infrared) glass. Firstly, an overview of mid-IR chalcogenide ULI waveguides along with their application is given. This is followed by details on how a suitable ULI parameter range was found to produce ULI waveguides in GASIR-1 and how the waveguides were subsequently tested for losses, dimensions of the guided modes and their dispersive properties. Finally, the GASIR-1 ULI waveguides utility for chip scale low peak power broadband sources is shown by demonstrating the broadest and deepest mid-IR supercontinuum to-date from a ULI waveguide.

Chapter 5 presents the first demonstration of selective chemical etching of ULI modified regions in Gallium Lanthanum Sulphide (GLS) glass. The chapter begins with detailing previous work which has been undertaken in etching of ULI modified regions in chalcogenide glasses. Next, the various laser parameters and etching methods tested for GLS selective etching are described along with the best etching selectivity attained. A demonstrator optofluidic sensor is fabricated in GLS and fused silica glass to illustrate the potential of the tested techniques.

Chapter 6 details the first demonstration of a ULI waveguide laser in Thulium Lutetium Oxide ($Tm:Lu_2O_3$) ceramic. The previous work in mid-IR bulk laser systems using sesquioxide material hosts as their gain media is summarised. This is followed by details on how a suitable ULI parameter range was found to produce ULI waveguides in $Tm:Lu_2O_3$ and how the waveguides were subsequently tested for losses and dimensions of the guided modes. The testing for lasing action is then discussed and the characteristics of the resulting chip scale ULI waveguide laser presented.

Chapter 7 draws conclusions on the investigations carried out in this thesis and outlines the future work that the author envisions could follow on from this project. The future work is divided into subsections with specific focussed research paths involving ULI fabrication of mid-IR photonic components or systems. The Chapter concludes with a summary presenting some closing thoughts on the state of the current body of work and where future progress can be made.

Appendix A serves as a user guide for the ULI processing system at FCAP. The system setup, usage and shutdown procedures are given.

Chapter 2 Light-Matter Interactions and Optical Materials

As outlined in the previous Chapter, this work focusses on the use of ULI to fabricate integrated optics compatible photonic devices in mid-IR transmitting materials. The fundamental building block of integrated optics is the dielectric waveguide as this structure forms the link between the different components on an integrated optic chip. It is therefore important to understand the principles of waveguides, which is covered at the start of this Chapter, and how they can confine light and direct light. The physics of light-matter interactions is also discussed as this enables ULI itself and allows for the supercontinuum generation shown in Chapter 4. The next section provides a description of ULI as a fabrication technique including the dynamics of light absorption, the way in which this energy is transferred to the substrate, the types of material modification induced by this energy deposition and their suitability for both waveguide and microfluidic channel fabrication in both vitreous and crystalline samples. The penultimate section presents the pertinent material properties for photonics devices of the main material classes used in this work. This Chapter concludes by summarising the topics covered and how they were used to inform the experimental work conducted.

2.1 Waveguides

Light is classically described as a travelling wave formed from the synchronous oscillation of electric and magnetic fields [36]. Therefore, in order to understand the origin of light guiding in dielectric waveguides, we must begin with describing the propagation of electromagnetic waves in materials. This is accomplished by starting with Maxwell's equations in matter, which are [37]:

$$\nabla \times \boldsymbol{E}\left(r,t\right) = -\frac{\partial \boldsymbol{B}\left(r,t\right)}{\partial t} \qquad 2\text{-}1$$

$$\nabla \times \boldsymbol{H}\left(r,t\right) = \boldsymbol{J}_{f}\left(r,t\right) + \frac{\partial \boldsymbol{D}\left(r,t\right)}{\partial t} \qquad 2\text{-}2$$

$$\nabla \cdot \boldsymbol{D}\left(r,t\right) = \rho_{f}\left(r,t\right) \qquad 2\text{-}3$$

$$\nabla \cdot \boldsymbol{B}\left(r,t\right) = 0 \qquad 2\text{-}4$$

where $\nabla\times$ is the curl operator, $\boldsymbol{E}$ is the electric field vector, $\boldsymbol{B}$ is the magnetic field vector, $\boldsymbol{H}$ is the magnetising field vector, $\boldsymbol{J}_f$ is the free current density, $\boldsymbol{D}$ is the displacement field vector, $\nabla\cdot$ is the divergence operator and ρ_f is the free charge density. The relationship between the $\boldsymbol{E}$ and $\boldsymbol{B}$ fields and the auxiliary $\boldsymbol{D}$ and $\boldsymbol{H}$ fields is given by:

$$\boldsymbol{D}(r,t)=\varepsilon_0\boldsymbol{E}(r,t)+\boldsymbol{P}(r,t) \qquad 2\text{-}5$$

$$\boldsymbol{H}(r,t)=\frac{1}{\mu_0}\boldsymbol{B}(r,t)-\boldsymbol{M}(r,t) \qquad 2\text{-}6$$

where ε_0 is permittivity of free space, $\boldsymbol{P}$ is the polarisation density vector, μ_0 is the permeability of free space and $\boldsymbol{M}$ is the magnetisation vector.

The response of a dielectric to an electric field, such as the travelling optical field from the passage of light, is to polarise by the displacement of bound charges in the medium away from their equilibrium position. This response is captured by the polarisation density which for a linear, isotropic and homogenous dielectric is given by:

$$\boldsymbol{P}(r,t)=\varepsilon_0\chi_e\boldsymbol{E}(r,t) \qquad 2\text{-}7$$

where χ_e is the electric susceptibility.

Substitution of equation 2-7 into equation 2-5 leads to a simplified form of the displacement field for a dielectric:

$$\boldsymbol{D}(r,t)=\varepsilon_0(1+\chi_e)\boldsymbol{E}(r,t)=\varepsilon_0\varepsilon_r\boldsymbol{E}(r,t)=\varepsilon\boldsymbol{E}(r,t) \qquad 2\text{-}8$$

where ε_r is the relative permittivity of the medium, also known as the dielectric constant, and ε is the total electric permittivity.

In the special case of light propagation in a dielectric medium we can immediately simplify equations 2-2, 2-3 and 2-6 above by noting that $\boldsymbol{J}_f$, ρ_f and $\boldsymbol{M}$ equal zero as

dielectrics are non-conducting and non-magnetic. Taking the curl of equation 2-1 and substituting in the simplified versions of equations 2-6, 2-2 and 2-8 leads to:

$$\begin{aligned}\nabla\times\left(\nabla\times\boldsymbol{E}\left(r,t\right)\right) &= -\frac{\partial\nabla\times\left(\boldsymbol{B}\left(r,t\right)\right)}{\partial t}\\ &= -\mu_0\frac{\partial\nabla\times\left(\boldsymbol{H}\left(r,t\right)\right)}{\partial t}\\ &= -\mu_0\frac{\partial\boldsymbol{D}\left(r,t\right)}{\partial t}\\ &= -\mu_0\varepsilon\frac{\partial\boldsymbol{E}\left(r,t\right)}{\partial t}\end{aligned} \qquad \textit{2-9}$$

The relationship between refractive index and relative permittivity in a non-magnetic medium is given by $n = \varepsilon_r^{1/2}$; and the speed of light in vacuum is related to the permittivity and permeability of free space by $c = (\varepsilon_0 \cdot \mu_0)^{-1/2}$. Using these relationships, we can rewrite equation 2-9 as:

$$\nabla\times\left(\nabla\times\boldsymbol{E}\left(r,t\right)\right) = -\frac{n^2}{c^2}\frac{\partial\boldsymbol{E}\left(r,t\right)}{\partial t} \qquad \textit{2-10}$$

Then using the vector identity:

$$\nabla\times\left(\nabla\times\boldsymbol{A}\right) = \nabla\left(\nabla\cdot\boldsymbol{A}\right) - \nabla^2\boldsymbol{A} \qquad \textit{2-11}$$

on the LHS of equation 2-10, substituting in the simplified version of equation 2-3 and rearranging, leads to:

$$\nabla^2\boldsymbol{E}\left(r,t\right) = \frac{n^2}{c^2}\frac{\partial\boldsymbol{E}\left(r,t\right)}{\partial t} \qquad \textit{2-12}$$

which is the wave equation for light propagation in a dielectric medium, considering only the electric field component of light.

There are an infinite number of solutions to equation 2-12 for unguided light propagation but the constraints imposed by a waveguide structure define a finite subset of guided mode solutions, where light is confined by the waveguide. As an example, a 1D

symmetric dielectric waveguide, or infinite slab waveguide, consists of a stack of three dielectric layers where the first and third layers are called the cladding layers and the second layer is called the core layer. In this structure, the refractive indices of the layers are chosen so that $n_1 = n_3 < n_2$, where n_1 and n_3 are the cladding layer refractive indices and n_2 is the core layer refractive index, respectively. For this waveguide, a general solution to equation 2-12 which assumes a monochromatic travelling wave in the z direction, takes the form [2]:

$$\boldsymbol{E}_j(r,t) = \boldsymbol{E}_j(x)\exp\left(i\left(\omega t - \beta_j z\right)\right) \qquad 2\text{-}13$$

where $\boldsymbol{E}_j(x)$ is the transverse field profile, ω is the angular frequency of the optical field and β_j is the propagation constant of the j^{th} order mode.

For guided modes, in the cladding layers $\boldsymbol{E}_j(x)$ is a decaying exponential, whereas in the core layer the field profile is oscillatory with either a cosine or sine profile for the symmetric and antisymmetric modes respectively [38]. The different field profiles in the cladding and core layers appear as solutions from the allowed values of β_j for guided modes which is found to be in the range of $(n_{1,3}k_0) < \beta_j < (n_2k_0)$, where k_0 is the free space wavevector. The final restriction that quantises the guided mode solutions and sets a finite limit on the number of modes a waveguide can support is the interfacial constraints. These stem from Maxwell's equations and require that the transverse components of $\boldsymbol{E}$ and $\boldsymbol{H}$ and their first order partial derivatives must be continuous across as the interfaces between the core and cladding layers [38].

From the general solution to an infinite slab waveguide presented and the subsequent discussion on the origins of a quantised and finite set of guided mode for a waveguide we can see that there is potential to tailor the properties of the modes a waveguide supports. The choice of layer materials and waveguide geometry will affect the symmetry, number and field profile of the modes of a waveguide. For this reason, solving equation 2-12 is often done numerically as analytical solutions are only obtained for the simplest waveguide geometries such as the infinite slab waveguide solution given and step index optical fibres.

2.2 Nonlinear Light-Matter Interactions

The previous section has shown how applying the Maxwell equations to solve light propagation in a structured dielectric leads to guided modes of light. In this section we will revisit Maxwell's equations to see how light propagation in dielectrics can also lead to the generation of new frequencies of light, the simultaneous absorption of multiple numbers of photons and the tunnelling of electrons out of bound states. These processes are all due to the nonlinear interactions of the optical field, from a travelling light wave or pulse, and a dielectric medium.

2.2.1 Non-Resonant Nonlinear Light-Matter Interactions

In deriving a wave equation for the propagation of light in a dielectric medium, see equation 2-12, it was assumed that the polarisation response of a dielectric to an electric field was proportional to the magnitude of the applied field, see equation 2-7. This linear relationship holds for low light intensities but breaks down as the applied electric field strength approaches the atomic electric field strengths that bind electrons to their constituent atoms [37]. When this condition is met, the polarisation response of a dielectric medium becomes a nonlinear function of the applied field. This behaviour is captured through a nonlinear electric susceptibility and equation 2-7 becomes [15]:

$$\boldsymbol{P}(r,t) = \varepsilon_0 \left(\chi_e^{(1)} \boldsymbol{E}(r,t) + \chi_e^{(2)} \boldsymbol{E}^2(r,t) + \chi_e^{(3)} \boldsymbol{E}^3(r,t) + \ldots \right) \qquad 2\text{-}14$$

where $\boldsymbol{P}$ is now expressed as a Taylor series expansion with $\chi_e^{(1)}$ the linear electric susceptibility, a dimensionless quantity, and $\chi_e^{(n=2,3,..)}$ the n^{th} order nonlinear electric susceptibility term, with units of $(m/V)^{n-1}$.

It is important to note that not all dielectric media have a $\chi_e^{(2)}$ response as it is dependent on the material being non-centrosymmetric. Anisotropic media, such as many crystalline materials, are therefore prevalent in the field of nonlinear optics and to encompass this anisotropy the electric susceptibly terms become $n+1$ rank tensors. As a final note on the nature of the electric susceptibility, in the case of the material attenuating the applied field the electric susceptibility becomes a complex quantity with imaginary components related to this attenuation [2].

For simplicity, to demonstrate how a nonlinear polarisation response leads to the generation of new frequencies, we consider only the temporal response of material exhibiting both a $\chi_e^{(2)}$ and $\chi_e^{(3)}$ response to a time varying electric field defined by:

$$\boldsymbol{E}(t) = \boldsymbol{E}_0 \cos(\omega t) \qquad 2\text{-}15$$

where $\boldsymbol{E_0}$ is the maximum field amplitude and ω is the angular frequency of the field.

Inserting equation 2-15 into the temporal version of equation 2-14 truncated at the third order nonlinear electric susceptibility term and using the trigonometric identities:

$$\cos^2(x) = \frac{1}{2}(1 + \cos(2x)) \qquad 2\text{-}16$$

$$\cos^3(x) = \frac{3}{4}\cos(x) + \frac{1}{4}\cos(3x) \qquad 2\text{-}17$$

gives:

$$\boldsymbol{P}(t) = \varepsilon_0 \begin{pmatrix} \chi_e^{(1)} \boldsymbol{E}_0 \cos(\omega t) + \\ \frac{1}{2}\chi_e^{(2)} \boldsymbol{E}_0^{\,2}\left(1 + \cos(2\omega t)\right) + \\ \frac{3}{4}\chi_e^{(3)} \boldsymbol{E}_0^{\,3} \cos(\omega t) + \frac{1}{4}\chi_e^{(3)} \boldsymbol{E}_0^{\,3} \cos(3\omega t) \end{pmatrix} \qquad 2\text{-}18$$

Remembering that the polarisation density represents the displacement of bound charges in the dielectric from their equilibrium position, i.e. the formation of electric dipoles throughout the medium. Therefore, an oscillating ***P*** results in oscillating electric dipoles with the same frequency components. This in turn generates light at these frequencies. It is important to highlight that as there is no phase delay between the driving applied field and ***P*** this represents an instantaneous response of the dielectric. This implies there is no net transfer of energy, momentum, or angular momentum between the optical field and the dielectric. In nonlinear optics, this type of interaction is called a parametric response.

From the terms in equation 2-18, we can see that the 2nd order nonlinear response has led to a static DC field, called optical rectification, and an additional field with twice the

frequency of the fundamental applied field, called second harmonic generation (SHG). The 3rd order response has generated a field that provides a nonlinear contribution to $\boldsymbol{P}$ at the fundamental frequency, an effect which can be captured by defining a nonlinear refractive index. The 3rd order response has also produced an additional field with three times the frequency of the fundamental applied field, called third harmonic generation (THG).

For the derivation of equation 2-18 a monochromatic fundamental field was assumed but there is no reason as to why there can't be multiple input frequencies. This allows for a large range of additional frequencies to be output through mixing of the input fields in processes such as sum and difference frequency generation (SFG and DFG, respectively) for a $\chi_e^{(2)}$ response, and four wave mixing (FWM) for a $\chi_e^{(3)}$ response.

Although there is potential for a multitude of new frequencies to be generated through the parametric nonlinear polarisation response of a dielectric, there is another condition that dictates whether a meaningful amount of energy transfer happens between the fundamental field and a new frequency component. This condition is called phase matching and is related to the wavevector of the fundamental field generating the new frequency and the wavevector of the propagating new frequency component. As an example, if we consider SHG, we know that the propagating fundamental wave and second harmonic wave will have the forms:

$$\boldsymbol{E}_{\omega}(z,t) = \boldsymbol{E}_{0}\cos(\omega t - k_{\omega} z) \qquad 2\text{-}19$$

$$\boldsymbol{E}_{2\omega}(z,t) = \boldsymbol{E}_{0}\cos(2\omega t - k_{2\omega} z) \qquad 2\text{-}20$$

where $\boldsymbol{E_{\omega}}$ is the travelling fundamental wave with wavevector k_{ω} and $\boldsymbol{E_{2\omega}}$ is the travelling second harmonic wave with wavevector $k_{2\omega}$.

Perfect phase matching requires that $2k_{\omega} = k_{2\omega}$, and under this condition the second harmonic waves radiated at each point along the propagation direction of the fundamental beam add constructively to produce a co-propagating second harmonic beam. Unfortunately, real world materials exhibit chromatic dispersion, which is the frequency dependence of their refractive index. This property causes a phase mismatch ($\boldsymbol{\Delta k}$) for different frequencies with magnitude given by:

$$\Delta k = k_{2\omega} - 2k_{\omega} = \frac{2\omega}{c}\left(n_{2\omega} - n_{\omega}\right) \qquad 2\text{-}21$$

where $n_{2\omega}$ is refractive index at the second harmonic frequency and n_{ω} is refractive index at the fundamental frequency.

When there is a phase mismatch between the fundamental and generated frequency components there is back-conversion of the generated frequency terms to the fundamental beam as the relative phase between the two beams drifts. This severely restricts the amount of the new frequency component that is output. Whilst this restriction is a limiting factor in the usefulness of nonlinear frequency generation to create a broad range of new output wavelengths simultaneously, there are also benefits to the phase matching condition. Provided a scheme can be devised to allow for phase matching between the fundamental and a generated frequency of interest we can see that the energy of the fundamental beam only has one pathway to take out of the many other possible options which can lead to efficient generation of the new frequency. In addition, there are phase matching schemes which allow for tuning of the phase matching condition, such as critical phase matching [39] and quasi phase matched crystals with fanout poling [40], that allow for sweeping across a wide range of output frequencies from a single process such as DFG.

2.2.2 Supercontinuum generation

SPG is another nonlinear frequency generation method but in this instance instead of one or two well defined frequencies being generated, a broad and ideally continuous spectrum of light is output. Starting with a high intensity fundamental beam or pulse, the spectral content of a supercontinuum source can span several octaves, making them a seemingly ideal broadband source. It is however, important to highlight that this spectral width comes at the expense of lowering the source's power spectral density as power is distributed across the output spectrum.

As we have emphasised in the previous section, nonlinear frequency generation requires phase matching, which would seem to preclude the possibility of supercontinuum generation. Fortunately, there are a number of non-parametric and parametric processes that are automatically phase matched which can lead to supercontinuum generation, such

as: Stimulated Raman Scattering (SRS), (MI) Modulation instability, Self Phase Modulation (SPM) and Cross Phase Modulation (XPM).

SRS is caused by the resonant driving of a molecular vibration, also known as phonon, to generate a frequency shift in the input fundamental beam. This imparts thermal energy to the material and is therefore a non-parametric process. SRS is automatically phase matched as the molecular resonance which modulates the fundamental frequency is driven by the beating of the fundamental frequency and the new frequency components generated by the modulation.

MI, SPM and XPM on the other hand are automatically phase matched and parametric due to their link with the nonlinear refractive index which originates from the 3rd order nonlinear susceptibility. This can be shown by taking the terms in equation 2-18 which oscillate at the fundamental frequency, and inserting them into the definition of the displacement field, see equation 2-5:

$$\begin{aligned}\boldsymbol{D}(r,t) &= \varepsilon_0 \boldsymbol{E}(r,t) + \varepsilon_0 \chi_e^{(1)} \boldsymbol{E}(r,t) + \frac{3}{4}\varepsilon_0 \chi_e^{(3)} \boldsymbol{E}^3(r,t) \\ &= \varepsilon_0 \boldsymbol{E}(r,t)\left(1 + \chi_e^{(1)} + \frac{3}{4}\chi_e^{(3)} |\boldsymbol{E}|^2\right)\end{aligned} \qquad 2\text{-}22$$

Using the definition of the refractive index in dielectric media, $n = (1+\chi_e)^{1/2}$, we can identify the bracketed terms in equation 2-22 as an expression for refractive index where the linear and nonlinear terms are explicitly stated, therefore:

$$n = n_0\left(1 + \frac{3}{4n_0}\chi_e^{(3)} |\boldsymbol{E}|^2\right)^{1/2} \qquad 2\text{-}23$$

where n_0 is the linear part of the refractive index given by $n = (1+\chi_e^{(1)})^{1/2}$.

As $\chi_e^{(3)} << 1$ the expression for the nonlinear refractive index can be written as:

$$n = n_0\left(1+\frac{3}{8n_0}\chi_e^{(3)}\left|\boldsymbol{E}\right|^2\right) = n_0 + n_2 I \qquad 2\text{-}24$$

where n_2 is the nonlinear refractive index, given by $n_2 = 3\chi_e^{(3)}/(4n_0^2\varepsilon_0 c)$, and I is the intensity of the optical field, given by $I = 1/2 n_0 \varepsilon_0 c|\boldsymbol{E}|^2$.

For SPM the nonlinear contribution to the refractive index, as defined by equation 2-24, causes an intense light pulse to modulate the material's refractive index with the same temporal shape as the envelope of the pulse. This time varying refractive index imparts a time varying change in the instantaneous phase of the pulse causing a red-shift in frequency of the leading edge of the pulse and a blue-shift in frequency of the trailing edge. For input light pulses that are unchirped or up-chirped, SPM results in spectral broadening of the pulse. XPM is similar to SPM but involves the impact of an intense light pulse on any co-propagating signal by the same effect of refractive index modulation. This can lead to spectral broadening in the co-propagating signal. Finally, for MI, noise in the propagating optical field is enhanced by the nonlinear refractive index acting as trap for intensity fluctuations, amplifying them. The frequency domain picture of MI is FWM where any phase mismatch is compensated through the action of the nonlinear refractive index [15].

In order to understand SPG, it is not enough to simply identify some of the nonlinear processes involved, such as MI, SPM, XPM and SRS; we also need to understand the dispersion that the propagating optical field experiences due to the wavelength dependence of the refractive index. The dispersion that the optical field experiences affects how the nonlinear frequency generation processes interact with each other and can also cause exotic forms of light propagation such as solitary wave propagation, known as solitons. In the case of guided wave propagation this entails expanding the mode propagation constant from equation 2-13, as a Taylor series [41]:

$$\beta_j(\omega) = \beta_j^{(0)} + \beta_j^{(1)}(\omega-\omega_0) + \frac{1}{2}\beta_j^{(2)}(\omega-\omega_0)^2 + \ldots \qquad 2\text{-}25$$

where $\beta_j^{(n)}$ is the n^{th} order dispersion term of the j^{th} order mode, given by $\beta_j^{(n)} = d^n\beta_j^{(n)}/d\omega^n$ and ω_0 is the centre frequency of the pulse.

Taking the terms in equation 2-25 in ascending order: the zeroth order is equal to the inverse of the phase velocity, which causes a common phase shift; the first order term is equal to the inverse of the group velocity, which causes an overall time delay for a propagating pulse; and the second order term is equal to the derivative of the inverse group velocity, which relates to the dispersive broadening or compression of a pulse in time. Beyond the second order are terms that are collectively referred to as higher order dispersion and must be considered in the case of extremely broadband spectral fields such as those encountered in supercontinuum generation.

Dispersion not only governs the options for generation of new frequencies by phase sensitive parametric nonlinear processes; it also limits the effective interaction length for nonlinear frequency generation by ultrashort pulses. This is because any group velocity mismatch between fundamental and generated pulses gives rise to a temporal walk-off between pulses with different centre frequencies. Temporal broadening of an individual pulse can pose another limit to the effective nonlinear interaction length by the concurrent reduction in pulse peak power leaving the peak power too low for efficient nonlinear interactions.

For SPG, the determination of the second order dispersion is of particular interest because the wavelength at which $\beta_j^{(2)}$ is equal to zero acts a dividing line between two different regimens of light propagation for a particular material, namely the normal ($\beta_j^{(2)} > 0$) and anomalous ($\beta_j^{(2)} < 0$) dispersion regimes. This wavelength is termed the Zero Dispersion Wavelength (ZDW) as a narrowband optical pulse centred on the ZDW experiences no dispersive broadening or compression. In the anomalous dispersion regime, an ultrashort input pulse with centre wavelength just above the ZDW can experience a balance between the normal dispersion caused by SPM and the anomalous dispersion of the propagating medium. This allows the pulse to propagate with a constant or periodic temporal and spectral shape which is known as a soliton [42]. Solitons can also form from longer pulses or CW input if the fields are in the anomalous dispersion regime through MI. Solitons and their evolution, referred to as soliton dynamics which for brevity are omitted, are a main cause of spectral broadening in SPG [43].

As discussed in the previous section the design and material choices for a waveguide determine the propagating modes. As well as properties such as the mode number and

size, waveguide design can also tailor the dispersion properties of the modes they support. The contribution of dispersion from the waveguide design to the chromatic dispersion caused solely by the propagation medium gives the ability to shift the ZDW, create multiple ZDW and create phase matching conditions for wavelengths that would be mismatched in an unguided mode. As well as the opportunities for dispersion engineering, waveguides also offer high field intensities over much longer path lengths than are achievable for free space beams due to beam diffraction creating much longer interaction lengths for nonlinear processes to occur. Considering these benefits is not surprising that waveguides are widely used for supercontinuum sources [41, 43].

Due to the complexity of SPG, numerical modelling is often used to try to understand how the dispersion profile of a waveguide and the multitude of nonlinear processes involved are interacting to produce a broadband output spectrum. This is achieved by modelling the field propagation using the Generalised Nonlinear Schrödinger Equation (GNLSE), which can be derived from Maxwell's equations. The GNLSE comes in many variants depending on the assumptions made on the linear and nonlinear effects relevant for the scenario under study but it has the typical form [44]:

$$\frac{\partial A(z,T)}{\partial z} = \left(\hat{D} + \hat{N}\right) A(z,T) \qquad 2\text{-}26$$

where $A(z,T)$ is the complex field envelope, $\hat{D}$ is an operator describing linear loss and dispersion and $\hat{N}$ is an operator describing the relevant nonlinear effects containing terms such as the nonlinear refractive index and a Raman contribution term.

2.2.3 Resonant Nonlinear Light-Matter Interactions

In the previous sections we have seen how light-matter interactions can lead to new frequencies being generated due to nonlinear light-matter interactions. In these processes the passage of light induces a polarisation response from a dielectric medium by causing the displacement of bound charges. In this section we explore another type of light-matter interaction in which light is absorbed by the medium through the promotion of bound charges, i.e. electrons, to higher energy states.

As was the case for material polarisation, in the low intensity limit light absorption is a linear process. In this regime, the differential absorption of light as it propagates through a homogenous and isotropic absorptive medium follows the relation [45]:

$$\frac{dI}{dz} = -\alpha I \qquad 2\text{-}27$$

where I is the intensity, and α is the absorption coefficient.

Integrating equation 2-27 gives the light intensity as a function of propagation length which is known as the Beer-Lambert law [45]:

$$I(z) = I_0 e^{-\alpha z} \qquad 2\text{-}28$$

where I_0 is the initial intensity.

In the photon picture, linear absorption can be described as promotion of an electron to a higher energy state by the annihilation of a single photon. Because of the quantised nature of both photons and electrons this process can only occur is the photon has sufficient energy to promote the electron to an available free state. As the energy of a photon is determined by its frequency there is a range of frequencies, conversely wavelengths, where incident photons have insufficient energy to be linearly absorbed. This region defines the optical bandgap for a material and in this region the material is nominally transparent to the propagating light ignoring competing attenuation processes such as scattering.

As the light intensity increases the linear relationship expressed in equation 2-27 is no longer valid and the absorption coefficient becomes a function of the incident light intensity:

$$\alpha(I) = \alpha + \beta I + \gamma I^2 + \delta I^3 + \ldots \qquad 2\text{-}29$$

where α is the linear absorption coefficient and β, γ, δ are the two, three and four photon absorption coefficients respectively.

This is analogous to the nonlinear polarisation response seen in equation 2-14, which is unsurprising as the multiphoton absorption (MPA) coefficients can be expressed in terms of the imaginary parts of the odd order complex nonlinear electric susceptibilities. In the photon picture, MPA can be described as promotion of an electron to a higher energy state by the annihilation of multiple photons simultaneously. This transition is allowed by the concept of virtual states which are a consequence of the indeterminacy of quantum mechanical systems, i.e. some classically forbidden transitions are allowed so long as they happen on a timescale shorter than the virtual lifetime of the transition, $\Delta t \sim \hbar/\Delta E$, permitted by Heisenberg's uncertainty principle [46].

In a similar manner to linear absorption, MPA requires the combined energy of photons involved in the MPA process have sufficient energy to promote an electron to an available free state. The optical bandgap of the propagation medium and incident wavelength will therefore set the minimum MPA order that can occur and by sweeping the incident wavelength we can define a MPA edge for each order.

In the presence of very intense fields, another class of nonlinear absorption based solely on the electric field strength of the propagating light and not on the photon energy exists. When the strength of the optical field in a material is comparable to the binding energy experienced by an electron, then the band structure of the material will be distorted. If this distortion can suppress one side of the potential sufficiently, then an electron can tunnel through the potential barrier and out of its bound state.

These two seemingly different nonlinear absorption processes, as depicted in Figure 2-1, were shown to be extremes of the same fundamental process that can be treated under a single framework by Keldysh [47]. Under this framework nonlinear absorption proceeds by MPA at low laser irradiances and high frequencies that remain below the photon energy necessary for single photon absorption. Whereas for high laser irradiances and lower frequencies, the distortion of the band structure in the dielectric by the strong EM field allows for tunnelling to occur. The dominant pathway can be determined using the Keldysh parameter (γ):

$$\gamma = \frac{\upsilon}{e}\left(\frac{m_e c n \varepsilon_0 E_g}{I}\right)^{1/2} \qquad 2\text{-}30$$

where υ is the incident laser frequency, e is the charge of an electron, m_e is the effective electron mass, c is the speed of light, ε_0 is the permittivity of free space, E_g is the bandgap of the material I and is the laser intensity in the focal volume. For $\gamma \sim 1.5$ nonlinear absorption is a combination of both mechanisms, with tunnelling dominating when γ is much less than 1.5 and vice versa.

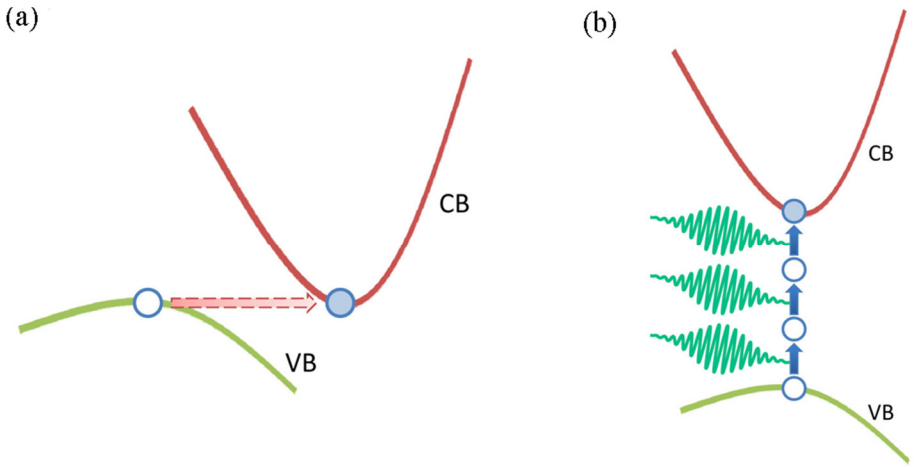

Figure 2-1 *Nonlinear absorption processes in the opposite extremes of high photon energy low field strength, (a) tunnelling process, and low photon energy high field strength, (b) MPA process. VB signifies the valence band and CB signifies the conduction band. Adapted from [48].*

2.3 Ultrafast Laser Inscription

2.3.1 Overview

ULI may be considered as a subcategory of laser machining that expands the capabilities of conventional laser machining by virtue of processing with ultrashort, i.e. femtosecond to few picosecond, laser pulses. Laser machining for applications such as cutting, drilling and patterning has traditionally been performed using continuous wave (CW) lasers or pulsed nanosecond lasers, but in both cases heating effects such as melting restricts the achievable resolution at the nanoscale. More recently picosecond and femtosecond laser systems have been introduced to mitigate the heating effects due to shorter pulses reducing thermal diffusion away from the processed volume. Also, conventional laser processing is performed on materials opaque to the processing wavelength, i.e. in the linear absorption regime. ULI employs ultrashort pulses at wavelengths for which the

machined material is transparent and thus utilises the fundamental nonlinear properties of the material in addition to properties of the machining laser to allow incident pulses to be absorbed.

2.3.2 Physical Process

In ULI, ultrashort laser pulses are focused beneath the surface of a dielectric material and are absorbed due to nonlinear absorption processes. This can lead to an optical breakdown leaving behind permanent structural modification as the electrons transfer energy to the lattice [49]**.** Because the wavelengths of light used in ULI have photon energies insufficient for linear absorption the modification is confined within the focal volume and by translating the sample through the incident beam complex 3D structures can be written due to this tight spatial confinement.

As discussed in the previous section, nonlinear absorption proceeds by MPA or tunnelling with the dominant pathway dependent on the value of the Keldysh parameter. Considering the MPA regime, the ionisation rate, P_r, depends strongly on the laser intensity:

$$P_r(I) = \sigma_n I^n \qquad 2\text{-}31$$

where σ_n is the multiphoton absorption coefficient for n-photon absorption. The nonlinear dependence on intensity means that the ionisation rate is more efficient for shorter pulses with higher peak powers.

If the energy transfer from the laser pulse was caused solely by MPA, the threshold intensity for optical breakdown would vary greatly with bandgap because of the large variation in absorption probability associated with different multiphoton absorption orders. Experimental observations however indicate a low dependence for threshold intensity with bandgap and this can be attributed to the importance of avalanche ionisation which depends only linearly on the laser intensity [50]. In avalanche ionisation, seed electrons provided by initial nonlinear absorption can linearly absorb incident photons to create hot conduction band electrons which subsequently impact ionise valence electrons resulting in two electrons in the conduction band, as depicted in Figure 2-2. This process

can then repeat to cause an electron avalanche and subsequent optical breakdown as the free electron plasma frequency approaches the laser frequency.

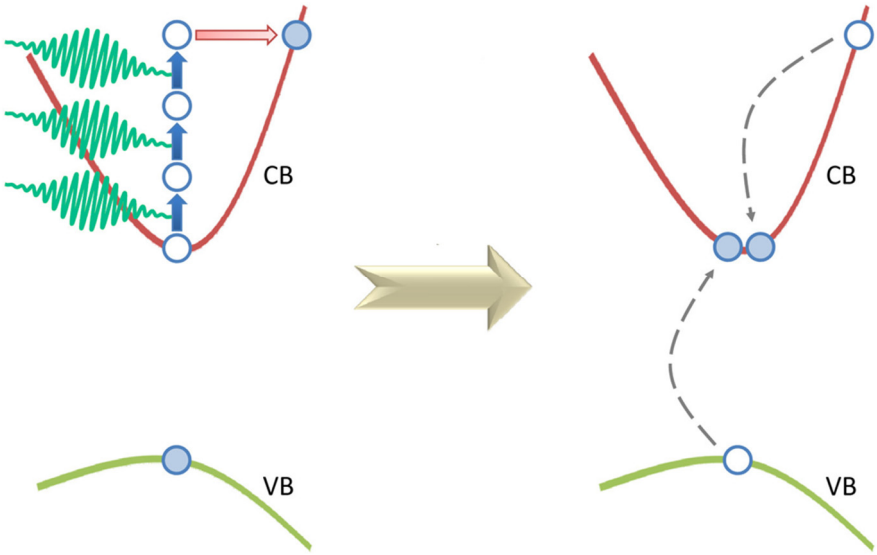

Figure 2-2 *Avalanche ionisation - the two-step process of free carrier absorption followed by impact ionisation. VB signifies the valence band and CB signifies the conduction band. Adapted from [48].*

As seed electrons are provided by the initial nonlinear absorption processes any resultant modification in the material is deterministic because it is not dependent on material defects or dopants. Hence ULI can be used consistently and reliably in a broad range of materials. In contrast with nonlinear absorption processes avalanche ionisation becomes more efficient with longer pulse durations [51].

As well as pulse duration determining the balance between nonlinear absorption and avalanche ionisation it also dictates the mechanisms of material modification. During laser irradiation the absorption of the pulse excites electrons to the conduction band by the previously mentioned processes. The electrons can distribute energy among themselves through carrier-carrier scattering which occurs on a timescale of 10-100 fs providing a fast route to reach an even distribution. They can also redistribute energy to the lattice by carrier-phonon scattering, occurring on a timescales >10 ps [52] equalising the temperature of the electrons and ions in the lattice. On the nanosecond timescale a pressure and/or shock wave can separate from the focal volume if the focal volume

temperature exceeds the material melting and/or boiling point. Beyond this on a roughly microsecond timescale thermal energy diffuses out of the focal volume.

For pulse durations of the order of femtoseconds that are used in ULI lattice heating occurs after the pulse has been absorbed which effectively decouples absorption and lattice heating [49]. This allows for more precise machining and reduces the size of any heat affected zone (HAZ) that can extend beyond the focal volume when longer pulses are used.

The decoupling also leads to a deviation from the scaling of material damage threshold intensity with the square root of pulse duration that is seen for pulse durations >10 ps. Using these longer pulse durations means that significant amounts of energy are transferred to the lattice whilst remnants of the pulse are still present causing the damage threshold to be determined by relative energy deposition rate and thermal diffusion in the material. In contrast, the damage threshold for the ultrashort pulses used in ULI is found to increase by a factor of 3 for every factor of 10 increasing in pulse duration [53].

2.3.3 Waveguides and Inducing Refractive Index Change

In many materials irradiating with pulse energies close to the threshold value for modification, ~ 100 nJ for 0.4 NA focussing of 1045 nm 350 fs duration pulses in fused silica, produces a smooth refractive index change. This has enabled the inscription of guiding structures, with propagation losses as low as 0.053 $dBcm^{-1}$ demonstrated for single mode guides [54]. The index change can be either positive or negative depending on the character of the material change induced by the laser irradiation and is usually on the order of 10^{-3}. ULI is therefore applicable for the fabrication of photonic devices in this regime by either creating higher index regions that act as a waveguide core with the unmodified material providing the waveguide cladding which has become known as type I structures. Or conversely writing a lower index cladding and guiding light in a core region of unmodified material which has been termed the depressed cladding geometry. It is important to note that guided modes in depressed cladding structures are in fact not strictly guided but ‘leaky’ due to the evanescent field of the propagating modes extending into the unmodified region surrounding the cladding [55].

The most widely studied material in ULI is fused silica and for the low pulse energy regime a positive index change is observed. The index change is attributed to several factors, firstly a refractive index increase can be caused by changes in absorption from the formation of dangling bond defects i.e. a Kramers-Kronig relationship from the complex refractive index [56]. This has been verified by the presence of photoinduced absorption peaks at 213 nm and 260 nm. These peaks are characteristic of oxygen-deficient paramagnetic electron centres and oxygen-excess non-bridging oxygen hole centre defects respectively [57]. It has also been shown however that these defects can be erased by annealing at 400 ˚C but waveguide behaviour can be observed with annealing steps up to 900 ˚C.

A second explanation is given by the rapid quenching of melted glass in the focal region freezing in a higher fictive temperature leading to a densification of the glass. In fused silica the density and consequently the refractive index increases when the melt is rapidly cooled from a higher temperature. Raman spectroscopy studies have shown an increase in 3 and 4 member rings in the silica network inside the irradiated zone, indicating densification and supporting this argument [58].

In materials which exhibit reductions in index in the focal volume shock wave propagation is often tabled as the reason as this creates a rarefied region at the focus. With increasing pulse energies shockwave propagation can lead to voids, even in materials such as fused silica which at lower pulse energies exhibit positive type I modification. Voids have application in 3D memory storage and can be produced using > 1 μJ 350 fs pulses with 0.4 NA focussing of 1045 nm light in fused silica. By inscribing parallel tracks of void ‘damage-like’ modification guiding can also be attained due to the induced strain from material expanding out from the focal region in a geometry known as type II guiding. The guiding geometries discussed are summarised in Figure **2-3**.

In multi-component glasses such as crown glass, index change allowing for waveguide inscription has been shown to have contributions from ion-exchange between the network formers and network modifiers in the glass [59]. This highlights a potential concern for type I waveguide inscription in doped materials for active devices such as compact amplifiers and laser sources, as there is potential for lasing ions to migrate from the modified region. For this reason and to keep lasing characteristics, which are effected by

the lasing ions local environment, similar to bulk samples type II and depressed cladding structures are ideal as the guiding region has not been modified [60, 61].

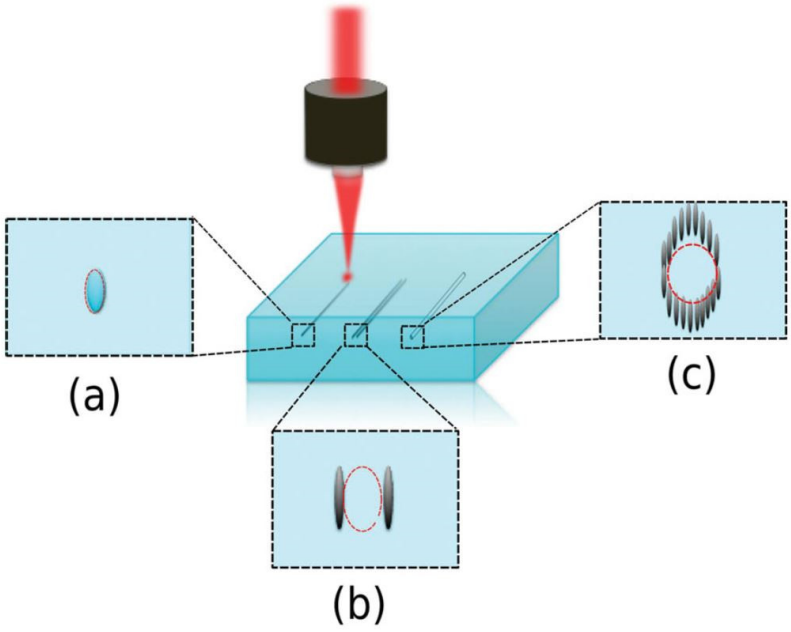

Figure 2-3 *Laser inscription of guiding structures with magnified inserts of waveguide cross-sections for (a) type I, (b) type II, and (c) depressed cladding waveguide structures. The guiding region for each type is indicated using red dashed lines. It is important to remember that the achievable modification type is material dependent as well as a function of fabrication parameters. Therefore, it is often not possible to fabricate all three types of waveguides in the same sample. Adapted from [62].*

2.3.4 Micro-channels and Selective Etching

The direct fabrication of microfluidic channels can be implemented by the technique known as Femtosecond Laser Irradiation followed by Chemical Etching (FLICE) which has also been termed Femtosecond Laser-Assisted Etching (FLAE). This technique consists of two steps: the irradiation of the sample with focussed femtosecond laser pulses and then etching by a suitable etchant [63]. The technique is possible because the structural changes induced during ULI can impact the chemical properties of the material as well as changing its optical properties. Providing a suitable contrast in etching rates is brought about in the modified regions they can either be preferentially removed or chemically resistant compared to the unmodified bulk allowing for 3D structures to be machined. In the case of inscribing areas which are more susceptible to etching chemicals; complex buried micro- and nano-scale channels can be fabricated in the bulk of a

dielectric sample. Also, as the material structural changes induced by ULI for waveguide writing and micro-channel formation can be performed by the same inscription laser, ULI has the unique ability to take these features and implement them on the same substrate to create opto-fluidic devices with a single inscription step.

FLICE has been achieved in both vitreous and crystalline materials with particularly high etching selectivity observed in crystalline materials, as an example etching selectivity of $1{:}10^4$ has been observed in sapphire [64]. The preferential etching can be linked to the material structure disparity between a "perfect" crystalline lattice and amorphized modified regions and this is often presented as the origin of the large etch rate contrast [65].

In glassy materials the structural difference between modified regions and bulk can be less distinct but etching selectivity can still be observed. Again fused silica has been the most broadly examined material with studies demonstrating a linear relationship between index change and etch rate for laser inscription parameters used to create type I waveguides [66]. The etching selectivity in this parameter space is low with modified to bulk etch ratio of approximately 1:10 which is credited to reductions in Si-O-Si bond angles caused by densification leading to a weakening of these bonds, compressive stress and the presence of laser induced defects.

Another interesting laser inscription regime for fused silica has been identified for pulse energies larger than those used for smooth modification and below pulse energies for disruptive modification i.e. ~ 150 - 700 nJ for 0.4 NA focussing of 1045 nm 350 fs duration pulses. In this parameter window nanostructures can be formed inside the focal region with feature sizes smaller than the wavelength of incident laser light. The nanostructures consist of periodic nanocracks that are aligned orthogonally to the laser polarisation and have found application in specialty optics as they exhibit form birefringence [51]. These nanocracks also permit the flow of etching chemicals along laser modified regions vastly increasing the preferential chemical etching contrast to selectivities in the order of $1{:}10^3$.

The mechanism behind nanocrack formation has been widely studied and several models have been presented to explain their formation. The first model proposed built on

traditional surface ripple formation theory for periodic structures found on sample surfaces during laser machining and expanded this to modification of the sample bulk [67]. The nanocrack formation in this model is reliant on the interference between Langmuir waves in the free electron plasma generated in the focal volume and the incident laser pulse electric field. This bulk plasma wave interference model has been used to successfully predict the decrease in nanocrack grating period with pulse energy [67].

Another model for nanocrack formation is known as the transient nanoplasmonics model, as summarised in Figure 2-4, which proceeds by inhomogeneous nonlinear absorption in the focal region due to the presence of defects or colour centres. The areas of higher nonlinear absorption form into spherical nanoplasma droplets over subsequent pulses due to feedback based on memory of previous nonlinear ionisation, which is equivalent to an effective bandgap reduction in the region [68]. This makes the region easier to ionise on the next laser pulse. The nanoplasma droplets then grow in size with increasing pulse number in an asymmetric manner owing to field enhancement at the boundaries of the nanoplasma enhancing the ionization rate at the equator.

The nanoplasma droplets become nanoellipsoids because of the asymmetric field enhancement with major axis in the direction of laser propagation. Continued growth of the ellipsoids and merging of neighbouring ellipsoids leads to nanoplanes which are initially randomly spaced in the focal volume. With successive laser pulses the electron plasma density inside the nanoplanes reaches the critical point for the planes becoming quasi-metallic, i.e. optical breakdown, and at this stage the cracks act as quasi-metallic waveguides that assemble with a spacing of $\lambda/2n$ where λ is the vacuum incident laser wavelength. This last stage is important in describing the observed long-range order of nanocracks.

As the alignment of laser induced nanocracks is perpendicular to the polarisation of the incident laser pulse; polarisation control gives another parameter to limit or increase etchant ingress into modified regions to alter etching rate. Nanocracks have now been observed in other silicate glasses [69] and single crystal tellurium oxide [70] signifying this level of control is possible in other materials.

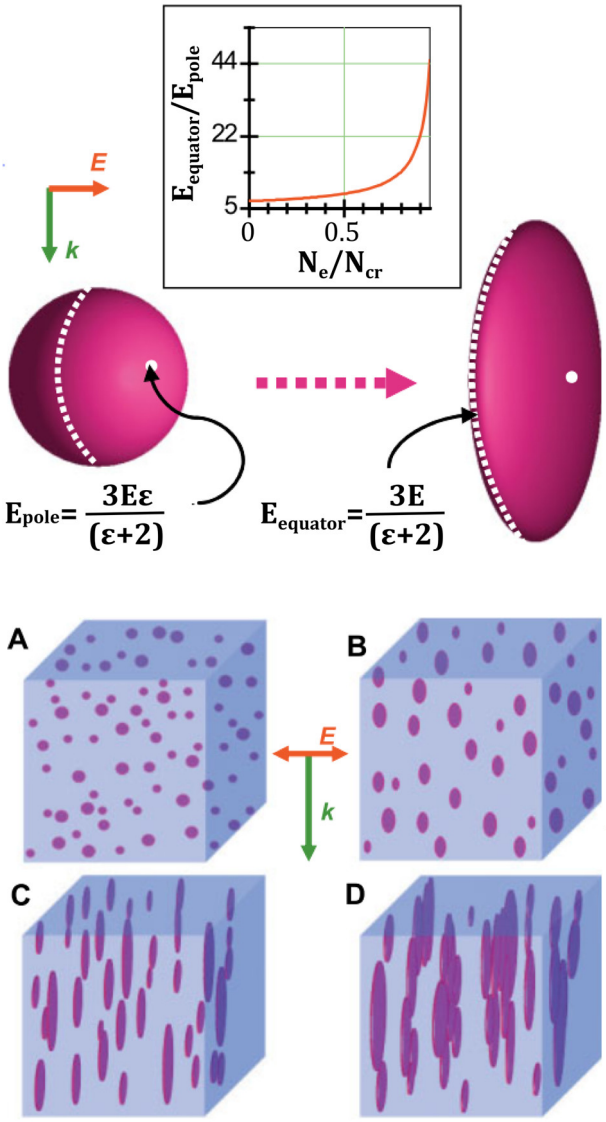

Figure 2-4 *Top: Asymmetric field enhancement at two locations on a nanoplasma under the influence of the laser electric field, E. The relative permittivity, ε, is the ratio of the real part of the nanoplasma permittivity to the dielectric function of the medium that surrounds the nanoplasma. N_e is the plasma density and N_{cr} is the critical plasma density. For an under-dense plasma, i.e. $N_e<N_{cr}$, field enhancement occurs as seen in the central graph. Bottom: Evolution of nanoplasmas into nanoplanes. Randomly distributed under-dense nanoplasma droplets (droplet size is a few tens of nanometres) grow asymmetrically in the presence of the laser field over hundreds of laser pulses to become ellipsoidal and finally flatten and merge to become micrometer sized nanoplanes. Adapted from [71].*

2.4 Material Properties

In pursuance of the fabrication of mid-IR optics, suitable materials must be identified that transmit into the mid-IR. The following section discusses the salient properties of two such classes of material that feature in this thesis, namely chalcogenide glasses and crystalline sesquioxides.

2.4.1 Chalcogenides

Chalcogenides glasses are a key class of amorphous semiconductors which find applications in areas as diverse as photonics, lithography, sensing and phase change memories. They contain one or more of the chalcogen elements, which form the sixteenth group of the periodic table (oxygen (O), sulphur (S), selenium (Se), tellurium (Te) and polonium (Po)), as a major constituent. In the context of glass families, oxygen and polonium are not included in the chalcogenide grouping as oxide materials demonstrate very different chemical, optical and electrical properties and polonium is unstable [72]. Chalcogenide glasses typically contain one or more of the network forming elements: arsenic (As), germanium (Ge), phosphorous (P), antimony (Sb) and silicon (Si); covalently bonded to the chalcogen element(s) to form a bulk glass structure that is held together by a combination of covalent bonding and van der Waals forces. This is in contrast to the ionic bonding in other glasses.

On the atomic scale the chalcogenide glass structure can be understood as a continuous random network that is quantified by a mean co-ordination number (MCN). This parameter takes the concept of a co-ordination number for each atom, i.e. the number of surrounding atoms each central atom is bound to by single or multiple bonds, and applies it for the bulk by summing the products of the mole fraction of each constituent element and their valence [73]. Chalcogenide glasses exhibit wide glass forming regions for example the ratio of arsenic to sulphur in the As-S glass system can be varied from 1.5 to 9 [74] . The MCN gives a parameter that can be tracked as the ratios of the glass elements are varied to define transitions in material properties such as network topology, refractive index, density, nonlinear response and bandgap.

The weaker bonding of chalcogenide glasses causes the short wavelength band edge from electronic absorption to shift to the visible or near-IR wavelength range in comparison to the near-UV for oxide glasses like fused silica. Whereas the long wavelength cut-off from

multiphonon absorption lies much further into the IR due to low phonon energies from the combination of heavier mass elements and weak bonding, as shown is Figure 2-5. Between the chalcogen elements themselves the heavier the atomic mass or increasing their abundance in the glass both act to reduce the average bond strength further, to the determinant of material properties such as hardness, strength and glass transition temperature. Although lowering the transition temperature does allow for the moulding of intricate components such as aspheric lenses as a route for low-cost manufacture.

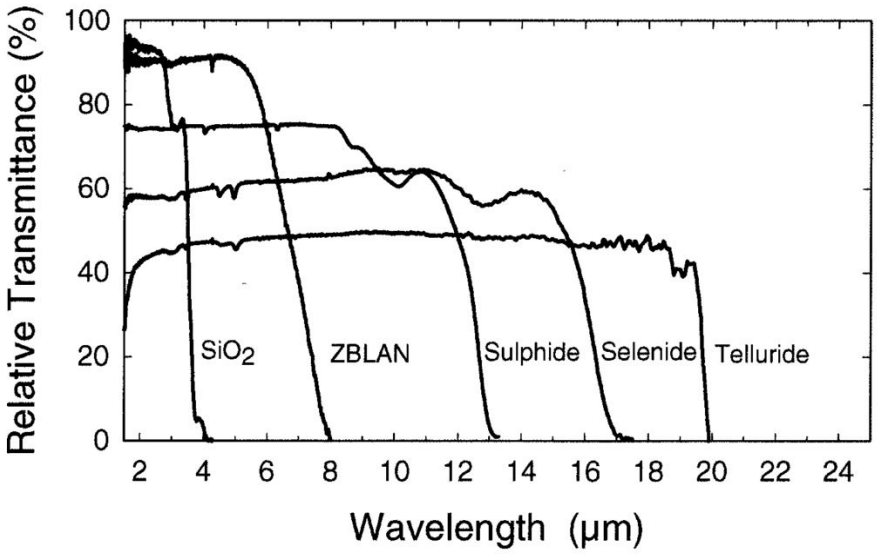

Figure 2-5 *Infrared transmission for bulk glass samples of SiO_2 (fused silica), ZBLAN (a multicomponent fluoride glass) and representative chalcogenide glasses. Silicon, not shown in this figure, has a long wavelength cut-off at around 7 μm. Reduction in the overall transmission for heavier chalcogen containing glasses is tied to Fresnel losses due to their higher refractive indices.*

Chalcogenide glasses possess relatively large linear refractive indices from around 2 to greater than 3. This stems from their higher density relative to oxides and the strong polarisability of the chalcogen elements. The refractive index increases in tandem with long wavelength transmission when moving to heavier chalcogen elements. For photonic circuit fabrication the high refractive index is beneficial as it allows compact waveguide circuits due to strong optical field confinement which also provides enhanced optical intensities for nonlinear applications. High refractive index and low phonon energies also makes chalcogenides attractive as hosts for rare earth ions as they provide high radiative rates for the rare earth transitions whilst simultaneously reducing non-radiative multi-phonon transitions [72].

Tied to their large linear refractive indices is an increase in chalcogenides' nonlinear refractive index which can be orders of magnitude larger than fused silica [75]. This has led to extensive studies of the nonlinear optical properties of chalcogenide glasses for their applicability in areas such as optical processing and supercontinuum generation, as summarised in Table 2-1.

Table 2-1 *Nonlinear optical constants for a selection of chalcogenide glasses. Where λ_m is the wavelength used for measurement, n_0 and n_2 are the linear and nonlinear refractive indices respectively, β is the two-photon absorption coefficient and FOM is the figure of merit given by the ratio $n_2 / \beta\lambda$ which parametrises the nonlinear phase shift attainable over one two-photon absorption length. Experimental uncertainty for the measurements where given: a ± 18 %, b ± 3 nm, c ± 1.6 %, d ± 17 %, e ± 1.7 %.*

Glass Composition	**λ_m (μm)**	**n_0**	**n_2 (10^{-18} m^2/W)**	**β (10^{-11} m/W)**	**FOM**	**Band Gap (nm)**	**Refs**
$As_{40}S_{60}$	3	2.42	5	-	-	620	[76]
$As_{40}Se_{60}$	1.5	2.8	13	0.4	2	700	[75]
$Ge_{30}Se_{70}$	1.06	-	21[a]	1.1[a]	0.9	705[b]	[77]
$Ge_{25}Se_{65}Te_{10}$	1.5	2.5	5.7	0.4	1	715	[75]
$Ge_{28}Se_{60}Sb_{12}$	1.5	2.6	9.4	0.2	3	690	[75]
$Ge_{10}As_{10}Se_{80}$	1.06	-	22[a]	2.7[a]	0.39	760[b]	[77]
$65Ga_2S_3$:$32La_2S_3$: $3La_2O_3$	1.52	2.41[c]	2.16[d]	<0.01	>7.1	545[e]	[78]
$70Ga_2S_3$:$30La_2O_3$	1.52	2.25[c]	1.77[d]	<0.01	>5.8	500[e]	[78]
$70Ga_2S_3$:$15La_2O_3$: $15LaF_3$	1.52	2.26[c]	1.39[d]	<0.01	>4.6	497[e]	[78]
$68Ga_2S_3$:$32Na_2S$	1.52	2.14[c]	1.01[d]	<0.01	>3.3	473[e]	[78]

Chalcogenides glasses also exhibit numerous photoinduced effects which can be grouped into many different categories depending on the change in electrical, structural, mechanical, chemical and/or optical properties [79]. These changes can further be

classified as permanent or reversible and as either scalar or vectorial, i.e. unaffected or affected by light polarisation.

Photocrystallisation or amorphisation is one such effect and is utilised in phase change memories. The phase change proceeds due to heating upon optical illumination to temperatures greater than the crystallisation temperature of the glass. This can then be reversed by heating above the melting temperature and quenching using a secondary illumination step or by electrically heating the crystallised volume.

Photopolymerisation is the process of optically induced polymerisation, i.e. the creation of more complex molecules from smaller repeating subunits in the glass. The polymerisation of the glass network in chalcogenides, like As_2S_3, which have been deposited by thermal evaporation dramatically affects its solubility in amine solvents and has been used for the creation of glassy resists for lithography [80].

Photodissolution of metals is another effect and has been shown to occur when samples are coated with thin metallic layers and illuminated with near bandgap light. This process is not easy to reverse and is another route to significantly change the etching selectivity of the illuminated regions [80].

Photocompaction and photocontraction are two more photoinduced effects with the latter being reversible under thermal annealing and the former being shown to induce a refractive index change in gallium lanthanum sulphide (GLS) glass of around 10^{-3} due to density changes and increase of lanthanum concentration in the illuminated area. Utilising this index change, surface waveguides in GLS have been demonstrated [81]. Conversely photoexpansion has also been observed in different chalcogenide glass systems.

Photodarkening and photobleaching occur with the redshift and blueshift of the optical absorption edge respectively due to structural changes that differ from the photodarkening processes in some oxide glasses where defects such as colour centres can appear as optical absorption peaks, with the absorption edges left intact [76].

Photoinduced anisotropy can occur with some chalcogenides exposed to linearly polarised light demonstrating dichroic redshift of absorption edges and birefringence that can be removed by exposure to unpolarised light.

All of these light-induced changes are sensitive to the glass preparation method with thin films particularly susceptible to large photoinduced changes due to the non-equilibrium nature of as-deposited material. Thus, irreversible effects predominately occur in as-deposited films, while reversible effects typically occur in well-annealed films as well as bulk glasses. It is also possible to demonstrate contrary effects subject to deposition conditions such as photodarkening and photobleaching in AsS films depending on the specifics of the glass preparation method. For low intensity illumination, changes in material properties are observed for near bandgap light, with longer wavelengths reliant on high intensity to initiate the photoinduced changes.

Due to their mid-IR transparency, large nonlinear response and range of photo-induced effects, chalcogenides are an ideal substrate for mid-IR integrated optics. Devices such as integrated optics beam combiners can take advantage of their transmittance across the whole mid-IR range and their large nonlinearities can enable compact supercontinuum sources. Light induced material property changes such as photopolymerisation hint at the possibility of structuring chalcogenides using the FLICE methods discussed in the previous section which would allow for mid-IR optofluidics. However, in any photonic device based on chalcogenides it is important to consider the range of photoinduced effects that may occur because as well as enabling some fabrication techniques or device functions they can also be detrimental to device performance.

2.4.2 Sesquioxides

Sesquioxides are a class of oxide materials with a chemical composition of three oxygen ions to two metal ions. Many crystals exhibit this ratio and some are already in widespread use for photonics applications. One such example is sapphire (Al_2O_3) which as a host crystal doped with Titanium ions is the gain medium of choice for femtosecond laser systems which are the workhorse of ultrafast optics labs worldwide.

Amongst the sesquioxides are an emergent set of laser host crystals with cubic symmetry, namely Lutetia (Lu_2O_3), Scandia (Sc_2O3) and Yttria (Y_2O_3), which have shown excellent

bulk lasing performance in the mid-IR when doped with rare earth ions in CW and pulsed operation [82, 83]. These crystals also form solid solutions with one another allowing for any mixture of the form $(Lu_aSc_bY_c)_2O_3$ where a + b + c = 1. As a result of their comparable laser performance, Lu_2O_3, Sc_2O_3, Y_2O_3 and their mixtures are nominally referred to as the sesquioxides for the remainder of this thesis which has become the convention in the wider field of photonics as well. Due to their shared cubic symmetry, the material properties of the sesquioxides are often compared with YAG which is perhaps the most well-known and widespread laser crystal. Some of these key material properties for sesquioxides and YAG are summarised in Table 2-2.

Table 2-2 Summary of important properties of lutetia, scandia, yttria and yttrium aluminium garnet for photonics applications. Superscripts refer to dopant ions where: a - thulium-doped, b holmium-doped, c - average across common rare earth dopants. Doping concentrations are stated in atomic percentages signified using %at. notation. * - values correspond to double the atomic percentage doping in sesquioxides as this provides a comparable dopant ion density..

Material Property	**Lu_2O_3**	**Sc_2O_3**	**Y_2O_2**	**$Y_3Al_5O_{12}$**	**Refs**
Refractive index @ 1 μm	1.911	1.966	1.889	1.816	[84, 85]
@ 2 μm	1.896	1.946	1.874	1.801	[84, 85]
@ 3 μm	1.883	1.926	1.860	1.783	[84, 85]
Transmission (μm)	0.225-8	0.210-8	0.220-8	0.210-5.2	[84, 86, 87]
Thermal Conductivity (W/m·K)	12.8	18	13.4	13.4	[86, 88]
@ 1 %at.	12.6^a	9.1^b	10^c	6^a - 2%*	[88, 89]
@ 5 %at.	11.3^a	5.5^c	6.4^c	5.3^a - 10%*	[88, 89]
Thermo-optic coefficient (10^{-6}/K)	9.1	8.9	8.5	9.1	[84, 85]

In comparison with YAG, the sesquioxides exhibit a similar refractive index but offer a broader transmission bandwidth. As sesquioxides have a comparable optical bandgap to YAG and therefore a similar visible transmission edge, their broader transparency range

comes from a deeper IR transmission edge [86, 87]. This is particularly advantageous for mid-IR laser sources as it results in reduced rates of non-radiative decay of the mid-IR transitions of dopant ions.

In doped or undoped crystals the thermal conductivity of sesquioxides is comparable or higher than YAG. Although offering the poorest thermal conductivity values of the sesquioxides for undoped crystal, Lu_2O_3 is seen to have a nearly constant thermal conductivity with increasing dopant ion concentration whereas for YAG this decreases sharply [90]. This has been shown to be down to the similarity in size of the common optically active rare earth ions to lutetium, which allows for minimal disruption of the lattice structure and hence minimal phonon scattering [91]. The negligible effect on the thermal conductivity Lu_2O_3 under high doping has stability benefits for high power laser applications and for high gain compact sources.

All the sesquioxides can be doped with rare earth ions in high concentration because, as is the case of the mixed sesquioxides, oxides of optically active rare-earth metals also form solid solutions. This allows for doping of any atomic percentage from 0 to 100% [89]. The presence of two rare-earth ions sites in the formula unit of the sesquioxides and their lattice spacings of around 10 Å, leads to dopant ion densities roughly twice as large as seen in YAG [92]. The dopant ions also experience a strong crystal field causing pronounced Stark splitting which can be seen in unusually long emission wavelengths and broad emission bandwidths for laser ions in sesquioxide hosts, especially Sc_2O_3 [93].

The mixed sesquioxides can offer even broader and deeper IR emission than pure Lu_2O_3, Sc_2O_3 or Y_2O_3 as their disordered structure leads to a wider range of possible environments for the laser ion. Though, the enhanced breath of the emission bandwidth comes at the expense of lower peak cross sections and a decrease of the thermal conductivity to less than the average of the individual pure sesquioxides [88]. The broadening of dopant laser ion emission makes rare-earth doped pure and mixed sesquioxides attractive as gain media for mid-IR tunable CW and ultrashort pulse sources.

Furthermore, due to the cubic lattice of the sesquioxides they can be fabricated in the form of laser ceramics [94] that offers a potential for size scalability and cost effective production. Laser ceramic manufacturing involves the cold, high pressure pressing of a

powder filled mould of a desired shape followed by sintering under vacuum for a number of hours to form the ceramic sample and then final processing and polishing [95]. This process of producing sesquioxides laser elements has the advantage over the Heat-Exchanger or Nacken-Kyropoulos methods in that it has a shorter manufacturing time and requires a lower temperature whilst still being able to closely match the physical properties and laser performance demonstrated with single crystals [96, 97].

Sesquioxides' mid-IR transparency, ability for arbitrary rare earth doping concentrations, good thermal conductivity and suitability for fabrication as laser ceramics make them ideal substrates for mid-IR integrated optics. Active devices such as chip scale waveguide lasers can utilise the broadened and deeper IR emission from dopant ions in sesquioxide hosts to create compact tunable and high repetition rate pulsed sources in the mid-IR.

2.5 Summary

This chapter has sought to explain the physical mechanisms behind waveguides, nonlinear frequency generation and nonlinear absorption. We have also discussed supercontinuum generation and highlighted specific nonlinear processes that lead to supercontinuum and the effects of dispersion. A description of ULI as a fabrication technique has been provided including the processes by which light is absorbed and also the timescales and routes in which this absorbed energy is distributed. Material modification regimes suitable for photonic and microfluidic devices are discussed with a particular focus on fused silica which has been the pre-eminent researched material in the field. The final section presented the pertinent material properties for photonics devices of the main material classes used in this work and suggests devices based on these properties.

Background theory and knowledge of material properties has steered the direction of this work and informed the investigations undertaken. For their demonstrated highly nonlinear nature and susceptibility to light induced material property changes chalcogenides were selected for optofluidic device fabrication trials and waveguide supercontinuum trials. For their demonstrated bulk lasing performance in the mid-IR, crystalline sesquioxide ceramics were selected for mid-IR waveguide lasing investigations.

Chapter 3 Laser Processing Rig

This Chapter describes the design, build and commissioning of an advanced laser processing setup at FCAP suitable for ULI whilst being adaptable for other laser processing techniques. An initial section gives an example of a typical ULI experimental setup along with the practical considerations concerned with ULI fabrication. The design considerations that allow for enhanced control over machined microstructures are also discussed. Following this, the hardware procured and control software design is described with each decision supported by a reasoned argument as to why that choice was made. Finally, the initial outputs from the system are presented and the system performance summarised. A user guide detailing the setup, use and shutdown of the laser processing setup at FCAP is included at the end of this thesis which gives further system information.

3.1 ULI Setup Considerations

ULI benefits from having a flexible inscription setup as the optimum inscription parameters for a particular material, be it for waveguides or other micro-structuring, can require the tailoring of many factors, typically: pulse repetition frequency (PRF), pulse duration, pulse energy, focussing, sample movement speed and polarisation. Equally important is the system stability and repeatability, as the nonlinear nature of the pulse absorption in ULI can place tight bounds on the range of fabrication parameters necessary for deterministic and consistent device manufacture. Consequently, an inscription setup that is not subject to drifts and fluctuations in fabrication parameters is also vital in enabling process development to identify optimum inscription parameters. In the first instance, this requires a highly stable laser source, but it is also essential that all the other system components introduced to modify the laser output and deliver the output to the sample do not adversely affect the system stability and reproducibility.

ULI has been widely performed with laser systems using titanium-doped sapphire crystals as the lasing medium. Typical Ti:sapphire laser oscillators have PRFs in the tens of MHz with output pulse durations on the order of 50–100 fs and pulse energies in the tens of nanoJoules. The high repetition rates mean these systems lend themselves to greater throughput but nanoJoule pulse energies necessitate high NA focussing objectives to reach the intensities required for nonlinear absorption, the disadvantages of which will be discussed on in this section. Higher energy laser oscillators are becoming available, but

it is typically necessary to use regenerative amplified Ti:sapphire systems. For ULI the regenerative amplification step is a compromise as it reduces the system PRF to the kHz range increasing device fabrication time and imposes an upper limit on an important laser inscription parameter which could be otherwise be tuned. The introduction of microJoule pulse energy MHz repetition rate Yb-doped fibre and hybrid fibre-solid state lasers for ULI has been an important step as these systems address the pulse energy - repetition rate compromise and due to longer pulse durations in the hundreds of femtoseconds, dispersion control in setups is less important.

A schematic of a typical ULI setup which meets the criteria for stability and flexibility is shown in Figure 3-1. It contains an ultrafast laser system with adjustable pulse compressor and automated control optics for regulating the character of the incident laser light on the sample during device fabrication.

Starting from the far left of the beamline the first component is a shutter which can be closed to allow for traversal around a sample substrate without inscribing structures. The shutter also allows for other inscription parameters to be changed during a run to combine different components on the same substrate, for example a change of polarisation for writing waveguides or microfluidic channels. Following the shutter is the power control optics which uses a half-wave plate for rotating the linearly polarised laser output before entering a polarising beam splitter to control pulse energy. The feedback for this controller is provided using a standard beam splitter to pick of a small fraction of each transmitted pulse which is measured with a calibrated detector.

After the power control there is an acousto-optic modulator which allows for pulse repetition rate changes by integer division of the source repetition rate, control over the number of pulses incident on a sample, the creation of pulse trains and fast on/off switching of the incident laser light for applications such as inscribing Bragg gratings [98]. The next controller in the beamline is a half-wave plate and quarter-wave plate pair for rotating the linearly polarised light and if necessary converting to circularly polarised light. The final components in the beamline consist of a set of mirrors to direct light onto the sample through a final changeable focussing objective. The sample itself is mounted onto a set of high precision translation stages with sub-micron accuracy and tens of centimetre range of travel, which is a requirement for the creation of complex structures.

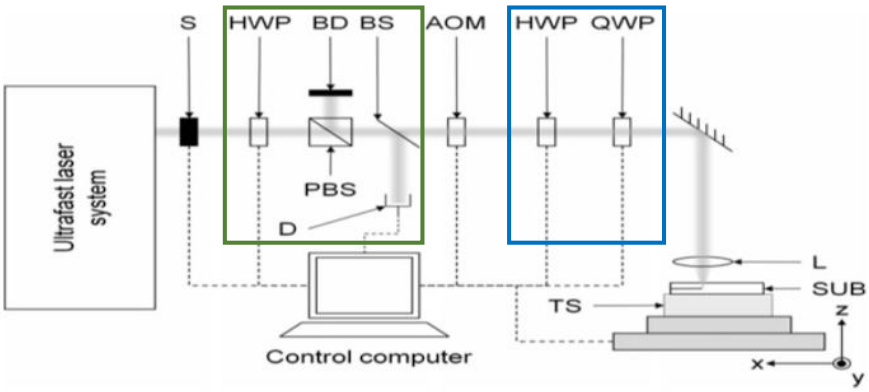

Figure 3-1 *Block diagram of a generic ULI setup, where: S - shutter, HWP - half-wave plate, PBS - polarisation beam splitter, BD - beam dump, BS - beam splitter, D - detector, AOM - acousto-optic modulator, QWP - quarter-wave plate, L - lens, SUB - substrate material, TS - translation stages. Green box contains power control optics and blue box contains polarisation control optics. Adapted from [99].*

Diffraction limited focussing of a Gaussian beam creates an asymmetric focal region as seen in Figure 3-2 by the relations for depth of focus, also known as the confocal parameter, ($2z_r$) and spot size ($2\omega_0$):

$$2z_r = 2\frac{nM^2\lambda}{\pi NA^2} \qquad 3\text{-}1$$

$$2\omega_0 = 2\frac{M^2\lambda}{\pi NA} \qquad 3\text{-}2$$

where z_r is the Rayleigh range, ω_0 is the beam waist radius, M^2 is the Gaussian beam quality factor, NA is the numerical aperture of the focusing lens, λ is the vacuum laser wavelength and n the refractive index.

Therefore $2z_r/2\omega_0 = n/NA$ is the magnitude of the asymmetry which can only be corrected by combination of low index substrates and high NA lenses. This presents problems for machining structures such as waveguides and microfluidic channels, which may require circular cross-sections, using ULI as high NA lens have limited working distances that restrict machining depth and are more prone to spherical aberrations caused by the index mismatch at the air-glass interface. Index mismatch causes a strong depth dependence for ULI buried structures [100] that is less pronounced for lower NA lens or can be eliminated by index matching with oil immersion lenses or by using dry objectives with aberration

correction collars [101]. Additionally, writing in materials with larger linear refractive indices, *n* greater than 2, is of interest for nonlinear photonic applications due to the semi-empirical Miller's rule between linear and nonlinear electric susceptibility [37]. For these materials index matching is not an option and spherical aberrations for tight focussing into samples can be severe [102].

The simplest solution to fabricate structures with circular cross sections comes from the selection of inscription geometry which can be either longitudinal or transverse to the writing beam. ULI relies on drawing the sample through the focal region and so if sample movements are made longitudinally with respect to the laser beam, i.e. along the propagation direction of the beam, a circular cross section can be achieved. The drawbacks to this solution are the challenges in writing curved waveguides without introducing asymmetry and that the short working distances (WD) of typical focussing objectives, e.g. WD ~ 5 mm for NA of 0.45, limit the overall length of inscribed structures. Structure length can be improved through several methods, such as using low NA lens and inscribing with filamentary propagation that occurs due to self-focussing brought on by the higher pulse peak powers required to reach threshold intensity for modification [103]. Another technique is to replace the focussing objective in a standard ULI setup with an axicon to create zero-order Bessel beams with a large depth of focus.

The advantages of a transverse writing geometry in terms of device complexity, e.g. multicore fan-outs [104], and size, only limited by stages, mean that there has been a tremendous effort in developing methods to control inscribed cross-sections. A common resolution has been the modification of the inscription laser beam in order to equalise the depth of focus and spot size, although the way this has been achieved has varied greatly.

The first method demonstrated is known as the astigmatic beam shaping technique and uses a cylindrical lens telescope to control the shape of the modified region. The premise behind the technique is that when writing in the transversal sample plane the modified region width is independent of the beam waist in the direction of writing. Exploiting this fact by tightly focussing in the axis of sample translation, the parallel axis, reduces the depth of focus of the beam, then by adjusting focussing in the axis perpendicular to sample translation, the perpendicular axis, a quasi-symmetric focal plane is attained in this axis [105]. Unfortunately beam waist ratios of ~ 10 are required to produce the

symmetric focal plane and this in turn requires a highly de-magnifying telescope introducing alignment difficulty and aberrations. Optimising the focal plane symmetry would also require changing the lenses in the telescope. In order to overcome this, a slight variation on the technique was demonstrated whereby adjusting the axial position of the second lens in the beam shaping telescope moves the position of the focus in each plane i.e. the astigmatic difference. The area of highest intensity in the beam, i.e. the area where material will be modified, is fixed by the tight focusing in the parallel axis with the astigmatic difference tuned to provide a symmetrical intensity distribution in the perpendicular axis plane. This allows for structures with circular cross sections to be machined with beam waist ratios of only 2-3 [105].

A simplification of this scheme, known as the slit beam shaping method, has also been demonstrated [106]. It is conceptually very similar to the astigmatic method as it relies on controlling the beam waist size in the parallel and perpendicular axes but the experimental setup is much easier to implement. By placing a variable width slit in front of the final focusing objective in a ULI setup, control of the NA in the perpendicular and parallel planes is gained by governing the diameter of the beam in each plane at the objective. A slit with fixed length and variable width therefore controls the beam waist ratio and can be easily adjusted with a micrometer to produce a symmetrical intensity distribution in the perpendicular plane, as seen in Figure 3-2. This method has been very successful in producing circular cross section channels and waveguides [106, 107].

The slit and astigmatic beam shaping methods have been shown to produce structures with circular cross section and both address the issue of structure length in comparison to the longitudinal inscription geometry. On the other hand, and due to their similarities, they both suffer from two major drawbacks, namely: the inability to easily change inscribed structure cross section during writing and that the inscribed cross sections will change for features with bends as the perpendicular and parallel writing axes move with respect to the fixed telescope and/or slit. Adaptive optics have since been used to enhance the slit beam shaping method to overcome these shortcomings, with either deformable mirror [108] or spatial light modulator (SLM) [109] elements inserted into the beamline to generate an image of a slit at the back pupil plane of the final focusing objective. Using adaptive optics allows for control over the slit width in real time for changing structure

cross sections on the fly and also allows the "slit" to synchronously follow the writing direction to preserve cross-sections during bends.

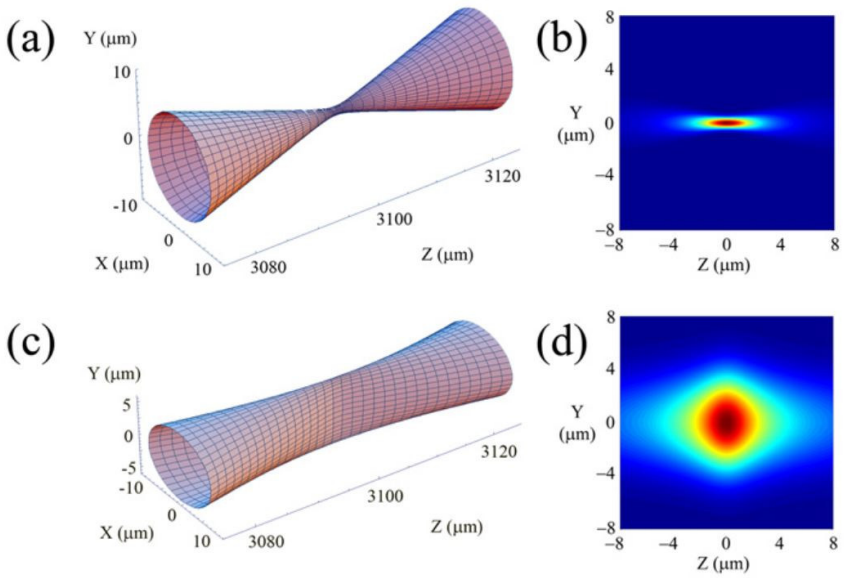

Figure 3-2 *Modelling of beam profiles and energy distribution for focussed beams into glass with n = 1.54 using a microscope objective with NA = 0.46 and 500 μm wide slit. (a) beam evolution near focus not using slit, (b) energy distribution in YZ plane not using slit (c) beam evolution near focus using slit, (d) energy distribution in YZ plane using slit where x corresponds with the direction of the beam translation (parallel axis). Adapted from [106].*

Every solution presented so far for cross-section control has introduced various degrees of complexity and/or expense into the basic inscription setup presented in Figure 3-1. There are however two other schemes in use, the first is based on multiple scanning to define a modified region which is known as the multiscan technique. The method uses no beam shaping optics in the ULI setup and hence each line of modification inscribed in a material carries the elliptical profile imparted on it by the asymmetry of the focal region. The asymmetry of individual scans lines is corrected by multiple passes of the sample through the focus with a small lateral offset, usually $^1/_2$ - $^1/_3$ of the spot size. In this manner structures such as type I waveguides with a square step-index cross section have been demonstrated exhibiting single mode guiding [110, 111]. One added benefit of the multiscan technique for type I waveguide inscription is that as the cross section of the guiding region is built up over multiple scans, the pulse energy used can be kept close to the threshold value for modification potentially reducing the number of scattering and absorbing defects.

The second non-beam shaping solution uses the high PRFs afforded by fibre lasers and solid-state oscillators to create a more uniform area of modification. As previously stated, thermal diffusion of heat out of the focal volume occurs on an approximately microsecond timescale and is dependent on the intrinsic thermal diffusivity of the material. For PRFs in the high hundreds of kHz or MHz a transition from a single pulse regime, where each pulse absorbed can be treated as independent from those previously absorbed, to what is termed as the cumulative heating regime is observed. In the cumulative heating regime, the inscribed cross section is defined by the HAZ which is much larger than the focal region itself. Also, as material modification is dominated by heating effects, their isotropic nature leads to a more symmetrical modified zone. In this parameter space the focal region can be described as a point source of heat in the bulk of the sample [50]. This is a unique machining process compared with all other laser based processing and manufacturing techniques with only ULI able to provide this type of machining due to nonlinear absorption seeding the deposition of energy in the bulk.

3.2 System Hardware

To meet the requirements outlined in the previous section for a laser processing setup capable of ULI an appropriate choice of hardware was essential; with the key equipment used detailed in Table 3-1. From the components listed, the stages, stage drivers and substructure were legacy equipment that was re-tasked for the ULI setup which placed constraints on the system design and also needed to be assessed to ensure they were fit for purpose. For the remaining component selection there was consideration on building in flexibility that allows for other laser processing techniques, such as cutting and welding, to be performed without drastic modifications. The laser processing setup has also been designed to be adaptable to allow for further functionality to be added as required and some of this will be discussed in Chapter 7.

Table 3-1 *Summary of key components in each system section. All transmissive optics coated for low loss at 1030nm.Components from Thorlabs unless otherwise indicated.*

Section	Component(s)	Notes
Laser Source	Amplitude Systèmes Satsuma HP	PRF: Single shot to 2 MHz + 40 MHz Average power: 10W Pulse duration: 250 fs - >10ps Centre wavelength: 1030 nm M^2: <1.1 Pulse energy: up to 20 µJ
Power Control	Rotation mount DDR05/M Driver KBD101 Waveplate WPH05M-1030 Beamsplitter CCM1-PBS253/M	Rotation speed: 5 Hz Drive: Direct drive Waveplate order: Zero Beamsplitter extinction ratio: >1:10^3
Polarisation Control	Rotation mounts DDR05/M Drivers KBD101 Waveplate WPH05M-1030 Waveplate WPQ05M-1030	As above
Telescope	Assorted plano-concave/convex singlets Z translation mount SM1Z	Expansion ratios: 2 and 2.5
Shutter	Shutter SH1/M Driver KSC101	Max cycle rate: 12.5 Hz Min time to open: 20 ms Min time to close: 40 ms
Inscription Head	Assorted aspheric lenses Objective Turret OT1	NA: 0.16 – 0.68 Clear aperture: 5 mm
Imaging	B+W camera DCC1545M Plano-convex singlet LA1708-B-ML Z translation mount SM1Z	Frame rate: 25 fps full frame Sensitivity limit: 0.1 nW/mm^2 Pixel size: 5.2 µm
Mirrors	Dielectric UM10-45B	Reflectivity @ 1030 nm: >99 % GDD @1030 nm: <30 fs^2
Stages + Drivers	Aerotech X + Y Stages ABL15020 X + Y drivers NdriveHLe10-40 Z Stage ATS20030 Z driver Ndrive-CP10	X + Y stage precision: ±0.1 µm X + Y stage max speed: 2 m/s X + Y stage travel: 200 mm Z stage precision: ±0.3 µm Z stage max speed: 220 mm/s Z stage travel: 300 mm
Substructure	Johann Fischer Aschaffenburg Custom Granite Table	n/a
Stage Air Filtration	IMI Norgren Particle filter F72G-2GD-AL1 Oil filter F72C-2GD-AL0 Dryer W72M-2GN-NNB	Max residual particle size: 0.01 µm Max residual oil content: 0.01 mg/m^3 Dryer dew point suppression: ~25 °C

3.2.1 Laser Source

For the laser processing setup, a diode-pumped ytterbium-doped fibre laser, Satsuma HP from Amplitude Systèmes, was chosen. This source utilises single mode polarisation maintaining photonic crystal fibres as the lasing and amplifying media giving it inherent robustness and repeatability in comparison to sources based on free space cavities. The source is split into two units: a back end containing the master oscillator, acousto-optic modulator (AOM) for pulse picking, a pre-amplifier, the pump diodes and control electronics; and a front end/laser head containing the power amplifier, a second AOM, adjustable pulse compressor and a manual beam shutter.

The source configuration allows for great flexibility with the two inbuilt AOMs removing the need for a beamline AOM and allowing for custom pulse trains or selection of pulse repetition rates from single shot to 40 MHz. This permits the study of a material's response to arbitrary numbers of ultrashort pulses in both the athermal and cumulative heating regimes. Whilst the AOMs can shutter the beam they can also coarsely regulate the source output power by choice of modulation efficiency and so a single stage beamline power control suffices for fine power control. The adjustable pulse compressor tunes the output pulse durations from 250 fs to >10 ps, which gives temporal coverage over the femtosecond to few picosecond timescales highlighted in Chapter 2 as necessary for ULI without needing to be concerned with dispersion effects from beamline optics. This can be highlighted by considering the dispersion length (L_D) for a Gaussian pulse, which is the propagation distance over which the pulse duration increases by a factor of √2, when traveling through dispersive media and is given by [15]:

$$L_D = \frac{\tau_0^2}{|GVD|} \qquad 3\text{-}3$$

where τ_0 is the unchirped, i.e. minimum, pulse duration and GVD is the group velocity dispersion for the propagation media.

For 250 fs pulses and taking the value for GVD as ~19 fs^2/mm, which is for fused silica at 1030 nm, we can see that the dispersion length is ~3 m and therefore pulse dispersion is negligible. As a final note, the laser centre wavelength of 1030 nm is advantageous for working in mid-IR transmitting media as longer IR transmission often comes at the

expense of a red-shifted band edge that prohibits ULI with sources emitting nearer to visible wavelengths.

3.2.2 Beamline

The constructed laser processing setup beamline is presented schematically in Figure 3-3, with components grouped into the system sections listed in Table 3-1 by coloured boxes. The beamline was constructed using an optical cage system which ruggedizes the setup and reduces the degrees of freedom of each beamline component, both of which enhance system stability. Using an optical cage system also improves laser safety by ensuring the inscribing beam can only travel along the cage system optical path and can be readily shielded by enclosing the cage system.

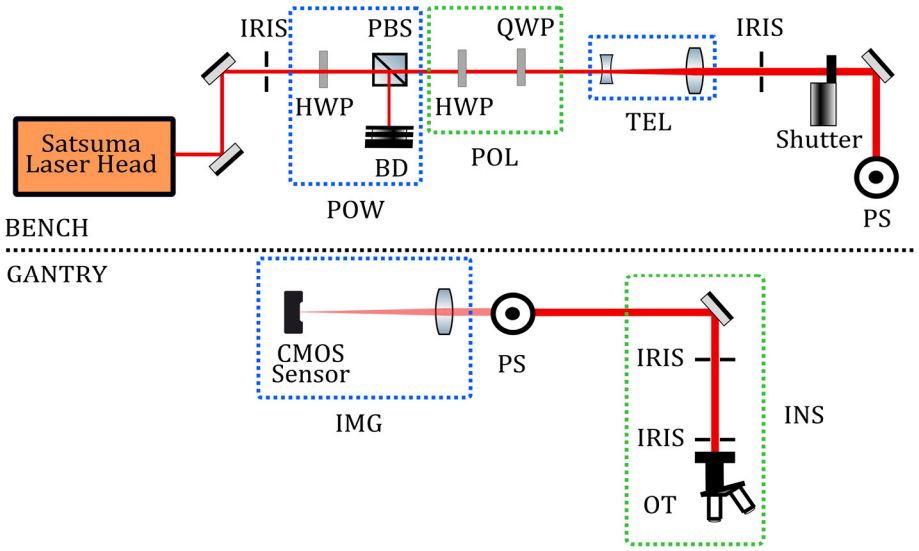

Figure 3-3 *Block diagram of the laser processing rig beamline, with components: HWP - half wave plate, PBS - polarising beam splitter, BD - beam dump, QWP - quarter wave plate, PS - periscope, OT – optics turret. Green and blue boxes group components together into the system sections listed in Table 3-1, where: POW - power control, POL – polarisation control, TEL – telescope, IMG – imaging and INS – inscription head.*

After the laser head the first two system sections in the beamline control the inscription power and polarisation state. The power control is formed by a half waveplate fixed into a computer-controlled rotation mount and cube mounted polarising beam splitter. Whereas the polarisation control is formed by a half waveplate and quarter waveplate both mounted in computer-controlled rotation mounts. These sections were both

calibrated by using modified versions of Malus's law for the case where the input light is linearly polarised and the first polariser is replaced by a half or quarter waveplate:

$$HWP: \quad I = I_0 \cos^2(2\theta) \tag{3-4}$$

$$QWP: \quad I = \frac{I_0}{2}\cos^2(2\theta) + \frac{I_0}{2} \tag{3-5}$$

where I is the transmitted intensity, I_0 is the input intensity, and θ is the angle of the waveplate axis to the axis of an analyser polariser aligned to pass the input linearly polarised beam in the absence of the waveplate.

Using equations 3-4 and 3-5, the transmitted power through an analyser polariser as a function of waveplate angle can be used to sequentially calibrate the angular position of the axis for each waveplate along the beamline. For the power waveplate the beamline polarising beam splitter acted as the analyser polariser whereas for the waveplates in the polarisation controller a Glan-Taylor polariser (Crylight, glp6-310) was used, in all instances transmitted power was measured using a Thorlabs S310C power meter. In order to perform the calibration, the laser output was limited to under 1 W by reducing the laser output AOM efficiency; the results for the power waveplate and circular polarisation waveplate are shown in Figure 3-4. In addition, for the full laser output of 10 W, the power control is able to attenuate the transmitted beam power to <1 mW for the "crossed polariser" condition. This confirms that the laser output is highly linearly polarised and requires no preconditioning before entering the controllers.

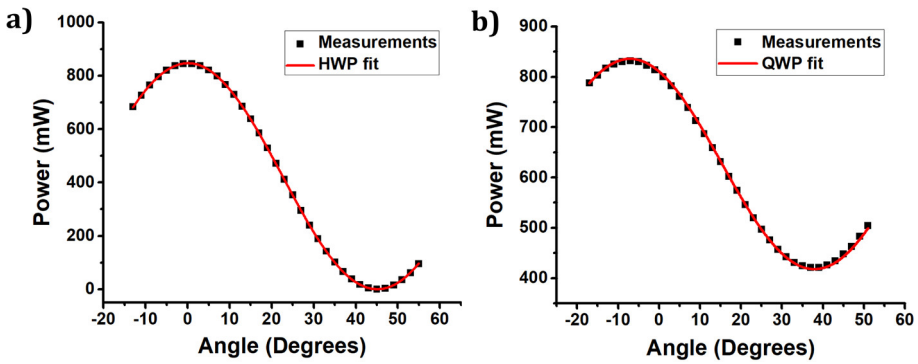

Figure 3-4 *Waveplate calibration results. a) measurements and fit for power waveplate, b) measurements and fit for circular polarisation waveplate. In both instances a good fit to the adapted versions of Malus's law was observed.*

Laser Processing Rig

Following the power and polarisation controllers is a manual telescope for beam expansion or reduction to match the beam diameter to the clear aperture of the inscription head focussing optic. The telescope consists of a fixed entrance lens and an output lens mounted in a flexure mount with micrometer adjustment allowing for easy output collimation. Setting a beam diameter that just fills the entrance pupil of the focusing optic ensures the full NA of the optic is used without clipping the beam. For the satsuma laser and the aspherics used this entails an expansion in the region of 2-2.5 which has the added benefit of lowering the power density on the beam shutter. A Galilean telescope design is used so that the inscribing beam doesn't come to a focus thus removing the risk of air breakdown. Furthermore, cylindrical lenses can be used in place of the spherical singlets listed in Table 3-1, to implement the astigmatic beam shaping techniques detailed in the previous section with the output lens flexure mount giving precise control over the astigmatic difference.

The final bench beamline component is a computer-controlled mechanical beam shutter whose primary purpose is for beam blocking during system setup and for safety interlocking as the inbuilt AOMs in the laser head offer switching with MHz cycle rates when shuttering is required for device fabrication. The beam shutter precedes a variable length periscope that links the beamline bench and gantry sections, which is mounted to the Z stage. The periscope allows for the inscribing beam to be colinear to the stage axis permitting the gantry to traverse the full range of motion of the Z stage whilst maintaining beam alignment with the entrance pupil of the inscription head optic(s).

The gantry section is user accessible and begins with a free space segment for beam characterisation or placement of slit beam shaping components. Following this is the inscription head which consists of a final beam steering mirror, alignment irises and a 4-port objective turret. The turret ports are RMS threaded allowing for easy swapping between standard microscope objectives and mounted aspheric lenses without causing misalignments. Additionally, the inscription head itself is mounted on a removable plate so that the entire section can be changed for other laser processing heads. This feature makes use of the similarities between different laser processing setups where it can be the final beam delivery components alone that enable different laser processing techniques. An example of this for the FCAP laser processing setup would be a X + Y galvanometer

mirror pair and scan lens head for large area surface patterning or cutting, as detailed in Chapter 7.

The final gantry beamline section is the imaging section which, together with the inscription optics, form an infinity optical imaging system analogous to a modern microscope. The imaging section consists of a CMOS sensor and focussing lens mounted in a flexure mount with micrometer adjustment. The focussing lens is set "at infinity" i.e. exactly one focal length away from the image plane of the CMOS sensor so that any object imaged by the inscription optics is in focus only when the object is in the focal plane of the inscription optic. With this optical setup, back reflections of the inscribing beam from the air-sample interface are imaged onto the CMOS sensor as an in-focus spot when the air-sample interface is at the inscription optic focus. This allows for simple determination of the Z position of the sample surface and finding sample edges which can be used to set an origin for inscription runs as described in Appendix A.

3.2.3 Positioning

First and foremost, sample positioning for ULI requires sub-micron levels of accuracy and precision as alluded to in the design considerations for ULI setups. This is a natural consequence of the size of the inscribing region volume given by equations 3-1 and 3-2, which for 0.4 NA focussing of 1030 nm light into fused silica is ~ 2 by 7 μm. Considering this example, it's clear to see that a positioning system which meets the requirement for sub-micron accuracy and precision enables device fabrication with diffraction limited feature size and larger structures free from stitching errors.

In order to fulfil these positioning requirements for the FCAP laser processing setup, the translation stages listed in Table 3-1, are used. The X and Y translation stages use an air bearing and direct drive motor and are therefore backlash and friction free. This gives the highest attainable translation speeds and acceleration without compromising stage accuracy and precision. The stages also offer 200 mm of travel which enables wafer scale fabrication and are supplied with compressed air at 80 psi filtered using the filter bank listed in Table 3-1.

On the other hand, the Z stage uses a ball-screw motor and linear guide bearings which provides a larger load capacity to support the weight of the gantry optics and scan heads.

Ball-screw motors are also more suited for vertical motion stages as they are fail safe, i.e. motor shutdown locks the stage whereas a non-contact direct drive motor would allow the gantry to fall and crash into the stage end of travel limit. These inherent benefits for vertical motion do however come at the expense of reduced positioning performance as can be seen from the lower maximum speed and poorer precision and accuracy of the Z stage in comparison to the X and Y stages. The Z stage translation range of 300 mm, whilst seeming longer than necessary for ULI even when considering longitudinal waveguide writing, builds in flexibility as it allows the system to accommodate a large range of processing head designs and to mount unusually thick samples.

3.3 Software

The delivery of a practical laser processing system for FCAP required the consideration of control software in tandem with the hardware selection for system design. This was to ensure that the system is easy to use and automate with the ultimate aim of allowing device fabrication to run unattended.

In terms of device fabrication, designs to be run on the system are contained in Aerobasic programs which are loaded and run as detailed in Appendix A. These files contain the stage motions required to inscribe a device and calls to change writing parameters as required for different device features or optimisation studies. As discussed in the previous sections, the machining parameter space for ULI is enormous and so automating these parameter changes allows for an efficient scan of this parameter space in a manner that would not be achievable by a system user performing a study through manually changing fabrication parameters.

The availability and quality of control software and developer libraries was a key concern for all the components chosen in the system design and manufacturer supplied software is used in conjunction with a custom control code to run the laser processing setup from a single desktop PC.

3.3.1 Original Equipment Manufacturer Software

The supplied software used to develop, troubleshoot and operate the laser processing setup consists of: motion control software for the beamline waveplate mounts and shutter, and the translation stages, Thorlabs Kinesis and Aerotech A3200 software motion controller and composer suite, respectively; Thorlabs Thorcam image acquisition software for sample imaging; and laser driver control software for the Satsuma laser.

Using the software listed, full computer control of all aspects of the laser processing setup is possible but automation of fabrication parameter changes is not as there is no means to pass information between the individual pieces of control software. In order to rectify this, custom control software, hereafter referred to as the FCAP ULI software, was written to facilitate the passing of data between the separate control software and where practical, integrate the functionality required for system use to head towards a single piece of control software for the laser processing system.

3.3.2 Custom System Control Software

National Instruments LabVIEW was chosen as the development environment in which to write the FCAP ULI software chiefly due to availability of LabVIEW developer libraries for third party application control of all the system hardware, excluding the laser where some parameters are controlled by RS-232 commands although these can also be implemented in LabVIEW using serial communication commands. LabVIEW was also chosen as the development environment as it makes it easy to create a graphical user interface (GUI), referred to as a front panel, which facilitates a clear and simple user interface for the control software. Finally, LabVIEW is intrinsically capable of both task parallelisation, enabling multiple pieces of hardware to be controlled simultaneously, and also enforcing a control sequence so that the system waits for tasks such as hardware state changes before proceeding with queued tasks.

In the design of the FCAP ULI software the priority was system automation and for this reason the software uses Kinesis LabVIEW developer libraries to fully integrate control of the waveplate mounts and beamline shutter so that inscription beam shuttering, power and polarisation can be controlled from within the FCAP ULI software. This also allows for these fabrication parameters to be changed automatically during fabrication runs by including calls to the FCAP ULI software to change these parameters in the Aerobasic

device design codes used. To include this functionality Aerotech LabVIEW developer libraries are used to enable the FCAP ULI software to send and receive data from the A3200 software motion controller. The FCAP ULI software also contains two subroutines for system setup. The first of which is a power calibration sequence to account for the variations in source output power with different settings of the Satsuma AOM modulation efficiency and the second is a slope finding sequence which determines the X and Y slope of the sample surface. The slope finder subroutine ensures structure depth is constant across large samples to avoid depth dependent modification effects and also maintains clearance between the sample and inscription optics.

The FCAP ULI software was built in LabVIEW using an event driven state machine design which is pictorially represented in Figure 3-5. This design was selected as it is suitable for programs that execute a known set of operations but with the operation frequency and order controlled by user events. State machines have another advantage in that they are modular programs which are simple to modify as new features or the automation of more fabrication parameters can be incorporated when required through adding new states. This fits with the ethos of building in adaptability into the laser processing setup as was considered in the hardware selection.

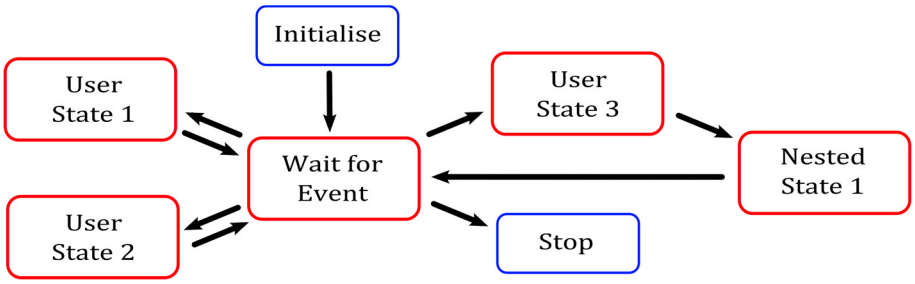

Figure 3-5 *A generalised flow diagram of the event driven state machine design used for the FCAP ULI control software. Upon program launch the initialise state runs and once complete the program proceeds to the wait for event state. The next state to execute is triggered by user input either from interactions with the FCAP ULI control software front panel or calls from running Aerobasic programs. Upon state execution the program returns to the wait for event state in all instances except for the stop state.*

In LabVIEW, a state machine is created by nesting a case structure inside a while loop, as shown in Figure 3-6. Each case, or sub-diagram, of the case structure contains the operations for one specific state and a case selector that determines which machine state

to proceed to next. The while loop is the main program loop and executes until the conditions for exiting the program are met, which is often the execution of a stop state. The while loop executes one case per iteration which ensures each state executes sequentially, removing the possibility of race conditions. Therefore, imposing these constraints provides deterministic control software that responds in a repeatable manner to user input.

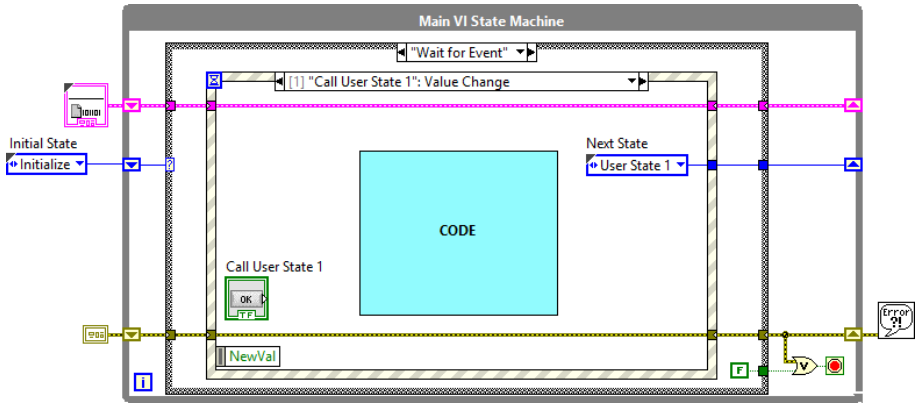

Figure 3-6 *Barebones block diagram for an event driven state machine in LabVIEW showing the wait for event state and the case selector option for when a front panel button called "Call User State 1" is pressed. The outermost structure is a while loop so that the program will run continuously until the stop state is executed. The stop state passes a Boolean true constant to the stop condition of the while loop, seen in the bottom right of the diagram to end the program. The coloured wires and associated shift registers allow data to passed between states and around the main program loop where pink, blue and yellow colour coding refers to strings, integer and error data types respectively.*

Data is passed around the main program while loop by means of shift registers which also keep track of which state to execute next as decided by the case selector code. The exact form of the case selector can vary; in the wait for event state it is an event structure that monitors front panel changes and Aerobasic program calls, whereas in the user states it is simply a constant that updates the state shift register as to which state is next. Using the event structure as a case selector in this way allows for LabVIEW to recognise requests, such as open the beamline shutter, causing a switch to the appropriate sub-diagram of the event structure that subsequently initiates a transition to the appropriate state. Event structures in LabVIEW also support event queuing so that user requests made whilst user states are executing are still captured and run once the program returns to the wait for event state.

For the FCAP ULI software, the various states in the state machine design are: initialise, which connects to the Kinesis and Aerotech hardware, and prepares the software front panel; wait for event, which captures front panel requests and polls for requests from Aerobasic programs; power, which rotates the power waveplate for power control using equation 3-4 to determine the appropriate angle; polarisation, which rotates the waveplates in the polarisation control section to set vertical, horizontal or circular polarisation states; shutter, which opens/closes the beamline shutter; power calibration, which moves the power waveplate to known positions for inscription power calibration using a power meter placed in the beamline; slope finder, which runs a sequence of stage motions to set the origin co-ordinates for the inscription run and find the sample X + Y slopes; program call, which enacts Aerobasic program requests for changes in power, polarisation or shutter state and on completion sets the next state as program return; program return, which sends a request complete signal to the A3200 motion controller; and stop, which disconnects from the system hardware and stops the program.

The final element in automating fabrication parameter changes during inscription runs comes not from the interfacial FCAP ULI control software but in establishing the commands necessary in Aerobasic inscription programs for making and waiting on fabrication parameter requests. As the FCAP ULI control software connects to the A3200 software motion controller, I/O can be achieved using Aerobasic global variables, which are accessible from any program on any task running on the controller. These can be double-precision floating-point numbers, strings or Aerobasic axis point target variables.

An example of the method selected is shown in Figure 3-7, whereby power and polarisation states are set by assigning values to global variables that can be read by the FCAP ULI control software. Signalling between the A3200 software motion controller and the FCAP ULI control software is performed by changing the value of $global[0]. Setting this variable equal to 1 triggers the program call state in the FCAP ULI software which once complete triggers the program return state which resets the variable. By implementing a while loop in the Aerobasic inscription program with a stop condition that's met when the $global[0] signalling variable is reset, the inscription run is forced to wait until requested changes have been implemented before continuing.

```
223    ;***************** SET WAVEGUIDE LASER PARAMETERS ****************
224
225          $POWER = 130 ;waveguide POWER (mW)
226
227          DWELL 0.2
228          $global[1] = $POWER ;Set power
229          $global[2] = 0 ;SET POLARISATION (0 = CIRC, 1 = VERT, 2 = HORIZ)
230          DWELL 0.5
231
232          $global[0] = 1
233          WHILE $global[0] = 1 ;Wait for requested change
234                DWELL 0.5
235          ENDWHILE
236
```

Figure 3-7 *Excerpt from an Aerobasic program demonstrating the syntax for setting the inscription power and polarisation state, signalling for the change to be made and waiting on confirmation that the change has been implemented.*

3.4 System Commissioning

The previous sections have discussed aspects of the system design including the hardware and software used to build the laser processing setup. With the system built, the final task in delivering the system was commissioning which involved fabrication of some initial demonstrator devices to confirm the systems suitability for ULI. Two strands were chosen for testing the system, one being micro-structuring of fused silica by FLICE and the other strand was waveguide writing.

For the micro-structuring testing, a feasibility study on manufacturing silica acoustic resonators for trace gas detection by laser photoacoustic spectroscopy was undertaken. Photoacoustic spectroscopy is based on sound generation caused by thermal expansion of the probed media initiated by local heating from light absorption. Using this effect, a photoacoustic spectrum of a sample can be recorded by measuring the sound generated for different wavelengths of light that is used to identify the absorbing species in the sample. The sensitivity of this technique is enhanced by using a resonator to amplify the sound generated.

The resonator design was a 10 mm long tube of 1 mm diameter with a 500 µm long 100 µm diameter tap section at the mid-point to facilitate the placing of a transducer for recording the photoacoustic spectrum. The design was inscribed in fused silica using 250 fs duration pulses with 600 nJ energy at 500 kHz repetition rate. Sample translation speed was 4 mm/s, polarisation was linear and orthogonal to translation direction with a 0.4 NA aspheric lens used for focusing. To etch away the modified regions a 5% hydrofluoric

acid (HF) solution in de-ionised water was used which was agitated using a sonic bath. The resonator at various steps in device fabrication is shown in Figure 3-8.

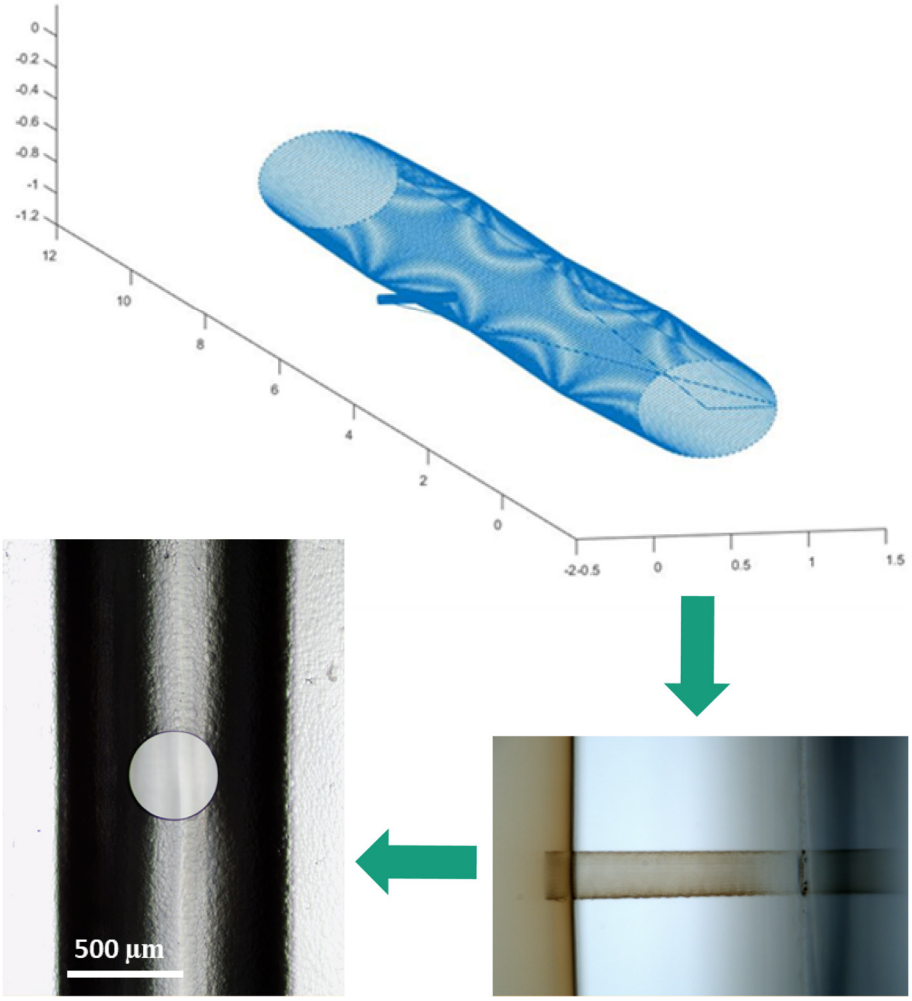

Figure 3-8 *Acoustic resonator device at different stages of fabrication. Top: Device design illustrated by simulated stage motions. Only the outer edges of the resonator tube and tap sections are inscribed to vastly reduce the processing time; because of this, these sections fall out as rods. Bottom right: zoomed in top down view of tap section as inscribed. Bottom left: side view of tap section after device etching.*

The feasibility study demonstrated that the system is capable micro-structuring glass through the FLICE technique of laser inscription followed by wet chemical etching. The structures were written correctly with no errors but unfortunately during etching the ends of the resonator tube etched up to and broke through to the sample surface. From the growth in diameter of the resonator tube and tap sections compared to their inscribed size and the maximum channel length of 5 mm, i.e. halfway point of resonator as etching from

both ends, the etching selectivity between the modified and unmodified regions was estimated to be ~1:30. Based on this result, the feasibility study concluded that it is possible to make the resonator design as etching selectivities of $1:10^2$ and $1:10^3$ have been shown for HF and potassium hydroxide (KOH) etching of fused silica, respectively, by optimising the laser inscription fabrication parameters which would be the first step of a follow up study.

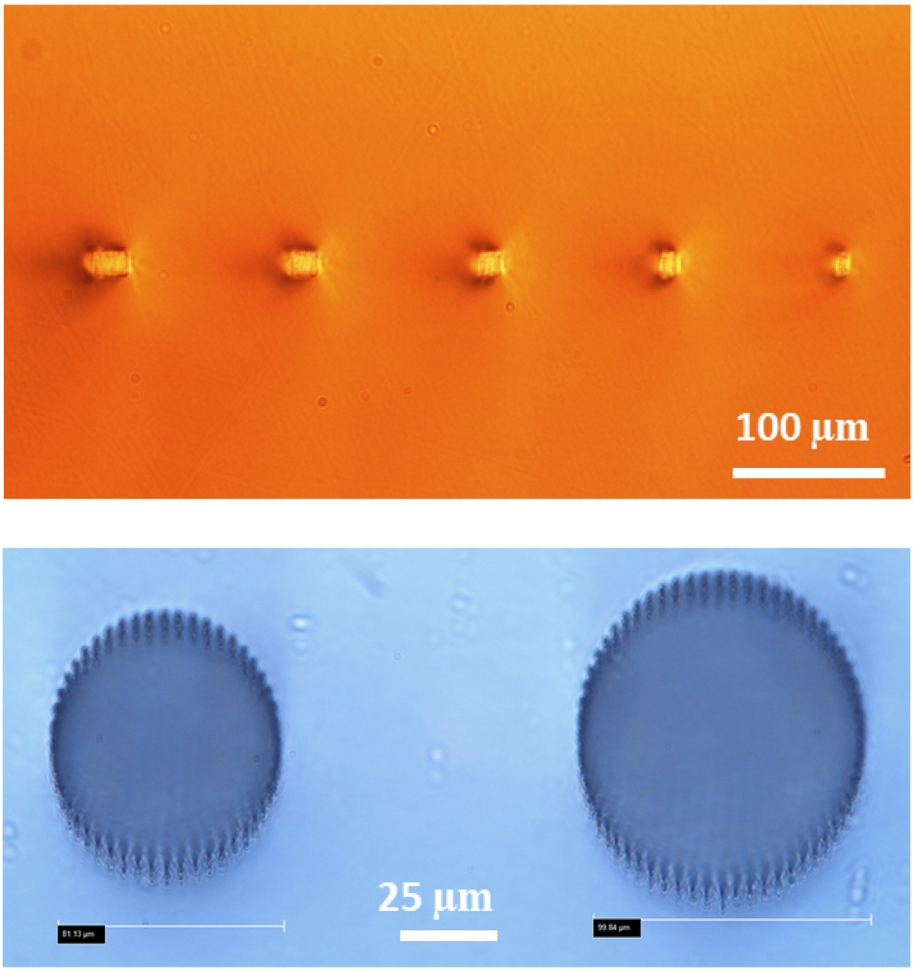

Figure 3-9 *Sample of waveguide structures written to test system performance. Top: Type I waveguide array in GLSSe with varying scan number to change core region width. Bottom: Type II cladding waveguide structures written in fused silica.*

The second strand of system testing was waveguide writing with both type I and type II waveguide designs explored, as can be seen in Figure 3-9. The results of these tests showed the system is capable of producing waveguide devices and no inscription errors were observed. In particular, a first demonstration of ULI waveguides written in gallium lanthanum sulphide selenide (GLSSe) was shown. The type I waveguides were written using the multiscan technique to control waveguide width and with a sweep in inscription

powers and translation speed, of 14 – 22 mW and 2 – 14 mm/s respectively, to control their height. The fabrication parameters held fixed were a pulse duration of 250 fs, repetition rate of 500 kHz and 0.4 NA focusing. GLSSe waveguide samples written on the FCAP system have undergone waveguide dispersion measurements and supercontinuum generation experiments with collaborators from the Fiber Sensors and Supercontinuum Group (FSaS) at the Technical University of Denmark.

3.5 Summary

This chapter has laid out the requirements for a typical ULI experimental setup with an in-depth discussion of techniques to modify the shape and cross sections of inscribed regions for microchannels and waveguides. Following this the design of a laser processing system suitable for ULI but adaptable for other laser processing techniques, which was constructed at FCAP, is presented. Details of the hardware choices made and the beamline design are then given. Following this is a discussion on the design of custom control software, which was written in the LabVIEW environment to automate the system and to consolidate some of the functionality provided by the various control software provided by the manufacturers of the system components. A final section presents the initial system outputs which were produced during system commissioning. The initial results in ULI glass micro-structuring and waveguide writing indicate the system is performing as expected.

The work on GLSSe waveguide writing undertaken for system commissioning and the results of testing the GLSSe waveguides at the Technical University of Denmark are forming the basis of a manuscript currently under preparation for publication in Optical Materials Express [112].

Chapter 4 Germanium Arsenic Selenide Waveguides for Mid-IR Integrated Optics

This Chapter discusses the fabrication of ULI waveguides in novel chalcogenide glasses for mid-IR optical applications. The Chapter begins with an overview of chalcogenide glass waveguides designed to operate in the mid-IR with a focus on ULI fabricated devices and highlighting the applications for which they are suited. This is followed by details on the first demonstration of inscription of ULI channel waveguides in $Ge_{22}As_{20}Se_{58}$ glass (GASIR-1, Umicore N.V.) as well as how a suitable fabrication parameter range was identified. The waveguides were subsequently assessed for losses, guiding characteristics and their dispersive properties through mode field diameter and waveguide loss measurements at 2.94 μm along with waveguide dispersion measurements in the 1 – 4.5 μm range. The dispersion measurements were undertaken to estimate the zero dispersion wavelength for the waveguides. Z-scan measurements of bulk samples have also been performed to determine the nonlinear refractive index of GASIR-1. Finally, the utility of GASIR-1 ULI waveguides for chip scale broadband sources is shown by demonstrating the broadest and deepest mid-IR supercontinuum to-date from a ULI waveguide. The generated supercontinuum spanned approximately 4 μm from 2.5 to 6.5 μm when pumping with femtosecond pulses.

4.1 Mid-IR Chalcogenide Glass Waveguides

Chalcogenide glasses have been widely employed in demonstrations of channel waveguides and have been fabricated by both ULI techniques and thin-film methods [73, 113]. Numerous studies have focussed on innovative methods of device fabrication, or on near-IR applications utilising the high nonlinearities of chalcogenides for applications such as All Optical Switching (AOS) [114, 115], but there have been fewer reports of channel waveguide devices for the mid-IR. Nonetheless, there are some notable instances of ULI fabricated waveguides that focus on mid-IR applications which will be discussed in this section.

One such example is the use of ULI in GeAsS glasses to create single mode (SM) large mode field diameter (MFD) mid-IR guiding structures. This was achieved by a waveguide design consisting of a hexagonal array of positive index waveguide cores spaced with a pitch in the region of 5 μm which allows evanescent coupling between the individual

waveguides. Together the cores form an evanescently coupled multicore waveguide array [116] that showed SM guiding at 3.39 μm with an MFD of 37 μm and propagation losses of 1 $dBcm^{-1}$. This waveguide demonstrates the potential for power scaling SM type I ULI waveguides using large MFD guiding which would benefit high power mid-IR applications such as compact amplifiers.

In another example, Type I waveguides in GLS glass have been shown to be suitable for astrophotonics such as mid-IR beam combiners for stellar interferometry. In this work ULI inscribed evanescent couplers in GLS exhibited power splitting ratios of between 8% and 99% based on coupler interaction length for mid-IR light at 3.39 μm with a beat length of 5.75 mm [117]. Other sulphide based chalcogenide glasses have also been used for this purpose with GeS_2-Ga_2S_3-CsI-Sb_2S_3-SnS glass (GCIS) three beam combiners demonstrating a monochromatic interference visibility of 99.89% at 10.6 μm and an ultrahigh bandwidth (3–11 μm) interference visibility of 21.3%. SM guiding across the entire 3-11 μm range was demonstrated by controlling core size with beam combining performed using Y couplers [118].

Single scan waveguides of 14.3 mm length in GLS were used for the first demonstration of mid-IR supercontinuum generation in ULI fabricated waveguides [119]. Seed pulses for broadening were produced by an OPA pumped by a regeneratively amplified Ti:sapphire laser system, which output pulses at 1 kHz, 800 nm centre wavelength and 100 fs pulse duration. The OPA signal and idler outputs and DFG between the signal and idler gave access a 1.1 – 4 μm range. For pump pulses centred at 2.49 μm with 130 nJ pulse energy, an output spectrum spanning 2 – 2.9 μm was measured between the -15 dB points. In the case of pulses with centre frequency of 3.85 μm and 115 nJ pulse energy, an output spectrum spanning 2.9 – 4.5 μm was observed between the -15 dB points.

The study drew comparisons between the bulk nonlinear refractive index and nonlinear refractive index inside the modified regions and showed a factor of 5 decrease which is detrimental to supercontinuum production. The bulk nonlinear refractive index was determined by Z-scan measurements using a 1 mm thick sample whereas the nonlinear refractive index of the modified region was estimated from the number of SPM peaks evident in the broadened output spectrum for the waveguide. It is possible to attribute some or all of the nonlinear refractive index decrease as an artefact of temporal

broadening of the pump pulses in the waveguide reducing the pulse peak intensity but it is still an area of concern.

Subsequent work has shown supercontinuum from ULI fabricated GLS waveguides, of 9 mm length, with output spectra covering the entirety of the first mid-IR atmospheric transmission window, as seen in Figure 4-1. In this instance the waveguide cross section was controlled by the multiscan technique to produce step-index waveguides which guided a more circular mode than previous demonstrations. The supercontinuum produced spanned 1.75 – 5 µm for 120 fs duration 410 nJ energy pump pulses centred at 4.26 µm, with the upper limit due to detector responsivity drop-off rather than spectrum cut off. Due to SPM broadening effects and by pumping at 4.26 µm, which is on resonance with a CO_2 absorption feature, the input pulse energy is distributed away from one of the main sources of loss in the 2 – 5 µm transmission window which benefits the Signal to Noise Ratio (SNR) for applications such as remote sensing.

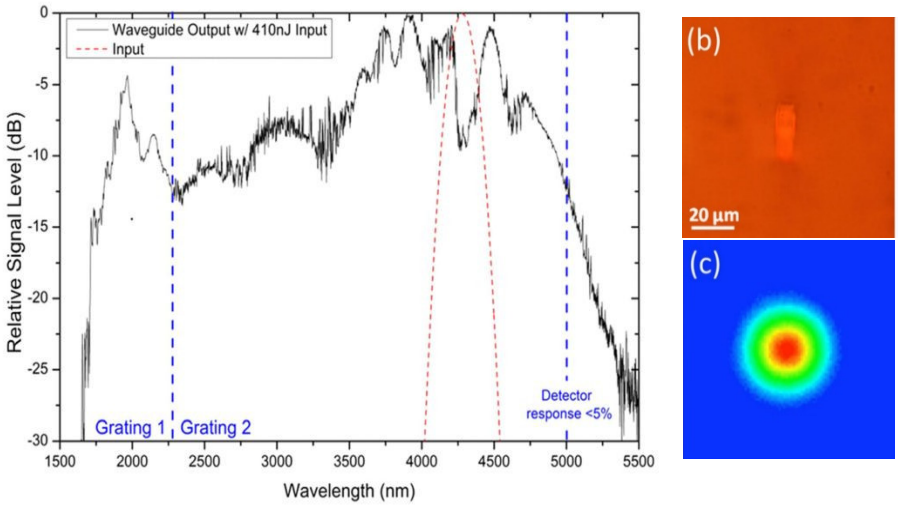

Figure 4-1 *Left: Supercontinuum spectrum generated with a 410 nJ incident pulse energy. The location and width of the input pulse spectrum is indicated by the broken red line. The pulse is centred at 4.26 µm near to an atmospheric CO_2 absorption peak. Right: The GLS waveguide end facet and scale bar is shown in (b) and the corresponding mode image of the below threshold pump at 4.26 µm is shown in (c) with the same scale [39].*

From the examples given, it is apparent that the current work in ULI fabricated devices using chalcogenide glasses for the mid-IR has been predominately in sulphur based chalcogenides. For devices to access wavelengths deeper into the IR or for taking

advantage of stronger material nonlinearities, selenide based chalcogenides need to be employed, as highlighted in Chapter 2.

With regards to selenide based chalcogenides, there have been several recent theoretical and experimental demonstrations of thin film channel waveguides in Ge-As-Se glasses for Mid-IR supercontinuum generation. Karim *et al.* [120] presented a numerical study of air clad $Ge_{11.5}As_{24}Se_{64.5}$ ridge waveguides on MgF_2 reporting a supercontinuum spanning from 1.8 to 7.7 μm when pumping with a peak power of 500 W at a wavelength of 3.1 μm. Subsequently, in a further theoretical study, Karim *et al.* [121] show a 1.8 to 8 μm supercontinuum could be output from $Ge_{11.5}As_{24}Se_{64.5}$ rib waveguides on MgF_2 using 85 fs pulses centered at 3.1 μm with a peak power of 500 W. Yu *et al.* [122] have reported an experimental demonstration of a 1.8 to >7.5 μm supercontinuum from a $Ge_{11.5}As_{24}Se_{64.5}$ glass rib waveguide on a $Ge_{11.5}As_{24}S_{64.5}$ substrate by pumping the waveguide with ~320 fs pulses at 4 μm and a peak power of ~3 kW. In their work the long wavelength edge of the supercontinuum was limited by absorption in the protective fluoropolymer coating applied to the waveguides. Yu *et al.* [123] have also presented experimental results showing a linearly polarised supercontinuum spanning 2 to 10 μm produced by pumping a buried rib waveguide, consisting of a $Ge_{11.5}As_{24}Se_{64.5}$ core and a $Ge_{11.5}As_{24}S_{64.5}$ cladding, with 330 fs pulses centered at 4184 nm and 4.5 kW peak power. These theoretical studies and experimental demonstrations have all employed waveguides fabricated using Two Dimensional (2D) planar techniques which allow for high index contrast and therefore tight confinement, which is advantageous for many integrated optics applications in the Mid-IR [124]. These techniques do however have disadvantages, as discussed in Chapter 1, such as process complexity and limited scope for vertical stacking of components.

As a member of the Ge-A_S-Se glass family, GASIR-1 was selected as a sensible host material for ULI waveguides to demonstrate the potential of ULI waveguide supercontinuum sources for the mid-IR. GASIR-1 is a commercially available material (Umicore N.V.) with high optical quality and transmission range from 1 - 15 μm, which makes it an ideal candidate for mid-IR integrated optics applications. As well as demonstrating the broadest and deepest ULI waveguide supercontinuum to-date, the study of waveguide writing in GASIR-1 can be readily translated into other applications in the mid-IR such as beam combining and on-chip sensing due to the flexibility in device design offered by ULI.

4.2 GASIR-1 Waveguide Fabrication and Characterisation

A study of the response of GASIR-1 to ULI processing methods was undertaken using the Nonlinear Optics Group (NLO group) laser processing setup located at Heriot-Watt University [125]. The system consists of a mode-locked Yb-doped fiber laser source (IMRA μ-Jewel D400) that emits 360 fs pulses with a central wavelength of 1045 nm and a pulse repetition rate of 500 kHz. The laser pulse train was passed through power and polarisation control optics to set the inscribing pulse energy and circular polarisation. Finally, the pulse train was focused using a 0.4 NA aspheric lens to give a focal spot diameter of approximately 1.8 μm.

GASIR-1 samples were mounted on air bearing stages (Aerotech ABL1000) and passed through the focus of the aspheric lens using the transverse writing geometry to write lines of modified material across a range of inscribing beam pulse energies, to study the effect the parameter sweep has on the material modification. Modification lines were written at a depth of ~250 μm below the sample surface to avoid surface ablation during writing and with consideration of the working distance of the objective and the sample thickness. After each inscription run the sample was removed and the end facets imaged using a microscope with transmission illumination to characterise the inscribed regions. This allows for both the determination of the cross section of the modified tracks and a rough assessment of the type of refractive index change induced by checking for light guiding. An end facet image showing the results of one such pulse energy parameter sweep is shown in Figure 4-2.

From the pulse energy sweep studies, it was found that for these writing conditions only Type I index change could be produced. At the higher pulse energies larger Type I regions extending up towards the sample surface were produced, i.e. in the pre-focal section of the focused beam. These investigations also showed for incident pulse energies of 12 nJ the modified region was approximately rectangular with height, extent in the z direction as defined in Figure 4-2, equal to the confocal parameter of the focused beam in the samples, calculated using equation 3-1.

For GASIR-1 which has a refractive index of ~2.54 at the inscribing wavelength and given the M^2 value for the inscription laser of 1.2, this gives a modification region height of ~13 μm for 12 nJ pulses. Careful control of the inscribing pulse energy in a few nJ range

around 12 nJ allowed for adjusting the height of the modification lines from approximately 10 to 15 µm whilst maintaining the rectangular cross section.

With the ULI parameters established for controllable Type I modification, waveguides were fabricated using the multi-scan writing technique at a depth of ~250 µm from the sample surface. The multi-scan technique was used so that waveguide width, extent in the x direction as defined in Figure 4-2, could be controlled in a deterministic manner that is decoupled from changes in the waveguide height. This allowed for the fabrication of arrays of waveguides with different core sizes. A waveguide array was fabricated containing 7 waveguides with core widths ranging from 2 to 8 µm and core heights of 15 µm (which are referred to as WG1-7 in order of ascending core width and shown in Figure 4-2) Waveguide core dimensions were chosen based on mid-IR ULI waveguides produced in other chalcogenide glasses [110]. Once inscribed, the waveguide end facets were ground back and re-polished to remove any defects caused by clipping of the writing beam at the sample edges, creating waveguides of 8 mm in length.

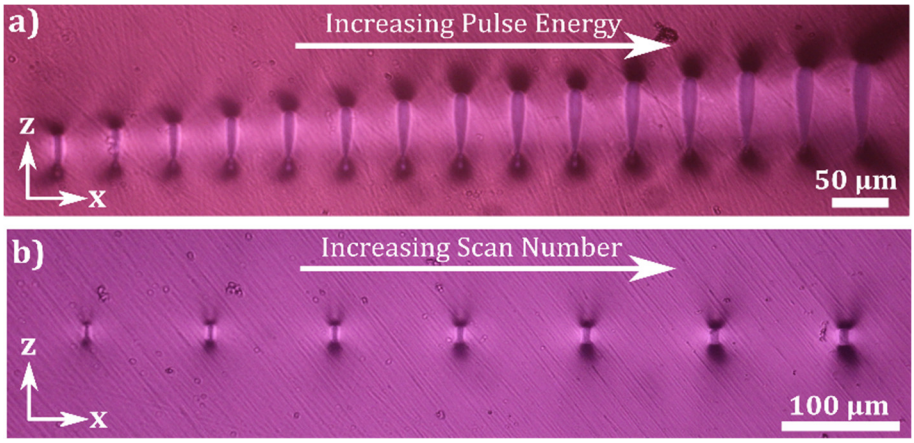

Figure 4-2 *Transmission microscope images showing the resulting material modification from two fabrication parameter sweeps. a) single line scan results for increasing pulse energies from 34 to 90 nJ. b) The array of multi-scan waveguides used in this work. Written with identical laser parameters but increasing scan number to vary the waveguide core width. In both cases the inscription beam is incident from above.*

Waveguide losses and MFD measurements were performed for each waveguide in the array by fixing the inscribed sample in a waveguide alignment workstation. An overview of the experimental setup is given in Figure 4-3 along with the waveguide losses and $1/e^2$ MFD values for each waveguide. Light was coupled into and collected from the

individual waveguides using a pair of 0.25 NA ZnSe objectives (Innovation photonics, antireflection coated for 2 - 12 μm). The collection objective was used to image the output facet directly onto the sensor of a mid-IR InSb camera (FLIR SC7000) or power meter for mode imaging and loss measurements, respectively. Input power measurements into the waveguides were taken by moving the power meter in front of the first objective, labeled L1 in Figure 4-3. The signal laser used was a Er:YAG mid-IR laser emitting up to 1 W at 2.94 μm (Sheaumann 2.94 μm MirPac). All the stated waveguide losses account for Fresnel reflections at both the input and output facets and so consist of the contribution from coupling and propagation losses. The $1/e^2$ MFD values were calculated using a Gaussian fit to the mode image formed on the InSb sensor with a scale factor determined by taking images of calibration targets mounted in place of the inscribed sample.

It was found that WG1, which has the smallest core, offered poor confinement at the signal laser wavelength and so losses and MFDs could only be accurately determined for WG2 to WG7 which correspond to core widths of 3 to 8 μm. In this range, the waveguide MFDs were observed to decrease from an average value of 16.25 μm ± 0.5 μm to an average value of ~13 μm ± 0.5 μm. For WG2 the guided mode was slightly elliptical with the weak lateral confinement resulting in a larger MFD in the x direction, for the remaining waveguides the guided modes were observed to be circular to within the error in the measurement technique. WG2 to WG5 were observed to be single mode at 2.94 μm whereas first order modes could be excited in WG6 and WG7 with the input spot misaligned. The lowest loss measured was 1.4 dB ± 0.21 dB for WG5 which has a cross section of 6 by 15 μm and accounts for Fresnel loss. By making the conservative assumption that the lowest measured loss represents perfect coupling into WG5, i.e. no coupling losses from mode field mismatch, we can provide an upper estimate for the propagation loss of the waveguides of 1.75 $dBcm^{-1}$ ± 0.26 dB cm^{-1}. The manufacturer provided attenuation coefficient for GASIR-1 at 3 μm is less than 0.01 cm^{-1} and so the origin of the propagation loss can be seen to be from the waveguide.

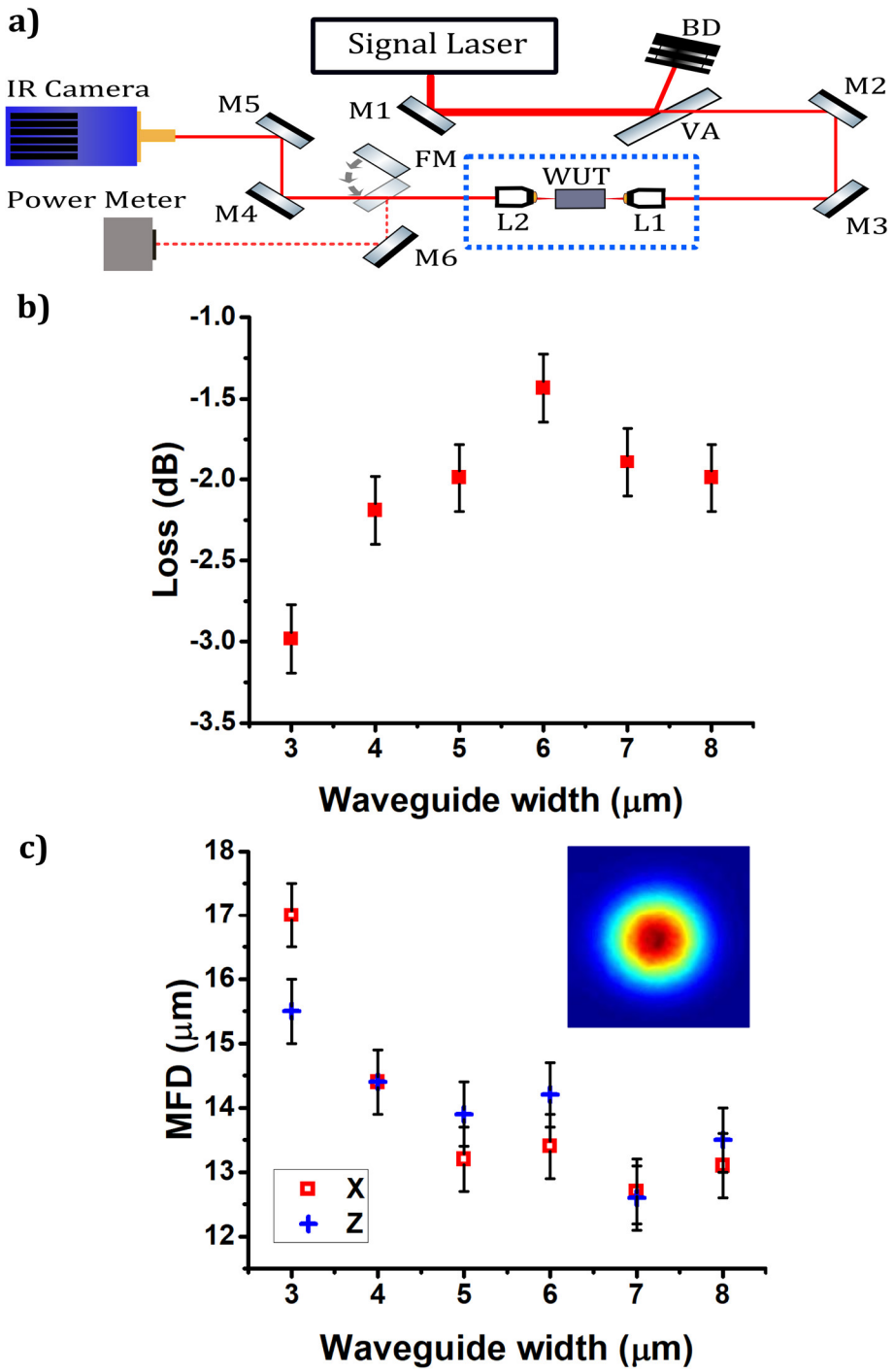

Figure 4-3 *Experimental setup for initial waveguide testing, waveguide losses and guided mode dimensions. a) Setup where: Mx, silver mirrors; VA, reflective variable ND filter; BD, beam dump; L1 and L2, BBAR-coated ZnSe objectives; WUT, waveguide under test; FM, flip mirror. Blue dotted box signifies components mounted on waveguide alignment workstation. b) Waveguide losses including coupling and propagation loss for WG2-7. c) Waveguide $1/e^2$ MFD measurements for x and z directions for WG2-7 with an insert showing the near field mode image of WG5.*

4.3 The Z-scan Technique

In Chapter 2, the concept of a nonlinear refractive index, i.e. an intensity dependent refractive index, was introduced. This was related to pulse broadening through SPM and to soliton propagation by the balance of the linear chirp that SPM induces with chirping caused by chromatic dispersion. SPM and solitons are both examples of temporal effects from a refractive index that is modified by the time varying field intensity of a travelling pulse, but if we consider that a laser beam has a finite dimension in space and that there is a spatially varying field intensity across the beam, we could imagine that the nonlinear refractive index would manifest itself in spatial effects as well. This does indeed occur and leads to self-focussing or self-defocusing of intense laser beams in dielectric media as the nonlinear refractive index causes a spatially varying phase delay across the beam in a similar manner to the way in which a lens reshapes/deforms the wavefronts of a laser beam. This can be utilised in applications such as ultrafast pulse generation by Kerr Lens Mode-locking (KLM) [126].

These spatial effects are also employed by the closed aperture Z-scan technique, devised by Sheik-Bahae *et al.* [127], in order to determine the sign and magnitude of the nonlinear refractive index for transparent dielectric materials. The technique measures the deviation of a laser beam passing through a thin sample as a function of intensity and uses this result to determine the nonlinear refractive index. This is accomplished by a simple experimental setup, shown in Figure 4-4, in comparison with other methods developed for nonlinear index measurement such as nonlinear interferometry and four wave mixing experiments [128, 129].

Furthermore, removing the aperture makes the Z-scan setup insensitive to phase variations so that the sample's absorption as a function of intensity can also be determined. This is known as an open aperture Z-scan, which through tuning the wavelength of the laser source used, can independently determine the sample's absorption coefficient for each nonlinear absorption order [130]. Open aperture Z-scans are also used to study the saturation for different multiphoton absorption orders [131].

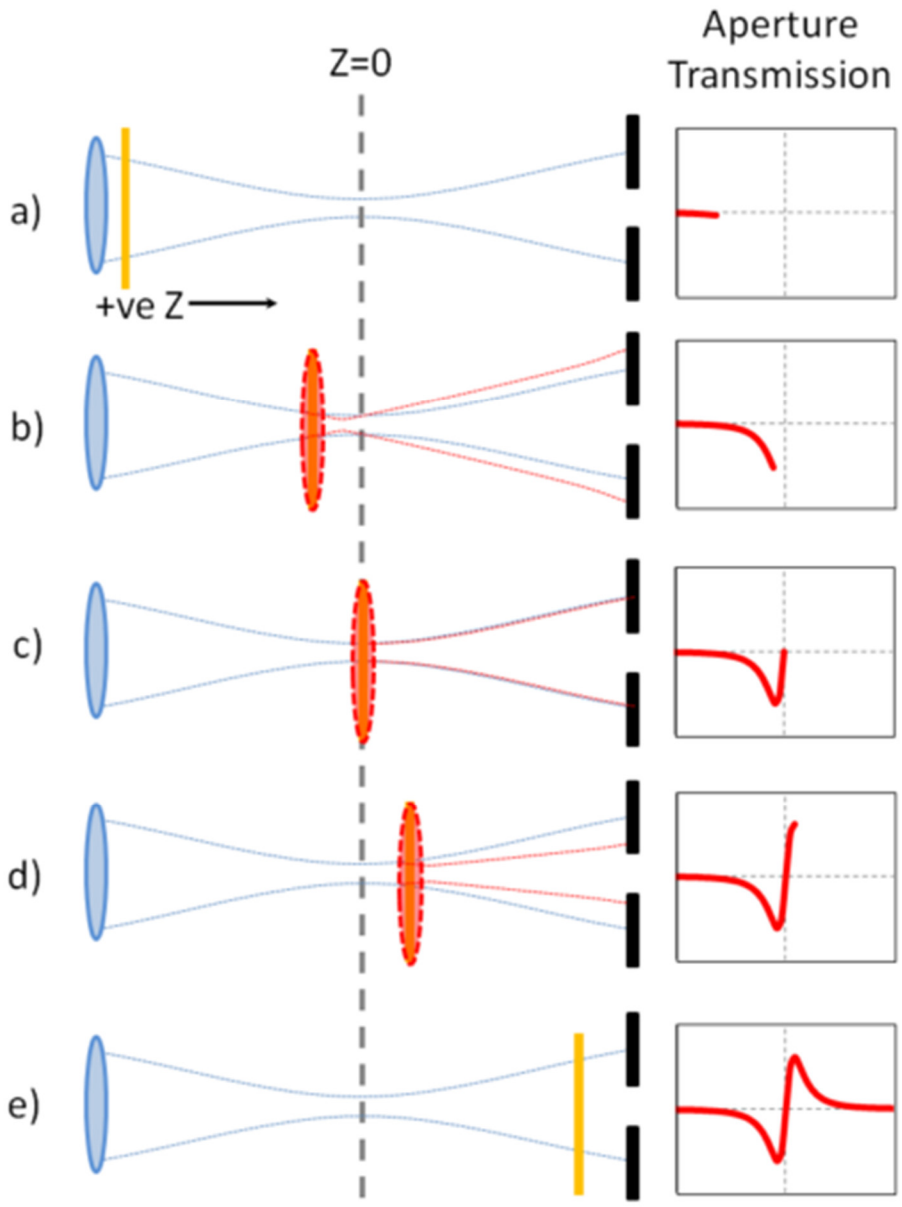

Figure 4-4 *Pictorial representation of an open Z-scan measurement for a material exhibiting a positive nonlinear refractive index, adapted from [132]. a) upstream and far from the focal region; b) upstream near the focal region; c) at the focus; d) downstream near the focal region; and e) downstream and far from the focal region. Near the focus the sample acts as a positive lens leading to a decrease in aperture transmission when the sample is upstream and near the focus, and an increase in aperture transmission when the sample is downstream and near the focus.*

Z-scans involve translating a thin sample along the optic axis, i.e. the Z direction, of a loosely focused beam and the recording the normalised transmittance of the beam as a function of sample position. For closed aperture scans, the transmittance of the beam through the aperture is influenced by the sample position as follows: upstream and far

from the focal region the light intensity is too low to affect a response from the sample under test; with translation along Z toward the focal region the increasing intensity of light in the sample induces a deviation of the beam, due to self-focussing or self-defocussing through the materials nonlinear refractive response, and therefore a change in aperture transmission; when the sample is at the focus there is a null point in beam deviation akin to placing a thin lens at the focus; moving past the focus, beam deviation from self-focusing or self-defocussing occurs again and affects the aperture transmission; finally, when the sample the far downstream of the focus the beam intensity is once again too low to induce a sample response.

For a sample with a positive nonlinear index, as shown in Figure 4-4, closed aperture Z-scans show a characteristic minimum then maximum in aperture transmission, known as a valley-peak trace, whereas a negative nonlinear response results in an opposite peak-valley aperture transmission. Therefore, the shape of a closed aperture Z-scan trace gives an immediate indication of the sign of a materials nonlinearity. The determination of the magnitude of the response, however, requires a method of fitting the recorded data. For open aperture scans the beam transmittance is affected solely by sample absorption near the focal region which, in the absence of any absorption saturation, leads to a minima in sample transmission when the sample is at the focus and a 'sharpness' defined by the order of the absorption process which can be determined by fitting for various absorption orders.

Determining exact values for the magnitude of the nonlinear refractive index and nonlinear absorption coefficients by fitting to a Z-scan trace requires semi-analytical or numerical solving for the propagation of a laser beam through the sample under test [133, 134]. But for the case of Gaussian beams, small phase changes, $\Delta\phi_0 << 1$, and thin samples, $L < z_r$, the following approximate formulas hold:

$$T_{cl}(z) = 1 + \frac{4x\Delta\phi_0(1-S)^{0.25}}{(1+x^2)(9+x^2)} \qquad 4\text{-}1$$

$$T_{op}(z) = 1 - \frac{\beta I_0 L}{2\sqrt{2}(1+x^2)} \qquad 4\text{-}2$$

where $T_{cl}(z)$ is the normalised closed aperture transmission and $T_{op}(z)$ is the normalised open aperture transmission, both as a function of sample position with respect to the focal plane of the Z-scan setup; x is the relative sample position given by $x = z/z_r$; z_r is the Rayleigh range of the focused beam given by equation 3-1; $\Delta\phi_0$ is the on-axis time averaged phase change for spatially and temporally Gaussian pulses given by $\Delta\phi_0 = 2\pi L n_2 I_0/(\lambda\sqrt{2})$, with L the sample length, n_2 the nonlinear refractive index, I_0 the on-axis peak intensity of the laser pulses and λ is the test wavelength; and β is the two photon absorption coefficient.

4.4 Mid-IR Z-scans of GASIR-1

Measurements of the nonlinear refractive index of GASIR-1 were performed by means of the closed aperture Z-scan technique introduced in the previous section. The experimental setup, as seen in Figure 4-5, utilises 120 fs pulses output from a OPA (Spectra Physics OPA-800) pumped by a regeneratively amplified mode-locked Ti:Sapphire laser operating at 1 kHz. The OPA output can be tuned from 1.1 to 1.6 μm for the signal and from 1.6 to 2.9 μm for the idler and therefore the idler output of the OPA can be used to investigate the nonlinear refractive index values of GASIR-1 into the mid-IR. Long pass filters (Schott RG850) are used to remove the copropagating residual pump light and white light supercontinuum seed which is generated to initiate the amplification of signal and idler wavelengths in the OPA.

To ensure a Gaussian spatial profile, as required by equation 4-1, the output of the OPA was first focused through a 100 μm diameter diamond pinhole held in vacuum to remove any higher order spatial modes and was recollimated before entering the Z-scan section of the setup. A pick-off beam splitter is placed in the collimated section of the beam path upstream of the sample to divert approximately 8% of the beam onto a reference photodetector (New Focus 2033 or Thorlabs PDA30G-EC for 1.55 μm or 2 and 2. 5 μm measurements, respectively) which was used to compensate for laser power fluctuations. A flip mirror is used to direct the beam onto a pyroelectric detector (Laser Probe, RKP-575) connected to a power ratiometer (Laser Probe, RK-5720) to record the power incident on the test samples. An upstream reflective neutral density (ND) filter is used to modulate the incident laser power and hence the on-axis intensity at the focus. The OPA output was finally focused for the Z-scan section using an uncoated 20 cm focal length

Calcium Fluoride (CaF_2) lens giving beam waists of 26, 28 and 32 µm for the 1.55, 2 and 2.5 µm beams, respectively.

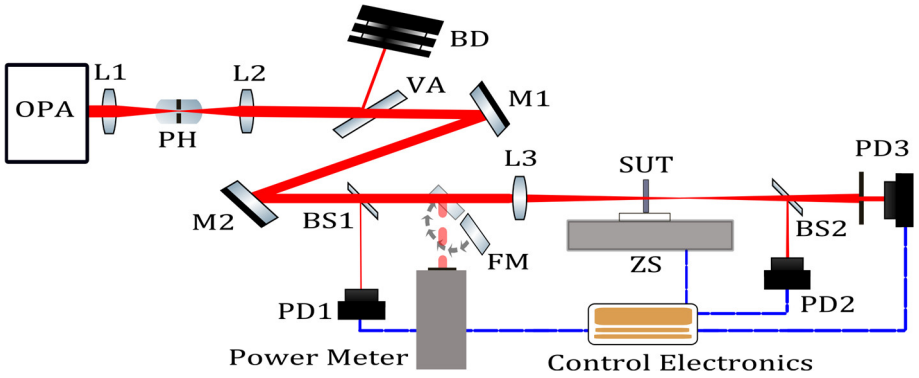

Figure 4-5 *Experimental setup for Z-scan measurements where: L1 and L2, achromatic doublet lens; PH, pinhole; VA, reflective variable ND filter; BD, beam dump; Mx, silver mirror; BSx, beam splitter; PDx, photodetector; FM, flip mirror; L3, CaF_2 lens, SUT, sample under test; and ZS, Z-stage. Control electronics includes the Z-stage motion controller, custom peak-hold unit for photodetector output, function generator and control PC with DAC.*

A 1 mm thick GASIR-1 sample was mounted to a motorised translation stage (Newport UTM 150 series), driven by a motion controller (Newport MM005), to translate the sample through the focus along the beam path. The far-field transmittance through an adjustable aperture is recorded using a second identical photodetector, termed the closed-aperture detector. The aperture was set to transmit 50% of the input beam without a sample in the beam path. A second pick-off beam splitter is used to divert 8% of the transmitted beam onto a third identical detector, termed the open-aperture detector, for simultaneous open-aperture Z-scan measurements. This setup allowed for the recording of Z-scan traces at tunable Infrared wavelengths, as shown in Figure 4-6. Measurements taken at 1.55, 2 and 2.5 µm as extending nonlinear index measurements further into the mid-IR was limited by the stable tuning range of the OPA and sensitivity range of the photodetectors.

Data acquisition is automated using a PC running custom control software written in HP VEE. This control software drives the translation stage and records the output from the three photodetectors in the experimental setup as a function of sample position along the Z-scan section of the beamline. To facilitate data acquisition, the transient output of the photodetectors is first passed through a peak-hold unit, triggered using a function

generator, to create a signal that can be digitized using a data acquisition card (DAC) installed in the control PC. To increase the accuracy of the measured Z-scans the control software allows for measurement averaging and windowing as selectable by the user.

Closed aperture Z-scans traces of GASIR-1 were fitted using the empirical normalised Z-scan transmittance formula, equation 4-1, to determine the sign and magnitude of the nonlinear refractive index with an error of ± 15% due to the approximations assumed for the empirical fit. The occurrence of MPA was monitored using normalised plots of transmitted power recorded by the open aperture detector, in order to ensure MPA was not affecting the measurements. The onset of MPA was observed to occur for pulse energies around 10 nJ at 1.55 and 2 μm and around 130 nJ at 2.5 μm. This is consistent with a change in MPA order from two to three photon absorption given the center wavelengths of the pulses. A UV-Vis transmission spectrometer (Lambda 950) was used to investigate this which showed that although the band edge of GASIR-1, defined by the absorption coefficient exceeding 10^4 m^{-1}, is in the region of 664 nm there is a long absorption tail with some residual linear absorption out beyond 1 μm.

A positive nonlinearity was observed as is evident from the shape of the Z-scan trace which indicates a nonlinear focusing of the beam by the sample. The magnitude of the nonlinear refractive index was seen to monotonically decrease for increasing wavelengths, as is shown in Figure 4-6. The measured nonlinear refractive index values were validated by comparing the value measured at 1.55 μm to published literature. The value measured in these experiments of 5.5×10^{-18} m^2/W ± 15% is in close agreement with the same glass composition in a recent large-scale Z-scan study of various chalcogenide glasses at 1.55 μm which was reported as 5.62×10^{-18} m^2/W [135].

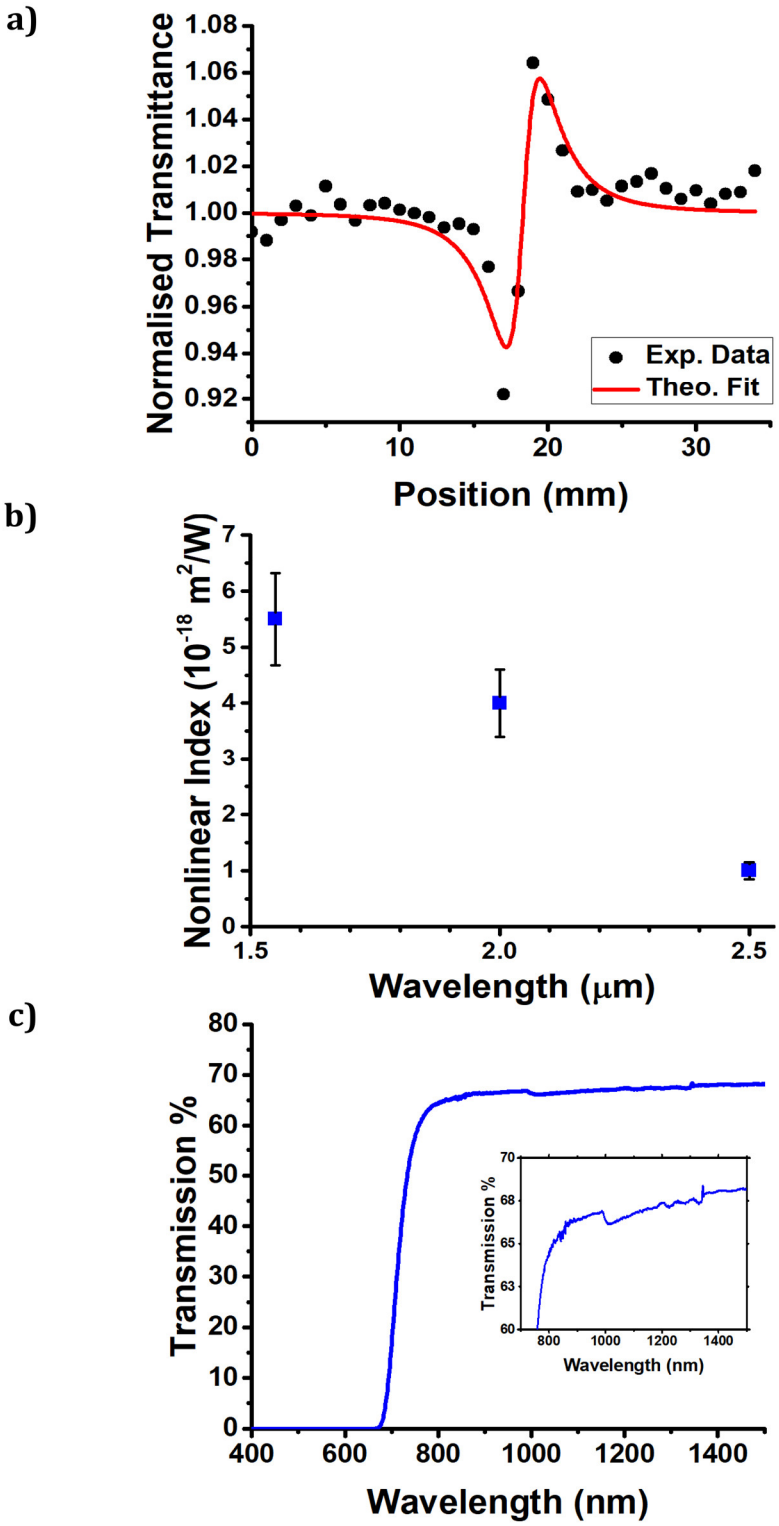

Figure 4-6 *Z-scan measurement results. a) Representative Z-scan trace taken using 10 nJ pulses centered at 2 μm with a linear aperture transmittance of 50% and fit using the closed aperture Z-scan formula. b) Plot of measured n_2 values vs wavelength including errors (± 15%). c) Transmission spectra showing band edge with a zoomed in view insert showing the absorption tail, includes Fresnel losses.*

4.5 Waveguide Dispersion

The dispersion of the waveguides was determined by collaborators in the FSaS group at the Technical University of Denmark. The dispersion measurements are performed using white-light interferometry with a mid-IR supercontinuum source (NKT Photonics), a balanced Mach-Zehnder interferometer, and a scanning spectrometer (Spectro 320, Instrument Systems). A detailed description of the method is found in [136, 137]. Figure 4-7 shows the measured dispersion for four different waveguides.

For each waveguide four measurements were performed at different optical path delays yielding different interference patterns that resulted in slight variations in the fitted dispersion curve. For this reason, the dispersion curves in Figure 4-7 represent the mean over these four measurements, with error bars indicating the variation in the fits. Because of the limited sampling the fits vary significantly near the edges of the spectrum, and especially at the short-wavelength edge where the dispersion slope is very steep. The inset zoomed in view on the long-wavelength edge of the measurement shows the variation at the long-wavelength edge more clearly together with an estimated ZDW around 4.44 μm and 4.56 μm for WG1 and WG3, respectively.

The measured dispersion was found to be almost the same for each waveguide despite the large geometric difference, which indicates that the dispersion is dominated by material dispersion and that the refractive index contrast is low. The measured dispersion of the larger WG5 and WG7 was limited on the long-wavelength side by the source and on the low-wavelength side below 1.7 μm side by interference from higher-order modes.

The presence of higher-order modes is also visualised in Figure 4-7 through windowed Fourier transform spectrograms. The spectrograms translate the interference patterns into a delay curve, which result in a delay curve for each significant mode. The spectrograms show that WG1 exhibits only a single dominant mode, whereas two distinct traces are seen for WG5 below 1.7 μm. Moreover, the higher-order mode appears to dominate over the fundamental mode at shorter wavelengths making it difficult to measure the dispersion in this region.

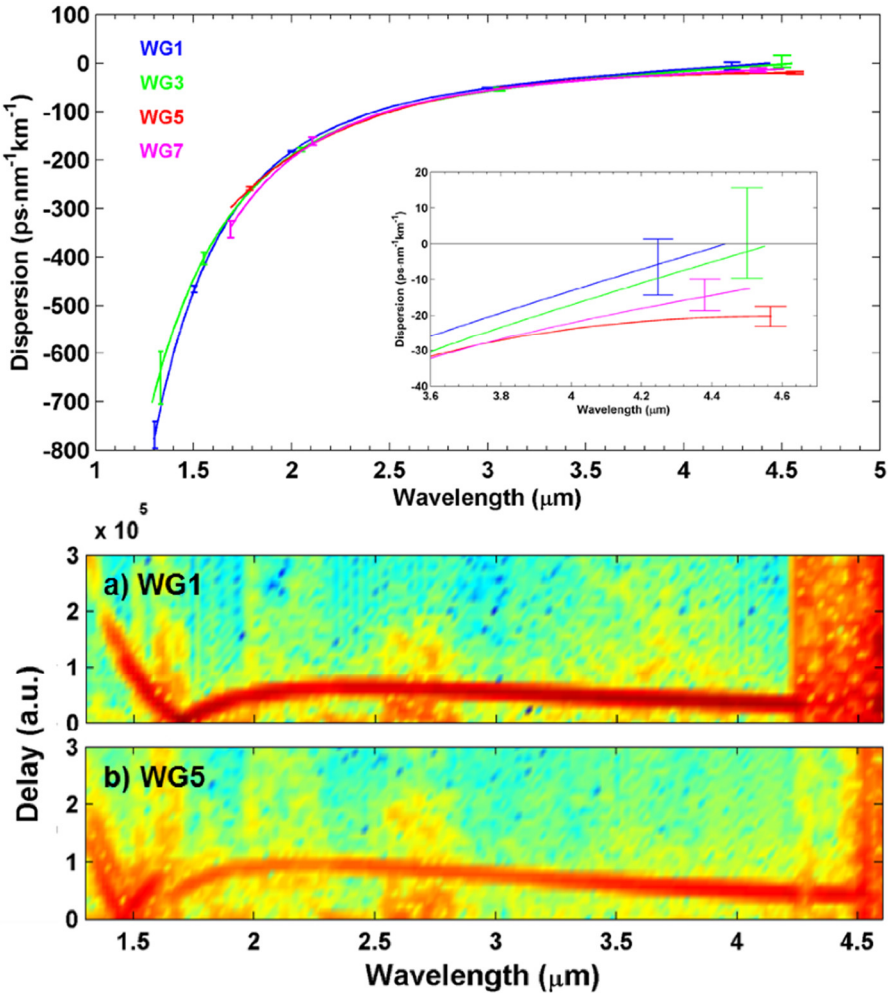

Figure 4-7 *Dispersion results and analysis. Top: Measured dispersion of different waveguides. The lines represent the mean of four measurements with error bars indicating measurement uncertainty. The insert shows a zoomed in view on the long-wavelength edge of the measurement, indicating a ZDW around 4.44 μm and 4.56 μm for WG1 and WG3, respectively. Bottom: Windowed Fourier transform analysis of interference spectra from a) WG1 and b) WG5, which demonstrates that WG5 exhibits multimode beating below 1.7 μm. In this particular example the higher-order mode is dominating at short wavelengths making it difficult to measure the dispersion in this region.*

4.6 Waveguide Supercontinuum Generation

For supercontinuum generation, the waveguides were pumped by mid-IR femtosecond pulses produced through DFG using a silver thiogallate ($AgGaS_2$) nonlinear crystal. The DFG crystal is synchronously pumped by the signal and idler outputs of the aforementioned OPA used for Z-scan measurements. Residual signal and idler power was blocked by a long pass 2.5 μm filter. The difference frequency output was passed through a tunable magnesium fluoride (MgF_2) half-wave plate and a barium fluoride (BaF_2) wire

grid polariser for power and polarisation control. A flip mirror was used to divert the beam onto a pyroelectric detector (Laser Probe, RKP-575) connected to a power ratiometer (Laser Probe, RK-5720) for incident power measurements.

Light was coupled into and collected from the individual waveguides using a pair of 0.25 NA ZnSe objectives (Innovation photonics, antireflection coated for 2 - 12 μm) or 20 mm focal length uncoated CaF_2 lenses (Thorlabs LA5315). The waveguide output was alternately imaged directly onto the sensor of a mid-IR InSb camera (FLIR SC7000) for alignment and to record the guided mode profiles or through a monochromator (Zolix Omni-λ300) to measure the output spectrum. The monochromator was used with a cryogenically cooled mercury cadmium telluride (MCT) detector (Zolix DMCT12) and a lock-in amplifier (Princeton Applied Research 5209) to measure the spectral power distribution of the supercontinuum. A 3.6 μm long pass filter was used to remove any higher order diffraction effects caused by the gratings in the monochromator. The experimental setup used and results are shown in Figure 4-8.

Supercontinuum width was observed to increase with increasing waveguide core size. This is explained by better coupling of the input light through improved mode matching and a decreasing waveguide MFD which enhances nonlinear interactions. Furthermore, for the smaller waveguides longer wavelengths, as was the case for WG1 at 2.94 μm, are not well confined. The pump pulse wavelength was chosen to be centered at 4.6 μm as this is above the ZDW for the smaller waveguides and is also within the range of the InSb camera used for waveguide alignment. The largest waveguide, WG7, produced a supercontinuum spanning approximately 4 μm from 2.5 to 6.5 μm when pumped with 130 nJ pulses, corresponding to a peak power of ~1000 kW, coupled and collected using the CaF_2 lens set. This represents the broadest and deepest IR supercontinuum from a ULI waveguide to date. Pumping with higher energy pulses did not improve the result which is attributed to the onset of MPA depleting the pulse. This is supported by the visible surface damage to the waveguide end facet that occurred when increasing the pulse energy further to around 300 nJ. The dispersion characterisation of the larger waveguides revealed that they exhibit normal dispersion at 4.6 μm and therefore supercontinuum generation occurred for a pump centered below the ZDW.

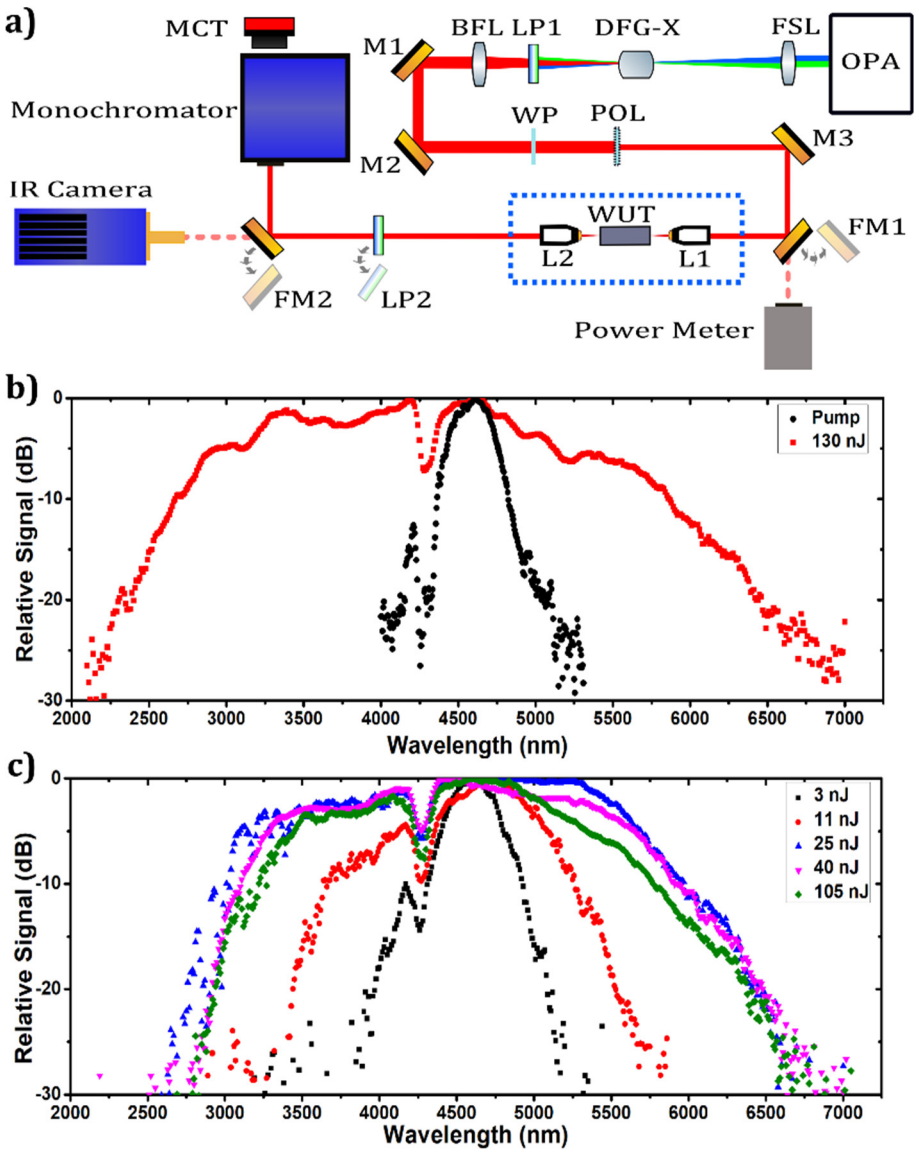

Figure 4-8 *Supercontinuum measurement setup and results. a) Setup where: Mx, gold mirrors; FSL, fused silica lens; DFG-X, DFG crystal; BFL, BF2 lens; LPx, long pass filters; WP, waveplate; POL, wire grid polariser; FMx, flip mirrors; L1 and L2, BBAR-coated ZnSe objectives or uncoated CaF2 lens; WUT, waveguide under test; MCT, MCT detector. Blue dotted box signifies components mounted on waveguide alignment workstation. b) Broadest supercontinuum measured spanning ~ 4 m at -20 dB points. Produced by pumping WG7 with 130 nJ pulses coupled and collected with CaF2 lens set. Input pulse spectrum is also shown. c) Evolution of supercontinuum with input pump power for WG5 with ZnSe objective set. Broadening is seen from pulse energies as low as 3 nJ.*

By measuring the pump spot size and waveguide MFDs for below threshold energy pulses at 4.6 μm it was identified that the ZnSe objectives provided the best mode matching and therefore lowest coupling loss into WG5. This allowed for an investigation of the threshold energy for the onset of spectral broadening in WG5 which was found to be at

around 3 nJ of incident pulse energy, corresponding to a peak power of ~24 kW. Broader supercontinuum generation is predicted for pump pulses centered deeper into the mid-IR beyond the ZDW but the drop off in sensitivity of the InSb camera used for waveguide alignment in this work restricted the testing of above ZDW pumping for the larger waveguides.

4.7 Summary

This chapter has presented work on the first demonstration of ULI fabricated waveguides in GASIR-1, a commercially available glass with high optical quality that transmits light up to ~15 μm, which were subsequently used to produce mid-IR supercontinuum. This represents the first step in introducing GASIR-1 as a new material for ULI fabricated mid-IR integrated optics and for nonlinear optics applications.

The Chapter began with an overview of chalcogenide glass waveguides designed to operate in the mid-IR with a focus on previous ULI fabricated devices and highlighting the applications for which they are suited. Following this, the results of a study on the response of GASIR-1 to ULI fabrication techniques were discussed. For the parameter space investigated, the response of GASIR-1 was found to be an increased refractive index in the inscribed regions and so Type I multiscan waveguides were fabricated.

The guiding properties of the multiscan waveguides in terms of number modes supported, MFD and losses have also been presented along with nonlinear optical characterisation in the mid-IR using the Z-scan technique. Finally, mid-IR supercontinuum generation has been shown when pumping GASIR-1 ULI waveguides with femtosecond pulses centered at 4.6 μm. When pumping the largest waveguide, WG7, with 130 nJ pulses a supercontinuum spanning approximately 4 μm from 2.5 to 6.5 μm was measured. This represents the broadest and the deepest IR supercontinuum from a ULI waveguide to date. Dispersion characterisation found the ZDW for WG7 to be above 4.6 μm and hence the supercontinuum was produced by pumping in the normal dispersion regime. This alludes to the possibility of even wider supercontinuum by pumping larger core GASIR-1 ULI waveguides in the anomalous dispersion regime.

The work from this chapter was published in Optical Materials Express [138] and presented at CLEO 2016 [139] and CLEO 2018 [140].

Chapter 5 Micro-structuring of Gallium Lanthanum Sulphide for Mid-IR Optofluidics

This Chapter presents the first demonstration, to the best of our knowledge, of selective chemical etching of bulk Chalcogenide glasses using the FLICE technique detailed in Chapter 2. GLS was chosen as the substrate material for this study due to its favourable material properties which include: a wide transmission bandwidth, covering parts of the visible spectral region out into the mid-IR; low toxicity, for bio-compatibility; large nonlinear response, for the prospect of on-chip frequency generation, and because of its wide use in ULI fabricated devices utilising waveguide circuits, examples of which can be found in Section 4.1.

The Chapter begins with a discussion on micro and optofluidics along with devices fabricated by ULI with a focus on those using silicate glasses as the substrate material. The proceeding section gives an overview on the work which has been undertaken in wet chemical etching of Chalcogenide glasses which helped to inform the etchant selection for this study. The next section details the etching of ULI fabricated micro-channels in GLS using various concentrations of inorganic and organic wet chemical etchants in solution. These trials were performed in order to quantify the selectivity of material removal between modified regions and the bulk glass. To qualify the experimental method the GLS trial results were compared with FLICE processing of fused silica micro-channels inscribed using the same inscription setup.

Following this is a discussion on the optofluidic sensor design with justifications for the design decisions made. A final section describes the progress towards fabrication of a demonstrator optofluidic sensor in GLS to illustrate the potential of the tested techniques for robust mid-IR optofluidic sensors. Results in GLS are also compared to the same optofluidic sensor design fabricated in fused silica.

5.1 Micro and Optofluidics

Microfluidics is defined as the science and technology of processing or manipulating fluids with volumes at or below the micro-litre scale [141]. Optofluidics, on the other hand, can be considered as an extension of microfluidics by the integration of optical

technologies, for sensing, actuation or imaging, within microfluidic systems [142]. Both micro- and opto-fluidics are cross-disciplinary fields that have parallels with the integrated optics concept introduced in Chapter 1, and with micro-electronics, inasmuch as they all seek to miniaturise larger systems for reductions in Size, Weight and Power (SWaP) and cost whilst increasing device functionality.

With microfluidic devices, the benefits for sample analysis, sorting and sensing applications include: reductions in the sample and reagent volumes, for both cost saving and fast detection times; scalability for screening applications and sample processing, by high throughput and/or parallel processing; and automation of complex *in vitro* assay procedures through using Lab-on-a-Chip (LoC) devices in which an entire sensing or sample analysis procedure is performed on a chip [143].

Whilst many different fluidic functions can be implemented with LoC devices, the monitoring and/or detection of microfluidic samples is challenging due to the reduction in detection volumes associated with working at the micro-scale [144]. Fortunately, optical measurement techniques offer high sensitivity as well as flexibility in detection scheme, as demonstrated by imaging flow cytometry LoC devices offering throughputs of around 4800 cells per second [145]. Also, in addition to detection, light can be used to add extra functionality to LoC devices by steering or trapping of cells, nanoparticles and molecules [146].

LoC devices have been widely demonstrated and are now a powerful tool for research in areas such as the life sciences, but they have also been referred to as a misnomer as they are often chips in labs rather than LoC [147]. This is because the benchtop equipment commonly used in conjunction with LoCs for monitoring and sample detection, such as confocal microscopes, are large and complex and therefore require both the space and specialist operators that a research laboratory can provide. The combination of a microfluidic LoC device with benchtop equipment, like bulk optical setups, negates some of the potential benefits afforded by the microfluidic chip itself, namely device portability and the associated possibility for *in situ* applications. Optofluidics is therefore a clear route towards the fabrication of true LoC devices that would be suitable for *in situ* testing by integrating the benchtop optical setups required to operate the device.

In micro and optofluidics, the individual fluidic components that form the micro-fluidic portion of a device are linked with micro-channels. This is analogous to the role that waveguides fulfil on an integrated optics chip linking photonic components. Micro-channels with cross-sections typically on the order of 10 to 100's μm are required for this purpose, which have been fabricated by methods such as: photo lithography, soft lithography, laser machining, and ULI through the FLICE technique [148, 149]. With respect to other fabrication methods, ULI has the advantage of offering true 3D design freedom allowing for complex micro-channel and microfluidic components to be fabricated [150]. The design flexibility that ULI offers can enable unique fluidic components, for example laminar 3D hydrodynamic flow focusing which will be discussed in the following section.

ULI can also readily fabricate waveguides in a wide range of dielectric materials, as demonstrated in Chapters 4 and 6, and detailed in Chapter 2. ULI can therefore be used to incorporate waveguides and photonic components into microfluidic chips to create integrated opto-fluidic devices and hence enable applications such as the on-chip optical sensing of liquid samples [151]. In materials where both FLICE and waveguide inscription has been demonstrated, ULI can be used to fabricate the integrated optical components concurrently with the pre-etch micro-channel structures in a single processing step. This ensures the alignment of waveguides and micro-channels in the optofluidic device and their relative position can be precisely controlled.

5.1.1 ULI fabricated Optofluidics

FLICE has been successfully used to structure both crystalline and glassy materials, as detailed in Chapter 2, which enables the ULI fabrication of microfluidic components across a range of materials. However, demonstrations of ULI fabricated optofluidic devices have been largely limited to silicate glasses, specifically fused silica or the photosensitive aluminosilicate glass Foturan (Schott A.G.) [63].

One example of such a ULI fabricated optofluidic device is the chip-scale cell counter [152], shown in Figure 5-1. The device takes advantage of the 3D design freedom offered by ULI to perform full 3D hydrodynamic focusing with a single sample and sheath flow inlet. As can be seen in Figure 5-1, the sheath flow channel splits into four separate channels with equal cross-section that subsequently recombine around the sample flow

channel confining the sample flow to the centre of the detection region. The constriction provided by the sheath flow serves two uses: firstly, its restricts cells in the sample fluid to flow to one element at a time across the detection region ensuring a simple binary cell counting signal is output from the device; and secondly, it allows for alignment of integrated waveguides with the sample flow in large channels where there is no risk of channel blockage. The addition of optical waveguides for input and output of the optical signal used for cell counting resulted in a monolithic optofluidic cell counter providing counting rates up to 5000 cells per second in a device with a volume less than 1 mm^3.

With regards to sensing applications, another example of ULI fabricated optofluidics comes from the demonstration of on-chip refractive index measurements of dilute acetic acid referenced to refractive index matching oils of known value [153]. For this work, the optofluidic chip consisted of microfluidic reservoirs which were evanescently probed by integrated Bragg grating waveguides with sensing sections matched axially to the microfluidic reservoirs at waveguide to reservoir separations around 1 μm. Several designs for waveguide routing and reservoir design were trialled with the highest refractive index sensitivity, of 81 nm/riu, provided by a dual reservoir design on either side of a 10 mm long waveguide sensing section. Reference gratings were also incorporated into the Bragg grating waveguide circuits to compensate for temperature and strain variations.

The examples given show that ULI fabrication techniques are well suited to optofluidic device fabrication in silicate glasses. Unfortunately for mid-IR applications, the long wavelength cut-off of silicate glasses, in the region of 2.5 - 3.5 μm, makes these materials unsuitable for mid-IR optofluidics. In order to overcome this restriction, selective etching and waveguide writing must both be demonstrated in a mid-IR transmitting substrate, and to this end GLS glass was selected for the etching studies described in this Chapter. The justification for the pursuit of mid-IR optofluidics in GLS is described in the next section.

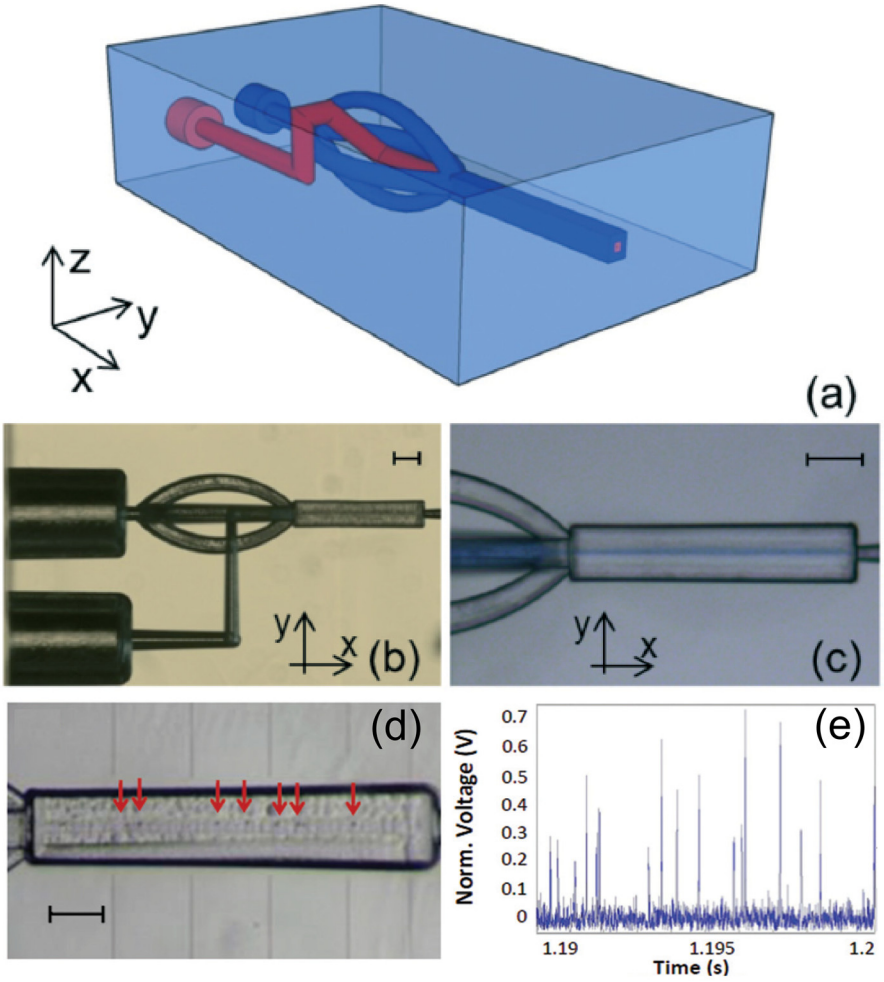

Figure 5-1 *LoC cell counter using 3D hydrodynamic focusing and optical detection. (a) Schematic rendering of microfluidic circuit. (b) Microscope image of the fabricated microfluidic circuit. (c) Zoomed in view demonstrating flow confinement of a dyed sample fluid in the horizontal and vertical directions. (d) Confined stream of red blood cells in opto-fluidic device with input and output waveguides visible. (e) Signal output from cell counter where peaks indicate passage of individual cells. Scale bars are 100 µm. Adapted from [152].*

5.1.2 Gallium Lanthanum Sulphide as a Substrate for Mid-IR Optofluidic Devices

GLS was chosen as the material in which to investigate mid-IR optofluidics due to the enabling nature of GLS for novel optofluidic devices, specifically in comparison with silicate glasses GLS offers: a wider transmission bandwidth, from around 0.55 µm to 8 µm and a exhibits a nonlinear response that is around 100 times larger [78].

The combination of visible and mid-IR transmission offers the prospect of extending the wavelength range of optical detection techniques in ULI fabricated silicate glass

optofluidics with negligible effect on the existing methods employed, for example adding the possibility of mid-IR spectroscopic sample characterisation using external mid-IR sources. The large nonlinear refractive index of GLS also provides a route to bring the sources required for mid-IR spectroscopy on-chip by integrating mid-IR supercontinuum optimised waveguides demonstrated in GLS, such as those discussed in Chapter 4, into optofluidic devices. One additional route to integrating mid-IR sources into GLS optofluidic devices is through the doping of rare-earth or transition-metal ions into GLS. Thus far, demonstrations of lasers utilising GLS based gain media have been limited to the near-IR, with 1 μm emission from neodymium doped GLS thin-film waveguides and fibres [72, 154]. But recent results reporting on fluorescence emission centred at 2.75 μm from ULI waveguides in erbium doped GLS gives the prospect of mid-IR lasers with GLS gain media to come [155].

As well as the benefits that GLS offers for mid-IR optofluidic devices versus fused silica, the chemical composition and thermo-mechanical properties of GLS makes it more suited for optofluidic chips than many other chalcogenide glasses. For example, in contrast with many other chalcogenide glasses, such as those listed in Table 2-1, GLS is non-toxic through its lack of arsenic content, which would make GLS optofluidic devices bio-compatible for applications in the life sciences. Compared with other well-known commercially available chalcogenides glasses, such as AsS, AsSe and GeAsSe, GLS exhibits a working temperature ~200-300 °C higher, a lower coefficient of thermal expansion, has a 2-4 times higher thermal conductivity, 3-4 times higher stiffness and is up to twice as hard [156, 157]. These thermo-mechanical properties would make GLS mid-IR optofluidics more robust and thermally stable than counterparts fabricated in other chalcogenide glasses.

Finally, as optofluidic devices require both microfluidic and photonic circuitry, GLS was selected for its demonstrated history of ULI fabricated mid-IR channel waveguides, such as those discussed in Chapter 4. As well as specific mid-IR waveguide examples, studies on ULI waveguide writing in GLS using slit beam shaping, the multiscan technique and cumulative heating highlight the flexibility of GLS for ULI waveguide fabrication [158]. This leaves a single avenue of investigation, namely GLS micro-structing through FLICE, to unlock the potential of GLS for ULI fabricated mid-IR optofluidics.

5.2 Chalcogenide Glass Wet Chemical Etching

FLICE processing of GLS requires the selective etching of laser modified regions by a suitable wet chemical etchant. To the authors knowledge there have been no previous reports on the selective etching of bulk chalcogenide glasses but there has been research into the selective etching of chalcogenide thin films with many studies focusing on planar applications for example masks for lithography [80] or diffractive optical elements [159].

In these applications 2D surface patterning is sufficient and so etching selectivity has been attained using methods such as CW or pulsed near bandgap laser irradiation, or etching under patterned illumination to induce the structural changes in the films that would lead to selective etching [159-166]. For these studies, the predominant materials used have been thin films of the AsS and AsSe glass families modified in their as-deposited state to ensure large structural differences between exposed and un-exposed regions; typically irradiation results in photopolymerisation which makes exposed area more resistant chemical etching and therefore the films act as negative photoresists [73]. The etching chemicals used have been basic inorganic etchants such as KOH or sodium hydroxide solutions, or basic organic etchants, mainly amines in solution [80]. Notably most of these studies have reported modest selectivity values across a wide range of etchants, with the ratio of etch rates between modified and un-modified regions typically less than ~10.

With regards to 3D patterning of chalcogenide films, there have been two noteworthy reports in thermally evaporated AsS thin films which were used in the production of a 3D photonic crystals [167], as seen in Figure 5-2, which was followed by a study of high selectivity AsS film etchants [168]. In both demonstrations microstructures were created by irradiation of the as-deposited film using the output from an amplified Ti:sapphire system (PRF 1 kHz, 800 nm centre wavelength, 120 fs pulse duration) with pulse energy attenuated to the few nanoJoule range, focussed into the sample using an oil immersion objective (1.4 NA).

The etchant in the photonic crystal demonstration was diisopentylamine in dimethylsulfoxide (DMSO) solvent, which was used to develop a woodpile photonic crystal with an omnidirectional 3.5% photonic bandgap using single writing and etching step in under two hours. Whilst no value for etching selectivity was reported, from the dimensions of the etched woodpile structure, a conservative selectivity ratio of ~35 can

be estimated. The origin of the high etching selectivity was attributed to the size of the amine molecule which contains two sterically bulky organic groups attached to the nitrogen atom inhibiting dissolution of photopolymerised areas, deemed to be a crosslinked As_2S_3 glassy network, while maintaining the rate of dissolution of the surrounding film which contains smaller As_4S_6 molecules.

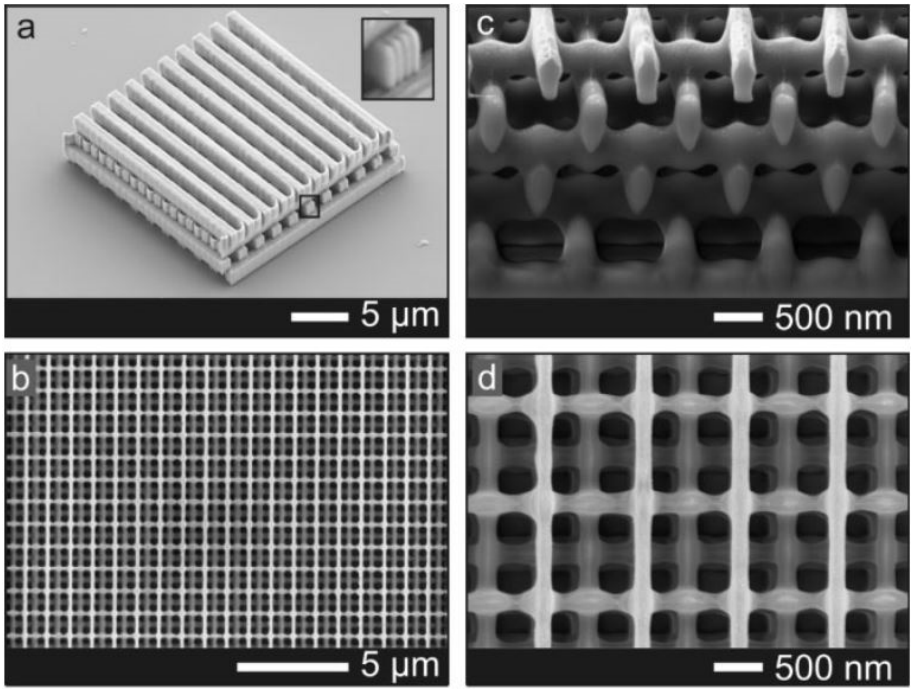

Figure 5-2 *Scanning electron microscopy images of As_2S_3 woodpiles. a) Woodpile with rod separation distance a = 2 µm. Inset - Each rod is made from eight parallel subrods to yield a rod height-width aspect ratio of almost unity. b) Top view of a woodpile with rod separation distance a = 1 µm. c) Focused ion beam cross section of the woodpile in (b). d) Close up of (b). Adapted from [167].*

For the high selectivity etchant study, a series of sixteen aryl amines synthesised from dibenzylamine were manufactured to study the effects of electron-withdrawing, electron-donating, bridging methylene removal, and steric size increase on the etching rates of irradiated and non-irradiated regions in AsS films. This resulted in a reported etching selectivity of 344:1 for the synthesised complex amine molecule N-(1-pyrenyl)-(4-methoxybenzyl)amine in solution with DMSO. This high selectivity was achieved through careful etchant design to create a molecule which simultaneously forms a passivation layer on the surface of irradiated regions whilst attacking the surrounding as-deposited film.

The reports on selective etching of chalcogenides in this section whilst performed on chalcogenide films, form a valid starting point for FLICE processing of bulk GLS glass. The wide range of selectivities shown also highlights the importance of the etchant search and etchant optimisation once a class of suitable etching chemicals has been identified.

5.3 Gallium Lanthanum Sulphide Selective Etching Trials

A selective etchant search for GLS was performed by trialling a range of the basic organic and inorganic chemicals used for the chalcogenide thin film etching discussed in the previous section along with some common etchants, including HF which has been used extensively for FLICE structuring of silicate glasses.

In order to determine the bulk dissolution rate of GLS and the dissolution rate of ULI modified regions in the various etchants, as required for determining etchant selectivity, a series of pre-etch channel modification regions were inscribed in bulk GLS samples for etching tests. The modification regions were inscribed using the NLO group laser processing setup discussed in Chapter 4 at a depth of 250 μm beneath the sample surface using 1 ps pulses at a pulse repetition rate of 500 kHz. The transverse writing geometry was used for fabrication with circular polarisation and a 0.4 NA aspheric lens for focussing the inscribing beam. A series of translation speeds and inscribing powers were trialled, namely 1, 2, 4, 8, 16 mm/s and 25, 30, 35, 40 mW, with the channels grouped in blocks with constant power as shown in Figure 5-3.

Multiscan channels consisting of 10 distinct line elements were written with a line element pitch of 0.33 μm to simulate the effect of rastering out larger areas as would be required for creating microfluidic circuits in real devices. The channels themselves were written with a 100 μm pitch in GLS samples with dimensions of 30 by 10 by 1 mm. Sample dimensions were chosen so that the channel set could been inscribed twice across the sample, with the sample subsequently diced into 10 5 by 5 mm sub-samples. The dicing step serves two purposes; firstly, it allows to creation of 10 identical sub-samples from the master sample to ensure the samples used in the etching trials were identical; secondly, the dicing removes any effects of edge clipping which occur as the inscribing beam leaves the master sample. Using smaller samples without dicing would require individual sample grinding and re-polishing introducing sample to sample variation.

Etchant trials were undertaken using the amines morpholine and diisopentylamine in solution with DMSO which have both been shown to selectively etch sulphur based chalcogenide thin films [161, 167]. The inorganic basic etchant KOH was also selected and used in aqueous solutions [160]. To test the response of bulk and ULI modified GLS to acidic and oxidising agents, HF, hydrochloric acid (HCL) and nitric acid aqueous solutions were also employed. All solutions were prepared to give 1 vol% solute to 99 vol% solvent. HF, HCL, KOH and nitric acid are supplied in aqueous solution at a range of concentrations and so an appropriate adjustment to the ratio of etchant to added de-ionised water was made to result in a 1 vol% solute solution.

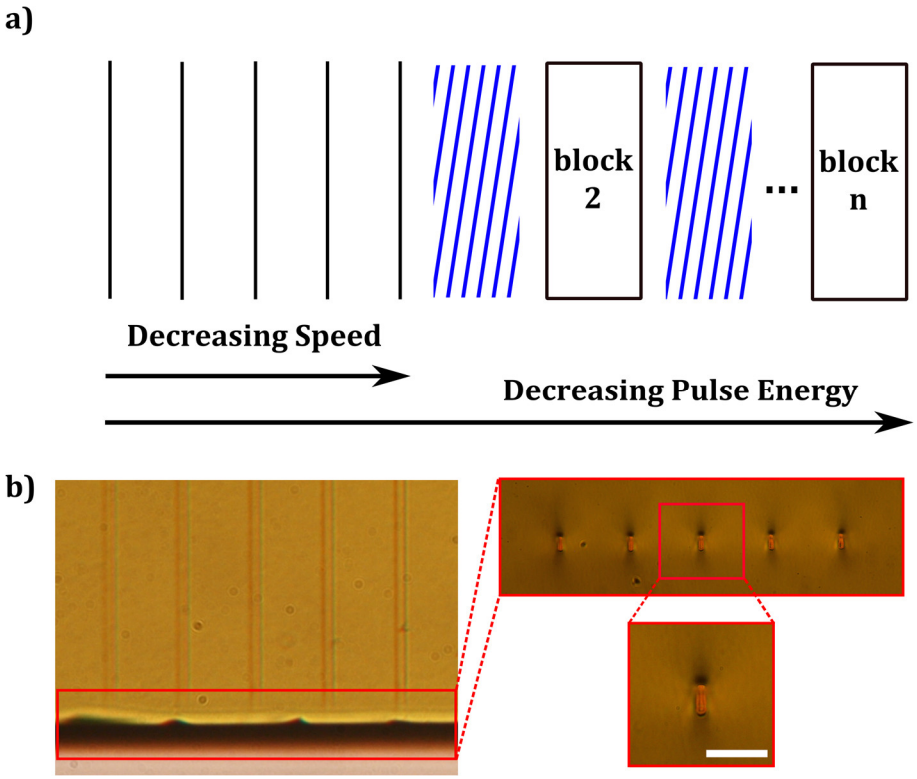

Figure 5-3 *Schematic and images of inscribed channels in GLS for etchant study. a) sample schematic showing series of sample translation speeds across a channel block which then repeats with decreasing powers. Blue hatched area signifies a double spacing so that the individual blocks could be easily identified. b) brightfield microscopy images of the 40 mW channel block from above and at the sample end facet. Channel pitch is 100 µm and a 100 µm scale bar is provided in the zoomed in image of the 4 mm/s channel.*

Etching trials were undertaken by immersing the diced sub-samples in the etchant solutions which were held in polytetrafluoroethylene (PTFE) beakers. Etching was performed at ambient temperatures and pressures without agitation. Selectivity

measurements were made by optical examination of the etched channel depth using brightfield microscopy and the known channel pitch as an in-sample graticule. Measurements were taken at 10 minutes and then hourly over the course of 4 hours and averaged. Bulk etch rates were determined by measuring the change in sample dimensions with Vernier calipers, at the same time intervals, and averaged over sample depth, width and height.

The results of the trials are summarised in Table 5-1 which lists the bulk etch rate, the maximum etch rate, the calculated selectivity and comments for each etchant. Amine etchants were found to be ineffective at either bulk or modified region material removal with no etching of any kind observed. In order to further establish the resistance of GLS to the tested amine etchants, samples were tested with neat amine etchants over the same 4-hour time period and also left in both 1 vol% amine solutions and neat amines overnight, giving a total exposure time of 21 hours. No response from the samples were observed in any case.

Of the remaining etchants, only the acidic etchants had any effect on the sample with HCL and nitric acid solutions showing selectivity. Across the range of channels inscribed in the sample no trends were observed with fabrication speed, but the modified region etch rate increased by approximately a factor of 2 between the 20 mW and 35 mW channel blocks. Above 35 mW, the etch rate was seen to stabilise with 35mW channels and 40 mW channels showing equal etch rates.

To validate the experimental methodology and to form a comparison with FLICE processing of silicate glasses fabricated using the same laser processing system, an etch trial on fused silica glass was performed using previously reported fabrication parameters [27]. For the trial, a series of multiscan channels were inscribed in fused silica samples with increasing powers from 80 to 340 mW in 20 mW steps. In this instance, 360 fs pulses at a repetition rate of 500 kHz, linear polarisation perpendicular to the writing direction, 0.4 NA focusing, and a constant 1 mm/s writing speed were used.

Table 5-1 *Summary of the bulk and maximum modified region etch rates for the collection of etchants tested. These were used to determine the etchants' selectivity and hence suitability for FLICE fabrication techniques. Diisopentylamine, morpholine and nitric acid are listed by their chemical formulas which are $C_{10}H_{23}N$, C_4H_9NO and NHO_3 respectively. Also included are the results from etching trials of neat amines, i.e. 100%, amine etchants with no solvent.*

Etchant + Solvent	Bulk [µm/hr]	Modified [µm/hr]	Selectivity (Mod/Bulk)	Notes
$C_{10}H_{23}N$ + DMSO	-	-	-	Unchanged
C_4H_9NO + DMSO	-	-	-	Unchanged
$C_{10}H_{23}N$	-	-	-	Unchanged
C_4H_9NO	-	-	-	Unchanged
HCL+ H_2O	5.4	72.1	13.3	Rough
NHO_3+ H_2O	7.6	56.6	7.5	Rough
HF + H_2O	42.6	-	1	Rough, Film Formation
KOH + H_2O	-	-	-	Unchanged

The samples were subsequently etched in 5 vol% HF aqueous solutions agitated using ultrasonic baths, and characterised in the same manner as the GLS samples. Modified region removal rates, given by etched channel depths, were seen to increase with higher powers, becoming constant for channels inscribed with average powers between 280 – 340 mW. A maximum modified region etch rate of 215 µm/hr was observed, with a bulk etch rate of 5.2 µm/hr, giving a selectivity ratio of ~ 40, this compares favorably with reported selectivity values for FLICE processing of fused silica using HF of up to 100. Figure 5-4 shows example images of GLS and fused silica channels after etching for direct comparison of channel width to depth ratios and surface quality.

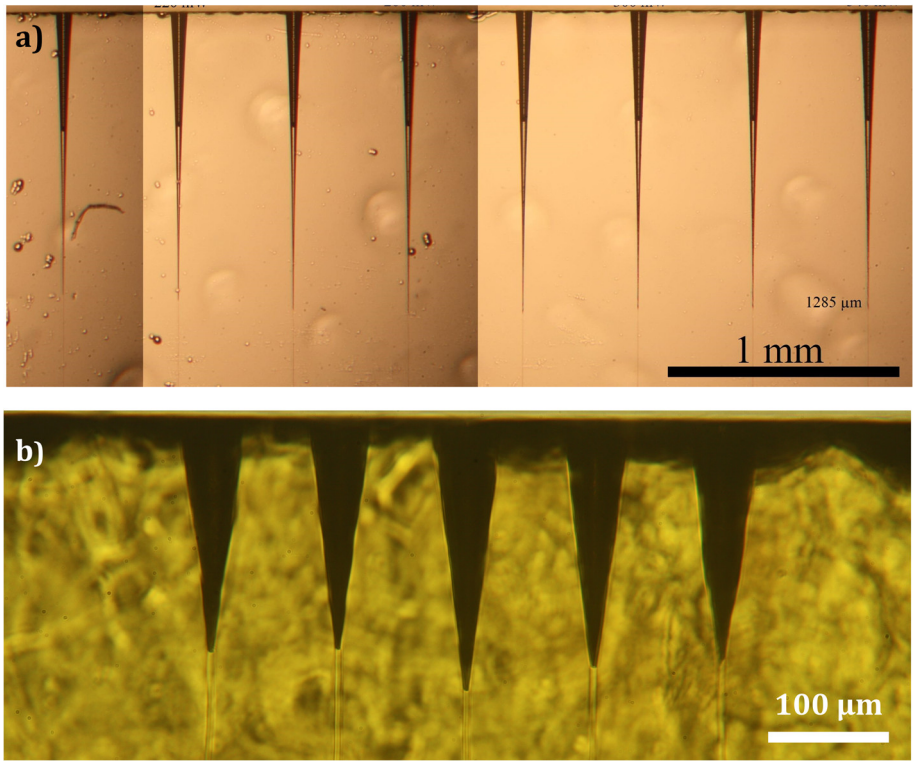

Figure 5-4 *Fused silica versus GLS etch trial comparison. a) Fused silica microchannels after 6 hours etching in 5 vol% HF aqueous solution. Left-to-right: 200 mW average power channel then steps of 20 to 340 mW average power channel. b) GLS microchannels written with 40 mW average power after 4 hours etching in 1 vol% HCL aqueous solution. Left-to-right: 16, 8, 4, 2, 1 mm/s translation speed.*

5.4 Optofluidic Device Design

With HCL identified as the best performing selective etchant of GLS from the etching trials, a compact optofluidic sensor design was formulated in order to investigate the potential of mid-IR GLS optofluidics. The optofluidic sensor chip was also fabricated in fused silica for direct comparison of FLICE processing in silicate and chalcogenide glasses.

The sensor design is shown in Figure 5-5 and consists of a 1 mm long central microfluidic channel with a 50 by 50 µm cross-section that links two 500 µm long 200 µm diameter inlet/outlet ports designed to connect to standard micro-fluidic tubing. This simple microfluidic circuit allows for a fluid sample to flow across the chip through a well-defined volume that can be optically probed. In order to perform measurements of fluid samples passed through the device, the central micro-channel is crossed by a waveguide

so that light can be delivered to the sample flow and the transmitted signal collected and analysed for sensing applications.

The photonic and microfluidic circuits sit within a 2 mm by 4 mm frame inscribed through the entire thickness of the GLS or fused silica substrates. As well as allowing the device to be written in larger sample substrates, a frame design was chosen as it provides scalability and simplifies the fabrication process, i.e. it gives the ability to produce arrays of pre-etch optofluidic devices in a single fabrication step that can subsequently be etched in a single processing step. Utilising frames also ensures the alignment of device features but prolongs the etching process as upon etching, the devices first need to be released from the larger substrate to reveal each individual device before the etchant can begin to dissolve the modified regions defining the chip microfluidic circuit.

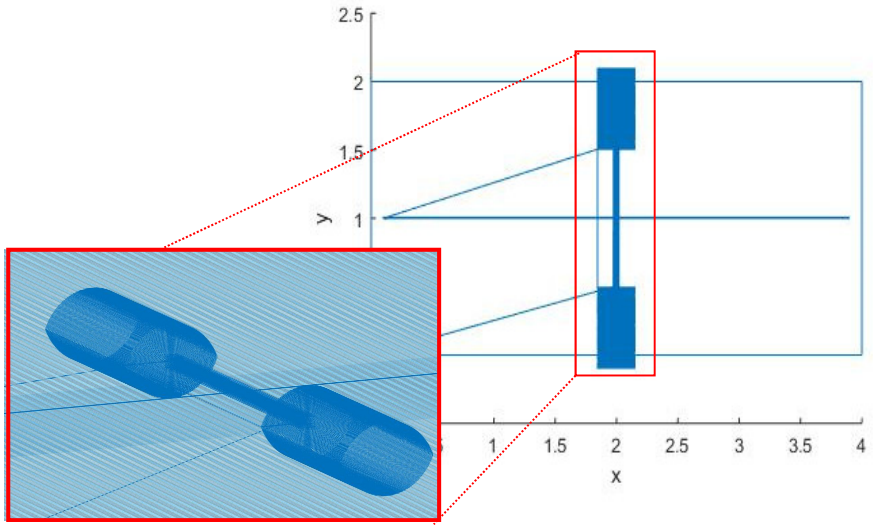

Figure 5-5 *Programmed stage movements showing the opto-fluidic sensor design. Top down view and zoomed in section of central section of device. Zoomed in section clearly displays elliptical inlets and waveguide crossing central channel.*

Considerations were made in the device design to counteract the lower selectivity that HCL demonstrates in FLICE processing of GLS in comparison with FLICE processing of fused silica using HF. One consideration was to limit the amount of time the devices need to etch and this was achieved by keeping the device narrow so that the microfluidic circuit could be short. Importantly this design restriction does not impact the complexity of the photonic components that can be integrated as the device can be made arbitrarily

wide without increasing the etching processing time. For GLS devices the frame was also written with an inverse taper to counteract the strong taper angles caused by low selectivity etching, as seen in the GLS micro-channels in Figure 5-4.

Due to the differences between the refractive index of air, approximately 1, and the opto-fluidic device substrates, GLS and fused silica around 2.45 and 1.45 at 1 μm, respectively, spherical aberration caused by refraction of the focused inscription beam at the air-sample boundary also needed to be taken into account in the sensor design. The index mismatch causes distortion of the inscription optic focus which shifts the focal position and lowers the intensity in the focal region [169]. For low NA focusing (≤ 0.4) higher order spherical aberration is not as apparent and a first order correction can be readily applied which consists of scaling motion along the optical axis by the inverse of the refractive index to correct for the focal position shift. Intuitively, in the ray optics picture, this offsets the lengthening of the focusing objective focal length caused by conservation of NA across a refractive index boundary. An easily visualised result of this scaling is the elliptical inlets/outlet design, seen in Figure 5-5, which results in circular inlets inscribed in the device.

5.5 Device Inscription and Etching

Using the design discussed in the previous section, arrays of pre-etch opto-fluidic devices spaced on a 4.5 mm by 4.5 mm grid were inscribed in 10 by 10 by 1 mm GLS samples and 20 by 20 by 2 mm fused silica samples.

Inscription parameters for the micro-fluidic components in the devices and for the device frames were based on the etching trial results reported in the previous sections. For the GLS devices, 1 ps pulses at 500 kHz were used and focused into the sample using a 0.4 NA aspheric lens. The inscribing beam polarisation was circular, and the inscribing power was held fixed at 50 mW. Fused silica devices were fabricated using the same repetition rate and focusing but with the pulse duration set to 360 fs, the inscribing beam polarisation was linear and kept perpendicular to the micro-channel write direction, and the inscribing power was set to 300 mW. In both materials the microfluidic components were written using a sample translation speed of 1 mm/s with the frames written at 5 mm/s.

In GLS and fused silica, the inscribing power was reduced for waveguide writing, set to 20 mW for GLS and 120 mW for fused silica, and a 10 mm/s translation speed was used. Other fabrication parameters were identical to the parameters used for frame and microfluidic component writing. In both substrates devices were inscribed with no evidence of cracking or introduction of other defects.

Once device arrays were written in the GLS and fused silica substrates, they were immersed in etching solutions to produce individual chips and to develop the pre-etch microfluidic components inscribed in the devices. GLS device arrays were etched in 1 vol% HCL aqueous solutions whereas fused silica arrays were etched in 5 vol% HF aqueous solutions. Etching was performed by placing the substrates and etching solutions in PTFE beakers with the etching solution agitated by placement of the beakers in an ultrasonic bath. The devices were periodically checked and removed once fully etched or deemed to have failed. The results of the opto-fluidic device fabrication trials can be seen in Figure 5-6.

From the device fabrication trials, it was found that fused silica devices could be produced reliably and repeatably, often with 100 % yields from each substrate. Individual chips were connectorised with microfluidic tubing and pressure tested using a syringe pump. On the other hand, no successful devices were produced in GLS. Although GLS devices could be successfully inscribed, during etching the lower selectivity of the HCL etchant between modified and un-modified regions consistently led to surface breaching of the inlet/outlet ports and etching of the waveguide regions.

These fabrication trials indicate that a modest increase, by around a factor of four, in the attainable selectivity for FLICE processing of GLS, equaling the demonstrated etching selectivity for FLICE processing of fused silica, would result in highly repeatable, high yield production of mid-IR transmitting, highly nonlinear optofluidic devices. Meeting this goal would allow for a new range of optofluidic devices for applications in the mid-IR, such as offering sensing modalities that are not possible in fused silica.

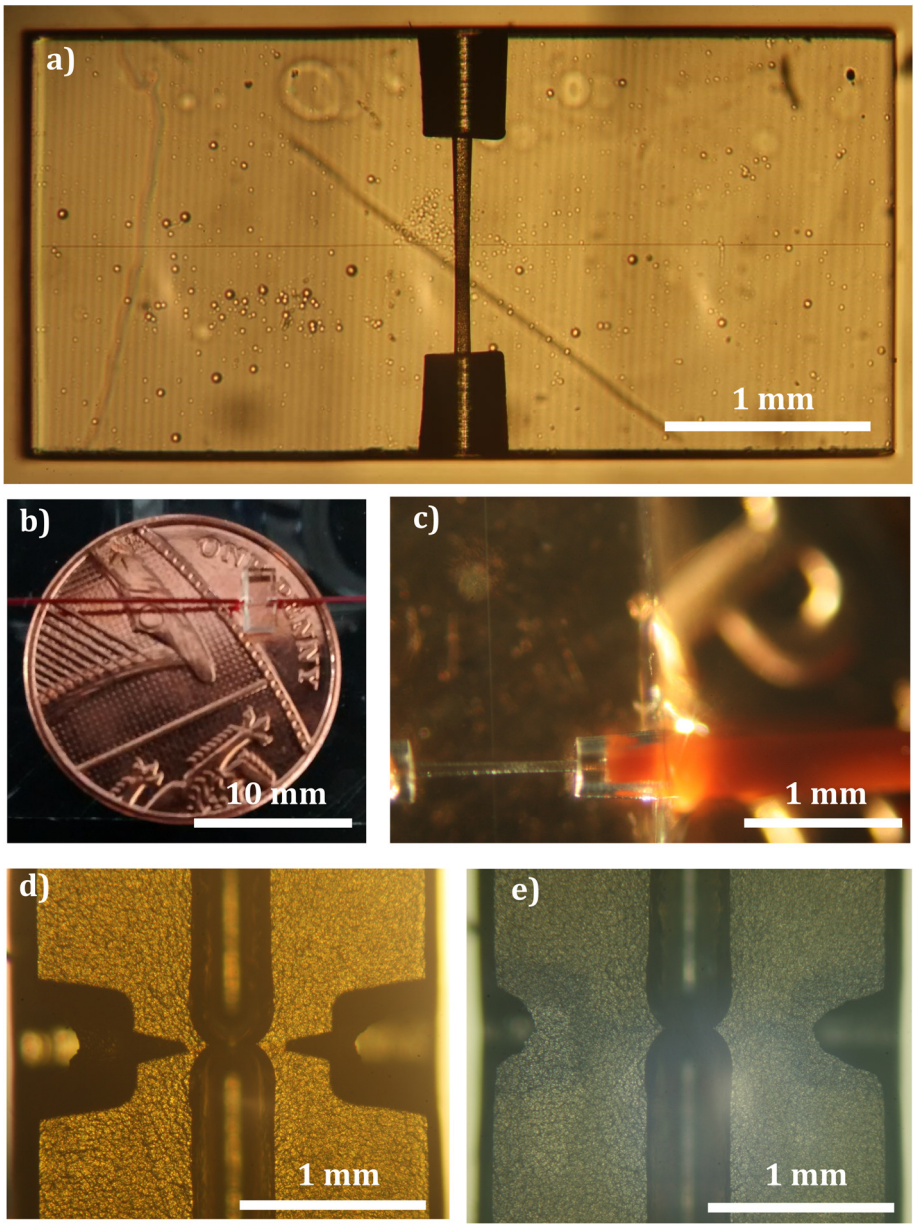

Figure 5-6 *Images of the outcome of device fabrication testing in GLS and fused silica highlighting the remaining challenges for FLICE fabrication of GLS optofluidics. a) composite microscope image of fully etched optofluidic device in fused silica showing microfluidic channel and light delivery/collection waveguides. b) and c) images of connectorised fused silica chip. d) and e) microscope images, under transmission and reflection illumination respectively, illustrating the results of GLS device fabrication trials. Breaching of the device top surface can be clearly seen on the inlet/outlet ports and the waveguide sections.*

5.6 Summary

This chapter has presented preliminary work on the FLICE processing of GLS glass with a view to fabrication of mid-IR optofluidic devices. To the best of our knowledge, this work is the first report of selective chemical etching of bulk chalcogenide glasses using the FLICE fabrication technique.

The Chapter began with an introduction to micro- and opto-fluidics along and a discussion of devices fabricated by ULI using silicate glasses as the substrate material. This was followed by an overview on the work which has been undertaken in wet chemical etching of chalcogenide glass thin films. The next section detailed the etching of ULI fabricated micro-channels in GLS using various concentrations of inorganic and organic wet chemical etchants in solution with the results compared with FLICE processing of fused silica micro-channels inscribed using the same inscription setup. For GLS, a maximum etching selectivity of ~13.3 was measured for 1 vol% solutions of HCL in de-ionised water whereas in fused silica a selectivity of ~40 was observed. The GLS etching trials also showed that the basic organic and inorganic etchants used to structure chalcogenide thin films have no discernible effect on bulk GLS glass.

The next section discussed an optofluidic sensor designed to compensate for the lower etching selectivity observed for FLICE processing of GLS in comparison to fused silica. A final section describes the progress towards fabrication of a demonstrator optofluidic sensor in GLS to illustrate the potential of the tested techniques for robust chip-scale opto-fluidic sensors. Although devices could be successfully inscribed in GLS with no evidence of sample cracking or inducement of defects, etching of the inscribed opto-fluidic chips lead to the devices failing before the complete etching on the microfluidic components. The most common failure route being over etching of inlet/outlet ports causing sample surface breaching or the etching of sensor waveguides.

The successful fabrication of opto-fluidic sensor chips in fused silica devices indicates that a modest improvement in etching selectivity of GLS to comparable values shown in fused silica would be the final step in realising the FLICE fabrication mid-IR optofluidic devices in chalcogenide glasses.

The work in this chapter was presented at Photon 16 [170].

Chapter 6 Waveguides in Thulium-doped Lutetium Oxide for Compact Mid-IR Lasers

This Chapter details the first demonstration, to the best of our knowledge, of ULI waveguide fabrication in a sesquioxide material, namely Thulium-doped Lutetium Oxide ($Tm:Lu_2O_3$) ceramic, and the demonstration of a ULI waveguide sesquioxide laser. The Chapter begins with a brief discourse on laser theory which is followed by an overview of the mid-IR emitting ULI channel waveguide lasers demonstrated to-date and the previous work in mid-IR bulk laser systems using $Tm:Lu_2O_3$ crystals or ceramics as their gain media. The next section gives details on how a suitable ULI parameter range was found to produce ULI waveguides in $Tm:Lu_2O_3$ and how the guiding characteristics of the waveguides were subsequently measured. A final section presents the results of laser development using ULI fabricated waveguides in $Tm:Lu_2O_3$ ceramic and discusses the characteristics of the resulting chip scale ULI waveguide laser.

Waveguide laser operation at 1942 nm was successfully demonstrated with an output power of up to 81 mW utilising a simple Fabry-Pérot laser cavity. These results show how combining the unique properties of sesquioxides, discussed in Chapter 2, with a ULI waveguide laser geometry could provide a means to produce compact, low-threshold and efficient laser sources near 2 μm with the potential for high pulse repetition rate ultrafast operation. As well as their utility as mid-IR laser sources, such chip scale lasers would also create new opportunities as compact pumps for mid-IR supercontinuum generation sources, such as those shown in Chapter 4, or for mid-IR OPOs.

6.1 Basic Principles of Laser Operation

Fundamentally, the operation of a laser is dependent on a type of resonant light-matter interaction referred to as stimulated emission. In the photon picture, this process is described by the stimulated demotion of an excited electron in a material to a lower energy state by the passage of an incident photon whose energy matches the difference between the two electronic states involved in the transition. To facilitate this change, the electron emits a photon of the same energy, direction, frequency, phase, and polarisation of the incident photon which therefore amplifies the incident light field.

Stimulated emission has been shown through both classical analysis, using Boltzmann statistics and blackbody radiation arguments, and quantum mechanical analysis, using quantum electrodynamics, to be the inverse of the absorption process introduced in Chapter 2 and as such, the occurrence of stimulated emission and absorption between two non-degenerate energy levels has the same probability. This is highlighted by the rate equation relations that describe the change in population of electrons in a non-degenerate two-level system, as seen in Figure 6-1, where absorption reduces the number of electrons occupying E_0, the ground state, whilst stimulated emission reduces the number of electrons in E_1, the excited state [2]:

$$\left(\frac{\partial N_0}{\partial t}\right)_{\text{Abs}} = W_{01}N_0 = \sigma_{01}F \qquad 6\text{-}1$$

$$\left(\frac{\partial N_1}{\partial t}\right)_{\text{Stim}} = W_{10}N_1 = \sigma_{10}F \qquad 6\text{-}2$$

$$W_{01} = W_{10} \Rightarrow \sigma_{01} = \sigma_{10} \qquad 6\text{-}3$$

where N_0 (N_1) is the number of electrons in the ground (excited) state, W_{01} (W_{10}) is the absorption (stimulated emission) rate, σ_{01} (σ_{10}) is the absorption (stimulated emission) cross section, and F is the incident photon flux.

For a two-level system in thermodynamic equilibrium electron level populations are governed by Boltzmann statistics and therefore $N_0 > N_1$. From equations 6-1 to 6-3, we can see that this leads to depletion of an incident light field as there are more electrons available in the ground state that contribute to absorption than those in the excited sate that provide gain. Pumping the system, such as with an intense light field, drives the two-level system into a non-equilibrium state but unfortunately, for a two-level system, the identical transition rates for absorption and stimulated emission leads to an equal number of ground state and excited state electrons in the limit of intense pumping and so a population inversion, which would be required to amplify an incident light field, cannot occur. In the limit where $N_1 = N_0$ the material becomes optically transparent but provides no gain.

It is worth reiterating this is a fundamental limit and does not consider decay processes that deplete the electron population in the excited state and make achieving amplification even more challenging. These include radiative decay through spontaneous emission and non-radiative decay through phonon emission.

Although two-level systems cannot be used to create a population inversion, the provision of additional electronic states enables energy level configurations where population inversion, and hence gain of the incident signal field, is attainable with sufficient pumping. These configurations can be three-level, quasi-three-level or four-level systems and are shown in Figure 6-1.

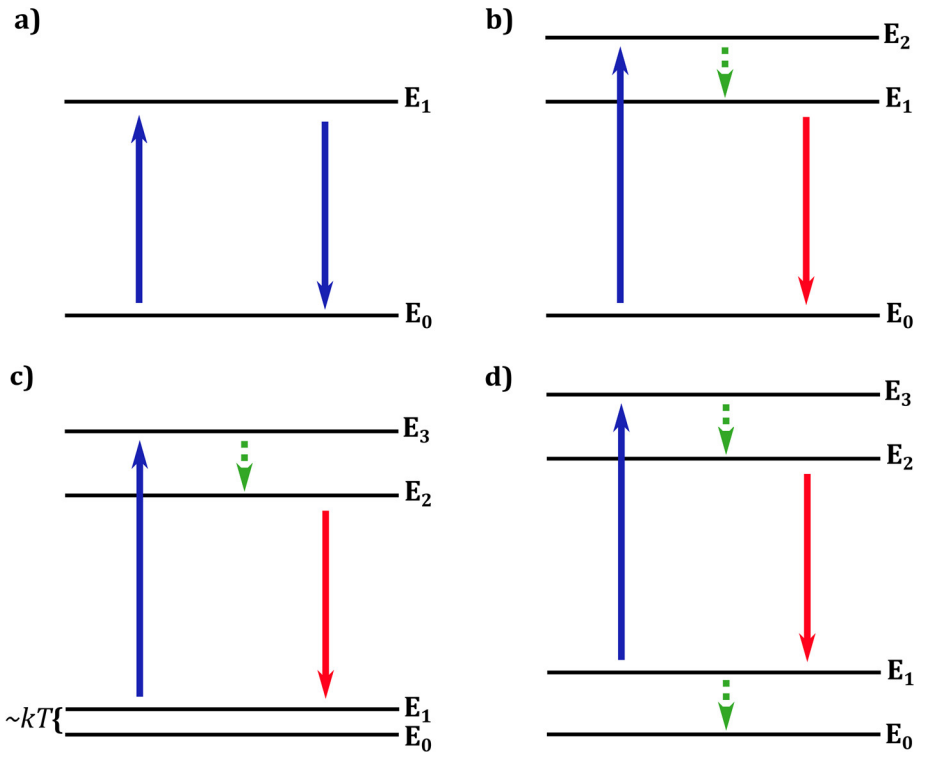

Figure 6-1 *Energy level configurations for a two-level system and the systems suitable for providing optical gain, where: a) two-level system, b) three-level system, c) quasi-three-level, and d) four-level system. Solid arrows signify radiative electron transitions where upwards pointing arrows are photon absorption events and downward facing arrows are photon emission events. Blue arrows are transitions mediated by pump photons whereas red arrows refer to signal photons. Green dashed arrows are non-radiative electron transitions and curly braces represent coupled levels with energy separation ≤ kT, where k is Boltzmann's constant and T is the temperature of the system.*

The degree to which a material exhibits three-level, quasi-three-level or four-level characteristics is often dependent on the wavelength of emission as this dictates the specific energy levels used from the set of optically active levels offered by the material. The $Tm:Lu_2O_3$ ceramic gain media used in this Chapter exhibits quasi-three-level characteristics for 2 μm signal emission and so the relationships governing laser performance which are presented in the rest of this section will be with respect to quasi-three-level systems. These relationships for laser threshold power, slope efficiency and output power are derived from rate equations that describe the change in electron populations for a quasi-three-level system, assuming steady state operation and uniform optical pumping. Only the results are stated as the full derivations can be found elsewhere [13].

The basic building blocks of a laser are: the gain medium, a resonator cavity to provide feedback, and a pump source to provide the energy required to invert the gain media. Using these building blocks, laser oscillation can begin when a threshold condition is reached, namely that the round-trip cavity gain experienced by the intracavity field equals the round-trip cavity loss. This occurs at a certain threshold pump power, P_{th}, which is given by:

$$P_{th} = \left(\frac{\gamma + \sigma_a N_t l}{\eta_p} \right) \left(\frac{h\nu_p}{\tau} \right) \left(\frac{A}{\sigma_e + \sigma_a} \right) \qquad 6\text{-}4$$

where γ is the logarithmic loss of the cavity, given by $\gamma = \gamma_i + \gamma_{oc}/2$; γ_i is the logarithmic internal loss, given by $\gamma_i = -\ln(1-L_i)$, with L_i the internal loss per pass; γ_{oc} is the logarithmic loss of the output coupler, given by $\gamma_{oc} = -\ln(1-T_{oc})$, with T_{oc} the transmission of the output coupler; σ_a is the effective absorption cross section of the lower laser level; N_t is the total number of electrons in the upper and lower laser levels; l is the length of the gain medium; η_p is the pump absorption efficiency, given by $\eta_p = P_a/P_i$ with P_a the absorbed power and P_i the incident power; h is Planck's constant; ν_p is the frequency of the pump light; τ is the radiative lifetime of the upper laser level; A is the cross-sectional area of the pumped region in the gain material; and σ_e is the effective emission cross section of the upper laser level.

Above threshold, the laser output power tends to follow a linear relationship with respect to increases in pump power which is characterised by a slope efficiency. This value depends on several factors, as can be seen in:

$$\eta_s = \left(\frac{A_b \gamma + \sigma_a N_t l}{\sigma_e + \sigma_a} \right) \left(\frac{h\nu}{\tau} \right) \left(\frac{\gamma_{oc}}{2} \right) \left(\frac{1}{P_{th}} \right) \qquad 6\text{-}5$$

where A_b is the cross-sectional area of the laser beam the gain medium and v_L is the frequency of the laser light.

For clarity, equation 6-5 can be rewritten as a product of separate system efficiencies, by substituting in equation 6-4, leading to:

$$\eta_s = \eta_p \eta_c \eta_q \eta_t \qquad 6\text{-}6$$

where η_c is the output coupling efficiency, given by $\gamma_{oc}/2\gamma$; η_q is the quantum efficiency, given by $h\nu_L/h\nu_p$; and η_t is the transverse overlap efficiency, given by A_b/A.

Using the given definitions for the threshold pump power and the laser slope efficiency, the output power from a laser can be succinctly written as:

$$P_{out} = \eta_s (P_p - P_{th}) \qquad 6\text{-}7$$

where P_p is the pump power.

In order to maximise the output power attainable from a laser system an important consideration is the optimal output coupling which can be adjusted by changing the transmissivity of output coupler mirror. From equations 6-4 and 6-5 there is an inverse relationship between threshold pump power and slope percentage with respect to changes in output coupling. As cavity losses include light coupled out of the cavity for the output laser beam, reducing the output coupling lowers the threshold pump power and therefore in isolation would increase the laser output power from equation 6-7. On the other hand, once a laser has reached threshold a larger output coupling leads to higher slope efficiency

as a larger fraction of the intracavity field is emitted which in isolation would also increase the laser output power from equation 6-7.

This section has discussed the physical mechanisms which enable laser operation, namely stimulated emission and population inversion, and presented the equations that dictate the output power, threshold power and slope efficiency of uniformly pumped quasi-three level lasers. For brevity there has been almost no discussion on specific design decisions on the three basic building blocks of any laser system, i.e. the active material, pumping scheme and resonator design. It is important to note that as well as affecting simple properties of the laser output, such as in the example given of output coupler mirror transmissivity on maximum laser output power, these building blocks can fundamentally change the nature of the emitted laser beam. Examples include strategies to enforce high output beam quality through control of the transverse mode order of the laser resonator; narrowing the linewidth of the emitted spectrum with frequency selective elements; and inducing a pulsed output either actively, driven by control electronics, or passively, driven by the intracavity light field. From a practical perspective, building block design decisions will also have a large bearing on a lasers SWaP and cost.

6.2 ULI waveguide lasers

The applicability of ULI for the fabrication of three dimensional photonic structures across a broad range of transparent dielectrics as discussed in Chapter 1 has led to ULI waveguide lasers being demonstrated using numerous solid-state gain media [171, 172]. Also, from examination of the output power and threshold equations given in the previous section, it can be seen that waveguide lasers have inherent benefits over their solid-state bulk laser counterparts which can be attributed to operating with a guided mode for pump and signal light and will now be discussed.

In a waveguide geometry, as both the pump light and signal emission are confined and copropagating through the same region in the medium, lower lasing thresholds can be attained through the reduction in pump volume as can be seen in equation 6-5. For solid-state bulk lasers pump volume reductions are limited by beam diffraction and so a waveguide solution can allow for lower SWaP pump sources to be used, thus reducing system complexity and footprint. ULI waveguide laser development is also attractive due to their potential in creating extremely compact chip-scale sources based on well-proven

solid-sate gain media. This is again due to operation with guided modes which allows for the entire cavity defined by the crystal size if cavity mirrors are coated directly onto the gain medium end facets.

By offering robustness and insensitivity to vibration or misalignment, compact micro-chip sources also benefit single-frequency operation, desirable in applications such as optical clocks, with narrow linewidths possible through the addition of ULI written frequency selective elements, like Bragg gratings, directly into the inscribed waveguides [98]. Conversely, chip-scale sources can also benefit high repetition rate ultrashort pulse lasers, where broad bandwidth emission is required, desirable for sensing applications as source repetition rate is directly related to the roundtrip time of circulating intra-cavity pulses [173].

Considering the mid-IR region, ULI channel waveguide lasers have been realised in rare-earth doped glasses with one of the first demonstrations being in fluorogermanate glass doped with thulium, namely GPNG ($56GeO_2 – 31PbF_2 – 9Na_2O – 4Ga_2O_3$). Type I multiscan waveguides in Tm:GPNG where shown to output a maximum of 32 mW at 1.93 μm for 620 mW of pump power with a slope efficiency of 6% [174]. For this work, the laser cavity was a Fabry-Pérot cavity design and the pump source was a CW Ti:sapphire laser tuned to emit at 791 nm. In addition to the maximum laser emission at 1.93 μm the Tm:GPNG ULI waveguide laser could be tuned by output coupler angle to emit over a range spanning 1.89 μm to 1.94 μm.

Subsequent work in rare-earth doped ZBLAN glasses produced ULI waveguide sources with deeper IR emission and higher slope efficiencies based on writing depressed cladding structures. One example being Thulium-Holmium-doped depressed cladding waveguides in ZBLAN which have been shown to produce up to 76 mW at 2.052 μm for 360 mW of pump power with a slope efficiency of 20% [175]. The co-doping of rare-earth ions in the ZBLAN host allowed for efficient operation of holmium laser transitions with a 790 nm CW Ti:sapphire pump due to energy transfer from excited thulium ions driving a population inversion in the holmium ions. Whilst beneficial for near-IR pumping of holmium, co-doping can lead to complicated laser dynamics [176], as is evident by the emission of the Tm,Ho:ZBLAN ULI waveguide laser switching to thulium laser emission lines in the range of 1.88 to 2 μm for larger output coupling values.

Another example of efficient mid-IR laser emission from rare-earth doped ZBLAN waveguide lasers comes from Ho:ZBLAN depressed cladding waveguides pumped by a gain switched 1150 nm fibre coupled diode laser [177]. In this instance, laser emission at 2.9 μm was observed with a maximum output power of 27 mW and a 19.5% slope efficiency. A pulsed pump source was required to overcome the limitations of the 2.9 μm laser transition in holmium which, whilst seeming being an ideal four-level system, has a longer radiative lifetime for the lower laser level that inhibits population inversion except in the case of transient pumping or co-lasing of the 2.9 μm lower laser level.

Demonstrations of mid-IR ULI waveguide lasers written in crystalline or ceramic gain media have been predominantly rare-earth doped or transition-metal doped YAG and ZnSe. In thulium-doped YAG ceramic, type II cladding waveguides have been shown to produce up to 90 mW output power at 1.985 μm for 660 mW of input power with a slope efficiency of 27% and threshold of 312 mW [178]. These best performance figures, in terms of slope efficiency and maximum output power, were observed for waveguides exhibiting a large number of higher order modes. Single mode type II cladding waveguides in the same sample where found to output 56 mW with a slope efficiency of 13.2% albeit with a lower laser threshold of 100 mW.

Similar Type II cladding waveguides written in chromium-doped ZnSe were first shown to generate 285 mW laser emission at 2.486 μm for 1.11 W of incident pump power with a slope efficiency of 45% [179]. The achieved slope efficiency is one the highest reported for any mid-IR ULI waveguide laser although it is important to note that the pump source used, a thulium fibre laser emitting at 1.928 μm, provides a much smaller quantum defect than the near-IR pump sources used for the thulium and holmium lasers which have been discussed.

Based on the previous work presented above, there is scope for further mid-IR ULI waveguide source development in novel gain materials provided they can offer an advantage over the ULI waveguide lasers presented thus far. To this end, it is logical to consider gain media used in high-performance mid-IR emitting bulk lasers to focus the search for mid-IR ULI waveguide laser development. One such gain medium is the rare-earth doped sesquioxide Tm:Lu_2O_3, which possesses beneficial thermo-optical properties as discussed in Chapter 2.

In particular, the host material Lutetia allows for high doping concentrations, and when doped with thulium emits a broad gain spectrum which covers >300 nm and extends well beyond 2 µm [88]. These inherent properties of Tm:Lu_2O_3 have led to the demonstration of 75 W of CW laser output around 2 µm with a tuning range of >200 nm under direct laser diode pumping [83]. Moreover, the broad gain spectrum of Tm:Lu_2O_3 has allowed for the generation of 180 fs pulses from a modelocked source which also demonstrated sub 400 fs pulses with a centre wavelength tunable over a 70 nm range, as seen in Figure 6-2.

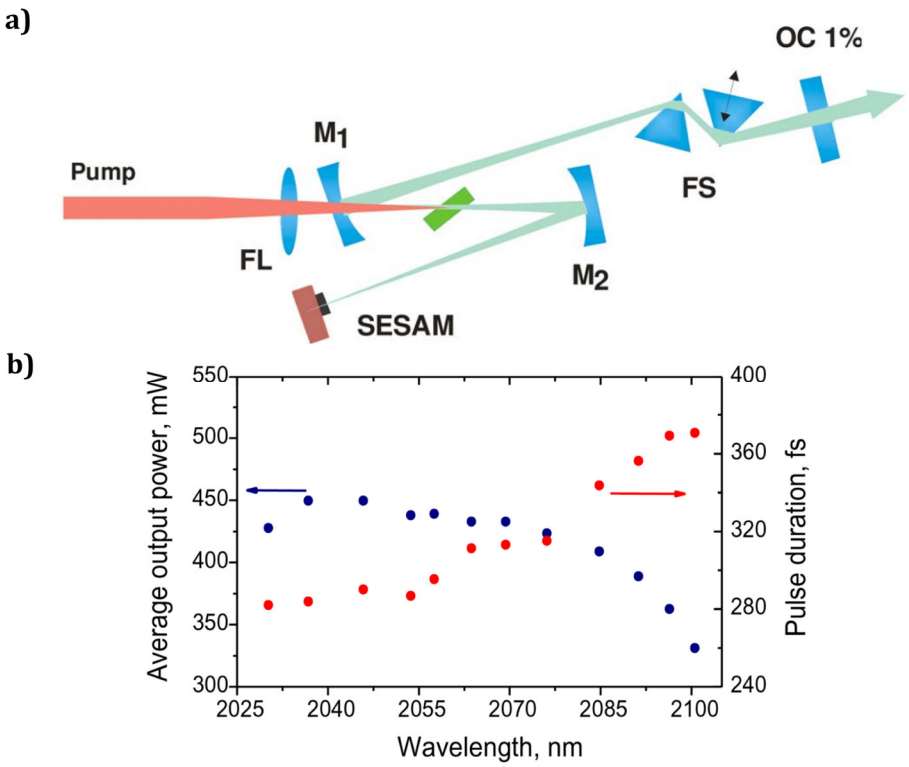

Figure 6-2 *Mode-locked bulk Tm:Lu_2O_3 ceramic laser. a) Cavity schematic, where: FL, focusing lens (f = 63 mm); M1 and M2, plano–concave high-reflective mirrors (r1 = −75 mm, r2 = −100 mm); OC, output coupler (T = 1% at. 2000 nm); and FS, pair of fused silica prisms. b) Tunability of the mode-locked Tm:Lu_2O_3 ceramic laser. Adapted from [82, 180]* .

The unique properties of Tm:Lu_2O_3 offers the chance for efficient mid-IR ULI waveguide laser sources with direct diode pumping allowing for lower SWaP pump systems which along with the ULI waveguide geometry would provide a means to produce compact, low-threshold and efficient laser sources near 2 µm with the potential for high pulse repetition rate ultrafast operation [173, 181]. The following sections report the first demonstration of optical waveguides in Tm:Lu_2O_3 ceramic fabricated by ULI and

demonstrate waveguide laser operation at 1942 nm with output powers of up to 81 mW using a simple and compact Fabry-Perot cavity design.

6.3 Waveguide Fabrication and Passive Characterisation

As discussed in Chapter 2, the type of waveguide which can be produced by ULI is heavily dependent on the material properties of the substrate and the inscribing laser parameters. In order to explore the range of induced refractive index change in Tm:Lu_2O_3 ceramic, arrays of 10 mm long track waveguides were fabricated using different pulse energies and track separations. The arrays were fabricated in a 2.3×5×10 mm substrate of 1 at.% Tm^{3+}-doped Lu_2O_3 ceramic (Konoshima Chemicals). The doping concentration of Tm^{3+} ions in the host ceramic was confirmed by comparison of the Tm:Lu_2O_3 substrate pump light absorption to previously reported results. This established that the doping concentration was within the 1 at.% range with an effective absorption coefficient of 0.68 cm^{-1} at 796 nm measured.

The ULI fabrication system used for waveguide inscription was the NLO group laser processing setup reported in previous Chapters. In this instance the ultrafast laser used for writing was a Yb-doped KGW bulk laser source (PHAROS, Light Conversion – provided by Photonic Solutions Ltd., Edinburgh) which emitted 200 fs pulses at a 500 kHz pulse repetition rate with a centre wavelength of 1040 nm. This source was used in preference over the IMRA μ-Jewel D400 system mentioned in Chapters 4 and 5 due to its capability to emit higher pulse energies which can be advantageous for track waveguide writing.

The waveguides themselves were written 350 μm beneath the sample surface using circularly polarised light focused with a 0.4 NA aspheric lens giving a spot diameter of approximately 1.8 μm. The transverse writing geometry was selected for waveguide fabrication with a constant 5 mm/s translation speed. Due to the thermal diffusivity of Tm:Lu_2O_3 and the focal spot diameter used in the ULI process the waveguides were fabricated in the non-thermal regime, as given by [182]:

$$f_{cr} = \frac{D_{th}}{d^2} \qquad 6\text{-}8$$

where f_{cr} is the critical frequency which occurs when the time between pulses matches the heat diffusion time from the focal volume, D_{th} is the thermal diffusivity of the material and d is the focal spot diameter. Using the known spot size and thermal properties of Tm:Lu_2O_3 given in Chapter 2, the critical frequency is determined to be approximately 1.7 MHz.

Waveguide depth was selected to avoid surface ablation during writing and with consideration of the working distance of the objective and the sample thickness. The writing speed was chosen by taking into account the capabilities of translation stages, writing time, and ensuring good overlap of the pulses in the sample during writing. The pulse energy across the waveguide arrays was varied from 0.4 - 5 μJ with track separations of 20 μm and 30 μm. After the fabrication process the sample end facets were ground back to remove any defects caused by clipping of the inscription beam near the sample edge and re-polished to optical quality giving a final waveguide length of 9 mm. Brightfield microscopy images of the resulting structures can be seen in Figure 6-3.

Inspection of the array of waveguides shows a clear change in the cross sections of the inscribed tracks with uniform material modification confined to the focal volume at lower powers and elongated disordered track cross sections for the highest power scans. The elongated tracks extend upstream towards the sample surface in the pre-focal region of the inscribing beam which is indicative of self-focussing and filamentary propagation.

After inspection an initial study of the guiding characteristics of the waveguides was undertaken with a 980 nm fibre coupled diode laser using the setup depicted in Figure 6-4. The fibre used was a single mode step-index silica fibre (1060XP, Thorlabs), which has MFD of 5.9 μm ± 0.5 μm at 980 nm and an NA of 0.14, and was wound onto a three-paddle polarisation controller (FPC030, Thorlabs) to manage the output beam polarisation state.

The fibre output was subsequently collimated using an aspheric lens with a focal length of 2.75 mm and then coupled into the waveguides using a second aspheric lens with an 11 mm focal length. This results in a coupling spot diameter size of 24 μm as calculated by the conservation of the beam parameter product (BPP) under the paraxial approximation which gives:

$$\omega_1 = \omega_0 \times \frac{f_2}{f_1} \qquad 6\text{-}9$$

where ω_0, ω_1 are the beam waist radius of the output fibre mode and the coupling spot, and f_0, f_1 are the focal lengths of the collimation and coupling lens, respectively.

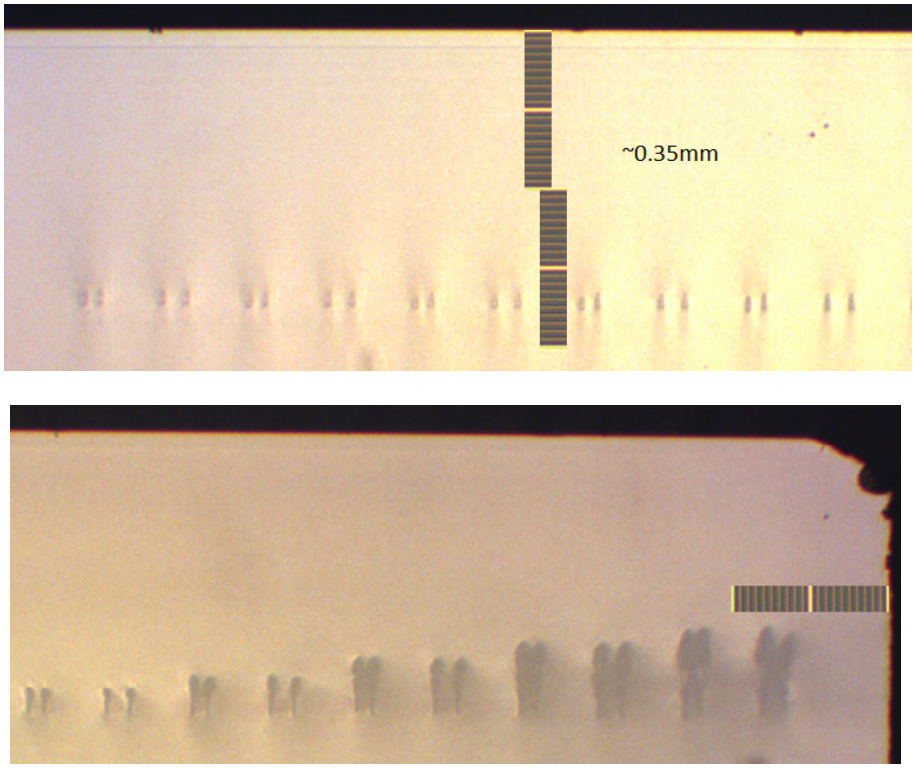

Figure 6-3 *Brightfield microscope images showing the resulting material modification caused by waveguide writing. Top: waveguides in the low power range from 0.4 to 0.8 μJ. Bottom: waveguides in the high power range from 1.5 to 5 μJ. The inscription laser was incident from above in both cases. Microscope images contain overlaid to-scale graticule images which have a 10 μm pitch.*

Type I guiding was observed for the track waveguides written with pulse energies from 0.4 – 0.8 μJ, where the guiding mode overlaps with the modified regions, as shown Figure 6-4. This was confirmed by backing off the coupling lens to allow simultaneous coupling into both modification lines in a track waveguide and comparing the guiding region spacing with the known track separation. Type II guiding with good mode confinement was observed in the structures inscribed at pulse energies between 0.9 – 3 μJ as can also be seen in Figure 6-4. In this pulse energy range the tracks with separations of 20 μm were found to support single mode guiding at 980 nm whereas the 30 μm separated tracks were found to be multimode. Guiding in the Type II regime was found to be strongly

polarisation dependent with only light polarised parallel to the y-axis guided. The stress induced in the irradiated tracks during the inscription process, which enables Type II guiding, and the asymmetry of the track waveguide design is the likely cause of the strong polarisation dependence. The results of the guiding characteristics study are summarised in Table 6-1.

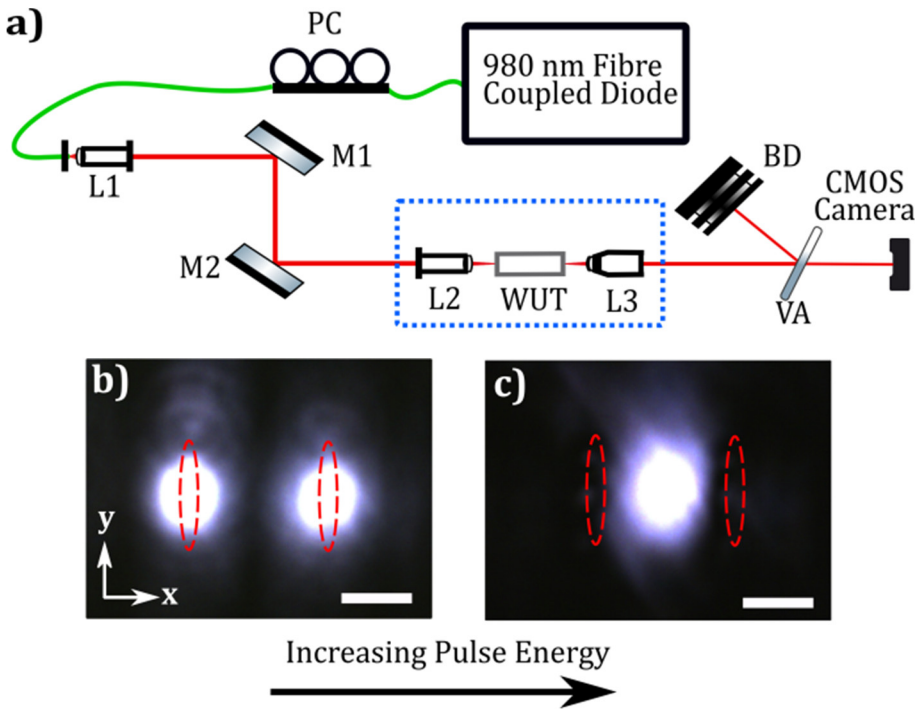

Figure 6-4 *(a) Experimental setup for initial waveguide characterisation. PC, three paddle fiber polarisation controller; L1 and L2, AR-coated aspheric lenses; M1 and M2, silver mirrors; WUT, waveguide under test; L3, ×20 objective; VA, reflective variable ND filter; BD, beam dump. Blue dotted box signifies components mounted on waveguide alignment workstation. (b) and (c) Mode images for Type I and II guiding in Tm:Lu_2O_3 waveguides with 20 µm track separations, respectively. Red dashed ellipses indicate the area of the inscribed tracks. A 10 µm scale bar is included.*

Table 6-1 *Summary of the guiding characteristics of inscribed track waveguides in Tm:Lu_2O_3 for different pulse energy and track separation combinations, where SM signifies single mode guiding behaviour and MM signifies multi-mode guiding behaviour.*

Pulse Energy (µJ)	Track Separation (µm) – Guiding?/ Type I? /Type II? /SM? /MM?
0.4	20 – Type I, 30 – Type I
0.5	20 – Type I, 30 – Type I
0.6	20 – Type I, 30 – Type I
0.7	20 – Type I, 30 – Type I
0.8	20 – Type I, 30 – Type I
0.9	20 – Not guiding, 30 – poor confinement Type II + MM
1.0	20 – Not guiding, 30 – poor confinement Type II + MM
1.1	20 – Not guiding, 30 – poor confinement Type II + MM
1.2	20 – Not guiding, 30 – poor confinement Type II + MM
1.3	20 – Type II SM, 30 – Type II MM
1.4	20 – Type II SM, 30 – Type II MM
1.5	20 – Type II SM, 30 – Type II MM
2.0	20 – Type II SM, 30 – Type II MM
3.0	20 – poor confinement Type II SM, 30 – Type II MM
4.0	20 – Not guiding, 30 – poor confinement Type II MM
5.0	20 – poor confinement Type II SM, 30 – Not guiding

6.4 Waveguide Laser Results

In order to test the potential for lasing from the inscribed waveguides, a cavity was formed around the sample using two plane dielectric mirrors mounted adjacent to the uncoated 2.3 × 5 mm end facets, as shown in Figure 6-5. The input pump mirror was coated for a high reflectivity in the range of 1.9 – 2.1 µm and a high transmission at the pump wavelength of 796 nm, whereas the output couplers with transmission of 2%, 9%, 20%, 30%, 40% and 75% between 1.9 – 2.1 µm were used, forming a standing wave cavity.

The pump source was a tunable Ti:sapphire laser producing linearly polarised light with a maximum output power of 2 W at 796 nm. The slightly astigmatic pump beam was coupled into the waveguides using an aspheric lens with a 20 mm focal length resulting in an average diameter spot size of 27.5 µm. In order to thermally stabilise the cavity, the mounting bracket for the sample was water cooled keeping the sample mount at a constant temperature of 20 °C.

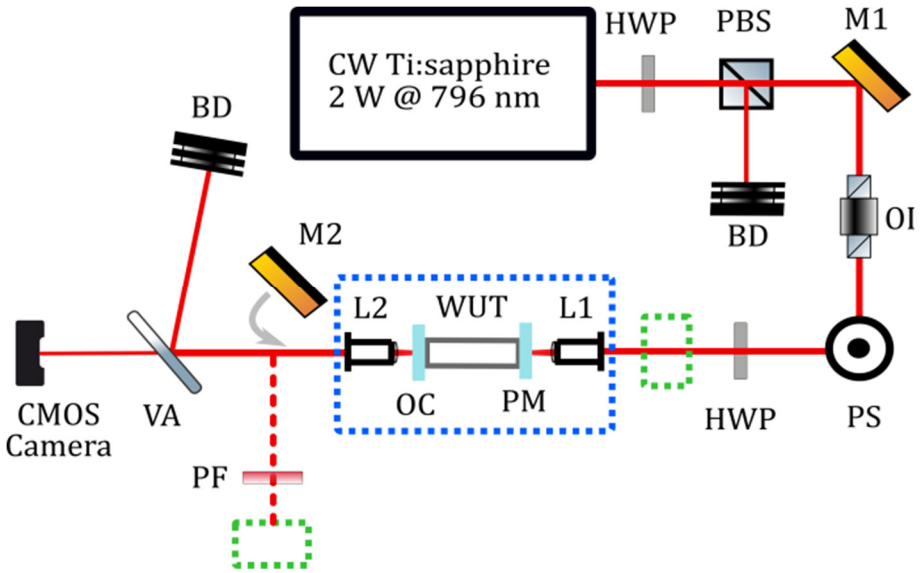

Figure 6-5 *Waveguide laser experimental setup. HWP, half-wave plate; PBS, polarising beam splitter; BD, beam dump; M1 and M2, gold mirrors; OI, optical isolator; PS, periscope; L1 and L2, AR-coated aspheric lenses; PM, pump mirror; WUT, waveguide under test; OC, output coupler; VA, reflective variable ND filter; PF, optical filter. Blue dotted box signifies components mounted on waveguide alignment workstation. Green dotted box signifies power meter or detector positions.*

In this configuration the pump light was coupled into each waveguide in the array in turn with the alignment checked at low power using an aspheric lens to image the waveguide end facet onto a CMOS camera sensor. The fluorescence emission from each of the Tm:Lu_2O_3 waveguides was monitored using an unbiased photodetector (Thorlabs DET10D, 1.2 – 2 µm) after a filter providing >40 dB of attenuation at the pump wavelength. The fluorescence signal was maximised by tuning the cavity alignment and input coupling of the pump light and a check for a lasing threshold was then undertaken by increasing the pump power. In all the waveguides tested only the structures written with 2 µJ and 3 µJ energy pulses and 30 µm track separation exhibited lasing with the best performance observed from the 2 µJ written structure. No waveguides were written

with pulse energies between 2 – 3 μJ and so further exploration of waveguides written with pulse energies in this region is justified to see if improved performance can be attained.

With the waveguide emitting the highest laser output in the array established, the output power vs input pump power characteristics were measured with the range of output couplers, with a selection of results shown in Figure 6-6. For these measurements two power meters (S310C, Thorlabs) were used to measure the input pump power and emitted signal at the positions shown in Figure 6-5. Using the known losses at the signal wavelength for the optics downstream of the output coupler the output power emitted from the waveguide could be calculated. The absorbed pump power was determined by measuring the residual pump power transmitted through the output coupler with the pump filter removed and the signal power subtracted and using this to estimate a conversion factor to calculate the absorbed power from the input power.

For such conversion from the measured incident power to absorbed, a perfect coupling of the pump signal into the waveguide was assumed except for a single Fresnel reflection due to the uncoated end facets, i.e. no coupling loss due to mode field mismatch between the guided pump mode and the pump spot profile. This assumption gives conservative, and hence higher, values for absorbed pump power due to uncertainties in calculating the coupling loss into the waveguide. A maximum output power of 81 mW was generated using the 40% output coupler for an absorbed power of 1.18 W, as shown in Figure 6-6. In addition, under optimal alignment conditions with the 40% output coupler a maximum slope efficiency of 9.5% was attained. However, a lower output power of 52 mW was generated at such conditions due to the presence of a slight degradation of the pump laser output at the time of achieving this result.

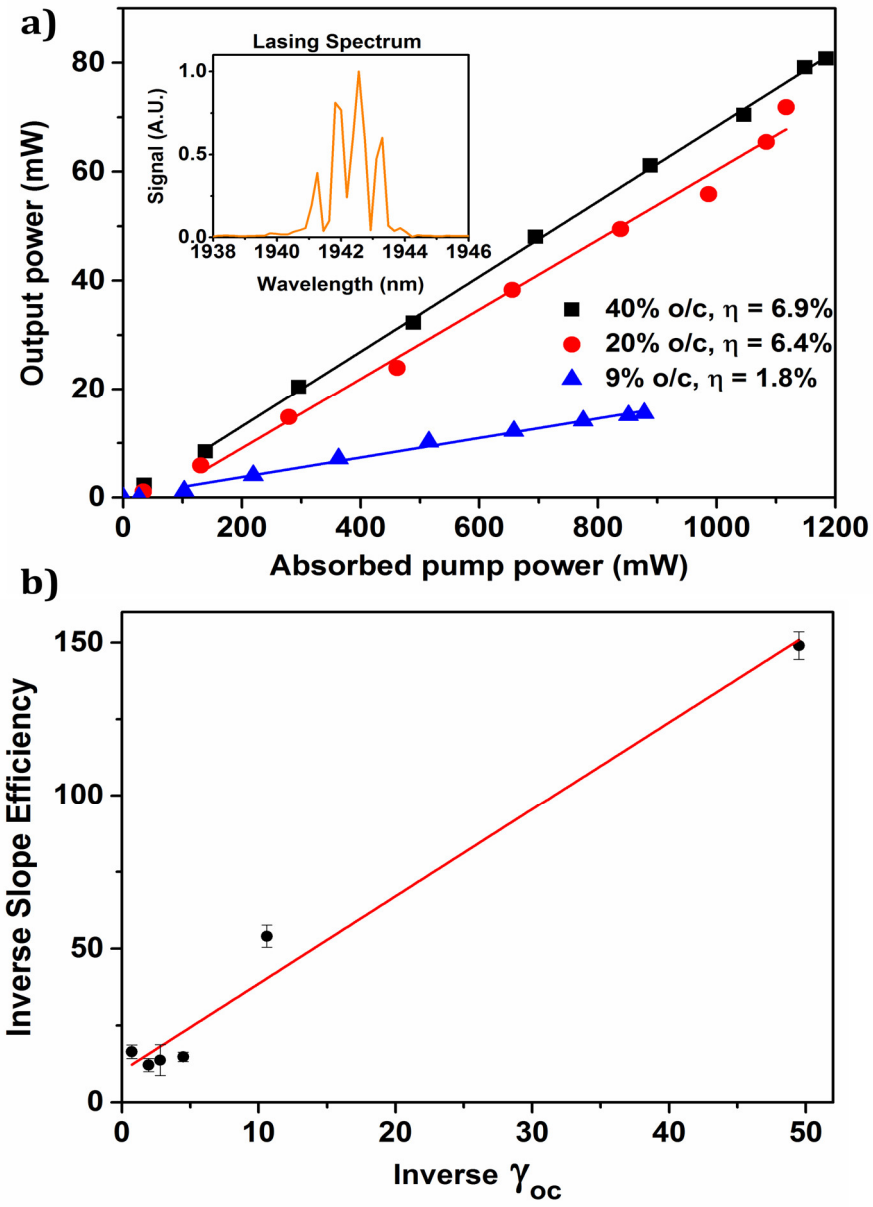

Figure 6-6 *(a) Input-output power characteristics of the Tm:Lu_2O_3 waveguide laser with different output couplers at the maximum output power experimental conditions. The inset shows the laser spectrum. (b) Experimental data and a linear fit of the inverse measured slope efficiencies against inverse output coupling.*

Across the series of output couplers tested, thresholds were observed to be in the range of 50 - 200 mW and the lasing emission spectrum remained centred around 1942 nm as measured using a fibre coupled optical spectrum analyser (Thorlabs OSA205). From the slope efficiencies calculated for each output coupler a modified Caird analysis [183] was performed in order to determine the parasitic round trip loss for the signal wavelength in the cavity, which due to cavity design, we equate to the round trip propagation loss for the waveguide.

The Caird analysis uses the relationship between the measured slope efficiencies and the known output coupling values from equations 6-5 and 6-6 to determine the cavity losses per pass. However, the original application of this method used a simplification valid in the limits of low cavity losses, namely that $\gamma_i \approx L_i$ and $\gamma_{oc} \approx T_{oc}$ for L_i, $T_{oc} \rightarrow 0$. The analysis should be modified to contain logarithmic arguments in the case of large output coupling values and large parasitic cavity losses, which gives:

$$\frac{1}{\eta_s} = \frac{1}{\eta_0}\left(1 + \frac{2\gamma_i}{\gamma_{oc}}\right) \qquad 6\text{-}10$$

where η_0 is the limiting slope efficiency with $\eta_0 = \eta_p\eta_q\eta_t$.

Fitting the above function to the measured slope efficiencies data, Figure 6-6, the propagation losses at the signal wavelength for the lasing waveguide were estimated to be 0.7 dB·cm^{-1} ±0.3 dB·cm^{-1}.

The near field mode profiles of the pump and lasing signals at the output facet of the waveguide were imaged using commercial visible (Thorlabs DCC1545M) and mid-IR cameras (FLIR SC7600M), respectively. The pump mode was imaged directly onto the camera sensor whereas the lasing signal mode was imaged onto a screen through the pump filter, and subsequently viewed with the IR camera. The waveguide structure demonstrated multimode characteristics at the pump wavelength of 796 nm but single mode propagation was observed at the laser wavelength, as shown in Figure 6-7. This behavior indicates that there is not ideal overlap between the pump and signal modes and hence pumping at longer wavelengths (in-band pumping) might provide further improvements to the laser slope efficiency due enhanced mode matching. A Gaussian fit of the lasing mode was performed using a scaled image containing a calibration target, this gave the mode field diameter ($1/e^2$) of signal of 22.5 µm and 25.2 µm in the *x* and *y* directions, respectively as seen in Figure 6-7.

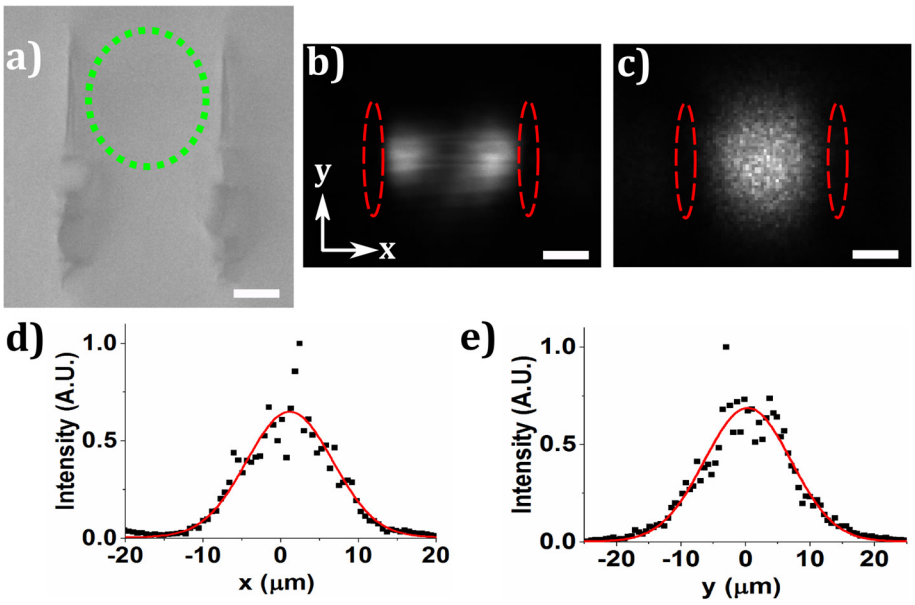

Figure 6-7 *(a) Microscope image of the waveguide used in the laser experiments. (b) and (c) show the pump (796 nm) and the laser (1942 nm) mode images, respectively. 10 μm scale bars are included. The green dotted circle shows the unmodified guiding region. Red dashed ellipses indicate the area of the inscribed tracks. (d) and (e) are the Gaussian fits to slices through the laser mode image in x and y directions, respectively.*

To investigate the waveguide losses at the pump wavelength a modified version of the setup described in Figure 6-5 was used. This involved the removal of the cavity mirrors and pump filter used for laser experiments and a detuning of the Ti:sapphire pump laser to a wavelength of 860 nm where there is a negligible absorption by the Tm:Lu_2O_3 sample. Incident and transmitted power measurements were taken with optimal coupling into the waveguide used in the laser experiments. In addition, a background loss value was taken by measuring the incident and transmitted power for just the lenses used by translating the sample out of the beamline to ensure that no clipping of the pump laser beam had occurred. These results allow for the calculation of the insertion loss for the laser waveguide at the pump wavelength which was estimated to be 1.6 dB. With the insertion loss established at the pump wavelength, measurements of the propagation loss of the waveguide allow for extraction of the coupling efficiency. However, the multimode nature of the waveguide at the pump wavelength inhibits the use of the most prevalent methods for accurate propagation loss measurements and thus the coupling loss could not be accurately determined.

6.5 Summary

This Chapter has presented the first demonstration of ULI channel waveguide fabrication in Tm:Lu_2O_3 ceramic, and the subsequent first demonstration of a ULI channel waveguide sesquioxide laser. The Chapter began with a section on the fundamentals of laser operation which was followed by a discussion of mid-IR emitting ULI waveguide lasers demonstrated to-date and key results from mid-IR bulk laser systems using Tm:Lu_2O_3 crystals or ceramics as their gain media.

The next section gave details on how suitable ULI fabrication parameters were found in order to produce ULI track waveguides in Tm:Lu_2O_3 which was achieved by writing waveguide structures across a range of pulse energies and track separations. The testing of the waveguides for their guiding characteristics is described and a transition from Type I to Type II guiding was observed as pulse energy increased.

A final section presents the properties of ULI fabricated waveguide lasers based on Tm:Lu_2O_3 ceramic with a maximum output power of 81 mW at 1942 nm and a slope efficiency of 9.5% measured. Laser thresholds were observed to be in the range of 50 – 200 mW across the range of output couplers tested and waveguide losses at the emission wavelength were found to be 0.7 dB·cm^{-1} ±0.3 dB·cm^{-1}.

The occurrence of Type I guiding indicates the possibility of ULI waveguide writing in Tm:Lu_2O_3 ceramic using a method optimised for this regime such as multiscan inscribing which has been shown to be a route toward low threshold and high slope efficiency waveguide lasers in other gain media [184]. Furthermore, the writing of depressed cladding waveguide structures in Tm:Lu_2O_3 is also feasible as it has been established for other mid-IR gain media such as those discussed in the earlier section of mid-IR ULI waveguide lasers.

The work in this chapter was published in Optics Express [185] and presented at CLEO Europe 2017 [186].

Chapter 7 Conclusions and Future Work

7.1 Introduction

This thesis has presented research undertaken on the microfabrication of photonic devices for mid-IR optical applications. ULI waveguides in highly nonlinear materials were manufactured, studied and employed for chip scale supercontinuum generation in Chapter 4, which has applications in remote sensing. ULI enabled selective chemical etching of mid-IR transmitting glass was studied in Chapter 5 as a potential route to the production of optofluidic sensors for gas, liquid chemical or biomedical samples. The fabrication and development of a ULI mid-IR waveguide laser source was presented in Chapter 6, demonstrating progress towards compact, low-threshold and efficient laser sources near 2 μm with the potential for high pulse repetition rate ultrafast operation. A custom advanced laser processing setup suitable for ULI fabrication was designed, built and commissioned which is described in Chapter 3 with supporting information provided in Appendix A.

This final Chapter aims to succinctly present the outcomes from this work and suggests areas for further development. The chapter begins with a section presenting conclusions from the research undertaken. This is followed by a section on future work which is split into subsections on specific focussed research paths. The Chapter, and thesis, then concludes with some closing thoughts on ULI and mid-IR photonics.

7.2 Conclusions

The results of the investigations into the microfabrication of photonic devices for mid-IR optical applications have been discussed in Chapters 3 to 6. With each Chapter providing a separate and distinct area of research and/or development.

Chapter 3 described the construction and commissioning of an advanced laser processing system at FCAP which is suitable for ULI. The chapter began with the requirements for a typical ULI experimental setup including techniques employed to modify the shape or cross section of inscribed regions for microchannels and waveguides. Following this was a discussion on the design of the laser processing system at FCAP which builds in adaptability for other laser processing techniques in addition to ULI. Hardware choices,

beamline design and the writing of custom control software to automate the laser processing system was also presented. A final section detailed the initial system outputs, which focussed on ULI glass micro-structuring of fused silica and waveguide writing in GLSSe, indicate the system is performing as expected. The Chapter is supported by **Appendix A** which is a user guide for the ULI processing system at FCAP, providing instructions for system setup, usage and shutdown.

Chapter 4 discussed the first demonstration of ULI fabricated waveguides in GASIR-1, a commercially available chalcogenide glass with high optical quality that transmits light up to ~15 μm. The Chapter began with an overview of chalcogenide glass waveguides designed to operate in the mid-IR with a focus on previous ULI fabricated devices and highlighting the applications for which they are suited. Following this, the results of a study on the response of GASIR-1 to ULI fabrication techniques were discussed. For the parameter space investigated, the response of GASIR-1 was found to be an increased refractive index in the inscribed regions and so Type I multiscan waveguides were fabricated.

The guiding properties of the multiscan waveguides at 2.94 μm in terms of number modes supported, single mode up to core dimensions of 6 by 15 μm; MFDs, circular in the range of 12 to 16 μm; and losses, estimated to be 1.75 dBcm^{-1} ± 0.26 dB cm^{-1}, have also been presented. Nonlinear optical characterisation in the mid-IR using the Z-scan technique determined the nonlinear refractive value of GASIR-1 to be 1×10^{-18} m^2/W ± 15% at 2.5 μm. These initial waveguide and sample characterisation measurements represent the first step in introducing GASIR-1 as a new material for ULI fabricated mid-IR integrated optics and for nonlinear optics applications.

Once such application is mid-IR supercontinuum generation, which was investigated by pumping GASIR-1 ULI waveguides with 120 fs pulses centered at 4.6 μm. When pumping waveguides with cross sections of 8 by 15 μm, a supercontinuum spanning approximately 4 μm from 2.5 to 6.5 μm was measured for pump pulse energies of 130 nJ. This represents the broadest and the deepest IR supercontinuum from a ULI waveguide to date. Dispersion characterisation found the ZDW for this waveguide to be above 4.6 μm and hence the supercontinuum was produced by pumping in the normal dispersion regime.

Chapter 5 presented preliminary work on the FLICE processing of GLS glass with a view to fabrication of mid-IR optofluidic devices. To the best of our knowledge, this work is the first report of selective chemical etching of bulk chalcogenide glasses using the FLICE fabrication technique.

The Chapter began with an introduction to micro and optofluidics along with a discussion of devices fabricated by ULI which have been limited to silicate glasses. An overview of the work by other researchers in wet chemical etching of chalcogenide glass thin films was presented and used to identify suitable etching chemicals. The next section detailed the etching of ULI fabricated micro-channels in GLS using various concentrations of inorganic and organic wet chemical etchants in solution with the results compared with FLICE processing of fused silica micro-channels inscribed using the same inscription setup. For GLS, a maximum etching selectivity of ~13.3 was measured for 1 vol% solutions of HCL in de-ionised water whereas in fused silica a selectivity of ~40 was observed with 5 vol% solutions of HF in de-ionised water. The GLS etching trials also showed that the basic organic and inorganic etchants used to structure chalcogenide thin films have no discernible effect on bulk GLS glass.

The next section discussed the design of an optofluidic sensor which was used for fabrication trials in GLS and fused silica. The design could be successfully inscribed in GLS with no evidence of sample cracking or inducement of defects but etching of the inscribed optofluidic chips lead to the devices failing before the complete etching of the microfluidic components. The most common failure route being over etching of inlet/outlet ports causing sample surface breaching or the etching of sensor waveguides. In contrast, arrays of fused silica devices could be successfully and repeatably fabricated with yields up to 100%.

Chapter 6 detailed the first demonstration of ULI waveguide fabrication and waveguide lasers in Tm:Lu_2O_3 ceramic, a laser gain medium which has been used to produce efficient ultrashort pulsed lasers around 2 μm in bulk systems.

The Chapter began with a section on the fundamentals of laser operation which was followed by a discussion of mid-IR emitting ULI waveguide lasers demonstrated to-date and key results from mid-IR bulk laser systems using Tm:Lu_2O_3 crystals or ceramics as

their gain media. The next section gave details on how suitable ULI fabrication parameters were found in order to produce ULI track waveguides in Tm:Lu_2O_3 which was achieved by writing waveguide structures across a range of pulse energies, from 0.4 to 5 μJ, and track separations of 20 or 30 μm. The testing of the waveguides for their guiding characteristics found a transition from Type I to Type II guiding for pulse energies around 0.9 μJ.

A final section presented the properties of ULI fabricated waveguide lasers based on Tm:Lu_2O_3 ceramic which displayed a maximum CW output power of 81 mW at 1942 nm with a slope efficiency of 9.5%. This result was attained with a 40% transmitting output coupler mirror as part of a systematic search for the optimal cavity output coupling. Laser thresholds were observed to be in the range of 50 – 200 mW across the set of output couplers tested and waveguide losses at the emission wavelength were found to be 0.7 $dB \cdot cm^{-1}$ ±0.3 $dB \cdot cm^{-1}$ through a modified Caird analysis.

7.3 Future Work

Based on the reported outcomes from Chapters 4-6 there are clear routes for future work that the author envisions could follow on from the investigations carried out in this thesis, which will now be outlined.

7.3.1 Multi-octave Spanning ULI Waveguide Supercontinuum Sources

Whilst GASIR-1 ULI waveguides in Chapter 4 were shown to produce the broadest and deepest IR supercontinuum from a ULI fabricated waveguide to-date, results from Ge-As-Se thin film waveguides, particularly reports of 2 – 10 μm supercontinuum generation from buried thin film $Ge_{11.5}As_{24}Se_{64.5}$ channel waveguides [123], show that there is great potential for improving this result. This could be investigated through complementary strands of experimental and theoretical work.

For the theoretical work, simulations of ULI waveguide structures to optimise their dispersive properties could provide a new route to increasing the breadth of the output supercontinuum from ULI waveguides in nonlinear materials through exploration of dispersion flattening, to restrict the temporal walk-off of the broadened pump light and hence maintain the spatial overlap required for nonlinear frequency generation processes,

or dispersion shifted designs that are optimised for specific pump sources. Furthermore, study of the simple step index multiscan waveguides already employed would be useful in determining an optimal waveguide length for broadening by modelling the spectral evolution of the supercontinuum process as a function of propagation distance along the waveguide.

For the experimental work, there are potential improvements to be made by further optimisation of step index multiscan waveguides for low-loss broad bandwidth guiding. As supercontinuum generation is a nonlinear process the reduction of the propagation losses of inscribed waveguides in GASIR-1 would be expected to lead to broader output supercontinuum. As the results in Chapter 4 show that the largest core waveguide produced the widest supercontinuum, which was attributed to higher efficiency coupling of the pump light and tighter mode confinement of longer IR wavelengths, repeating the reported experiments with larger core waveguides in GASIR-1 would be a worthwhile endeavour. As would finding a suitable pump source and experimental setup that could allow pumping of large core GASIR-1 waveguides in the anomalous dispersion regime.

7.3.2 Broadband Mid-IR Optofluidic Sensors

The successful fabrication of optofluidic sensor chips in fused silica shown in Chapter 5, indicates that a modest improvement in etching selectivity of GLS, by around a factor of 4, would be the final step in realising the FLICE fabrication mid-IR optofluidic devices in chalcogenide glasses.

Based on the body of work on selective chemical etching of ULI processed fused silica and the selective chemical etching of photopolymerised chalcogenide thin-films there are two routes that could be explored. Firstly, as the high selectivity of fused silica glass is attributed to the formation of sub focal region nanocracks enabling the rapid ingress of etching solutions along the inscribed micro-structures [71], a laser parameter study for nanocrack formation in GLS could provide the required increase in modified region etch rate.

Secondly, studies on FLICE processing of fused silica with aqueous KOH solutions, demonstrating an order of magnitude improvement on the reported etching selectivity of aqueous HF solutions [31], and also on high selective etching of chalcogenide films with

specially synthesised aryl amine etchants [168], highlights the importance of the etching chemical in determining the ratio of modified to unmodified material etch rates. A cross-disciplinary project incorporating thorough chemical analysis to understand the origins of the etching selectivity of ULI modified GLS in HCL solutions could lead to new etching chemicals tailored for high selectivity.

Once a suitable etching selectivity is attained, the on-chip broadband sensing of microfluidic samples could be attained by using the device design proposed in Chapter 5 with a swept source. A variation on the proposed design would enable single shot broadband sensing by using input waveguides optimised for supercontinuum generation in GLS [110], and a large mode area collection waveguide, either multimode or of the single mode array type discussed in Chapter 4 [116], to collect the transmitted signal without further broadening distorting the measurement.

7.3.3 Novel Mid-IR Sesquioxide ULI Waveguide Lasers

The occurrence of both type I and type II guiding in Tm:Lu_2O_3 opens up the possibility of realising a number of different ULI waveguide laser designs in the same gain media. One such example would be using a method optimised for Type I waveguide writing, such as multiscan method, to produce the first, to the best of our knowledge, demonstration of a mid-IR type I ULI waveguide laser. This class of waveguide laser has been has shown to be a route toward high slope efficiency waveguide lasers in the near-IR in other gain media [184]. If the magnitude of the induced refractive index change in the type I regime is greater than the magnitude of index change achievable in the type II regime, a lower lasing threshold could be realized by tighter mode confinement opening up the potential for single mode fibre coupled diode pumping.

A second example would be the writing of depressed cladding waveguide structures in Tm:Lu_2O_3 as this structure has produced the highest slope efficiency ULI waveguide lasers reported thus-far in the mid-IR [187]. Also, the radial symmetry of a depressed cladding structure typically leads to polarisation independent guiding, in contrast to the distinct polarisation dependence reported from the track waveguides in Chapter 6, this could lead to simpler and more compact pumping schemes if polarisation control is not required.

Finally, a combination of the two inscription regimes is envisioned where a depressed cladding waveguide is inscribed with an axial type I Bragg grating structure. A similar design has been implemented as a Bragg waveguide filter in ZBLAN [98]. In Tm:Lu_2O_3, which can provide optical gain, such a structure could provide the spectral narrowing required for single frequency output. Furthermore, a strong Bragg resonance from a long grating structure inscribed along the entire length of a depressed cladding waveguide would remove the need for laser cavity optics completely if the feedback provided is enough for the waveguide laser to reach threshold, analogous to distributed feedback diode lasers. If realised, both of these designs would vastly reduce the SWaP requirements of singe frequency solid state lasers.

As well as investigations of new ULI waveguide designs in sesquioxide host materials, one further area of future research for mid-IR ULI waveguide lasers would be the exploration of waveguide writing and lasing of Er:Lu_2O_3 for deeper IR emission. This is supported by demonstrations of 796 nm diode pumped bulk solid-state Er:Lu_2O_3 lasers with up to 5.9 W of output power at 27% of slope efficiency at 2.85 μm [89], showing the potential of this gain media for high power and efficient ULI waveguide lasers near 3 μm. In ULI waveguide lasers, this spectral region is currently only covered by Cr:ZnSe waveguide lasers which rely on thulium fibre laser pump sources. An Er:Lu_2O_3 waveguide laser could be directly diode pumped potentially leading to greater wall-plug efficiency and more compact systems.

7.4 Closing remarks

The range of applications and materials discussed in this thesis is testament to both the versatility and unique capabilities of ULI, and the utility of mid-IR photonics. The successful commercialisation of ULI techniques along with the ever-expanding range of commercially available mid-IR photonic systems and components show that these fields continue to be worth-while endeavours that can offer value to researchers, by providing exciting new science; and to businesses, by providing new products or services. I look forward to following and perhaps even playing a part in the future development of both.

References

[1] M. Guarnieri, "Two Millennia of Light: The Long Path to Maxwell's Waves " IEEE Industrial Electronics Magazine **9**, 54-60 (2015).

[2] B. E. A. Saleh and M. C. Teich, *Fundamentals of Photonics* (Wiley, 2013).

[3] J. Dudley, J. González, J. Niemela, and K. Plenkovich, "The International Year of Light and Light-based Technologies 2015 Final Report," (United Nations Educational, Scientific and Cultural Organization (UNESCO), 2016).

[4] T. H. Maiman, "Stimulated Optical Radiation in Ruby," Nature **187**, 493-494 (1960).

[5] R. N. Hall, R. O. Carlson, T. J. Soltys, G. E. Fenner, and J. D. Kingsley, "Coherent Light Emission from Gaas Junctions," Physical Review Letters **9**, 366-& (1962).

[6] M. I. Nathan, W. P. Dumke, G. Burns, F. H. Dill, and G. Lasher, "Stimulated Emission of Radiation from GaAs p-n Junctions," Applied Physics Letters **1**, 62-64 (1962).

[7] R. J. Mears, L. Reekie, I. M. Jauncey, and D. N. Payne, "Low-noise erbium-doped fibre amplifier operating at 1.54μm," Electronics Letters **23**, 1026 (1987).

[8] E. Desurvire, J. R. Simpson, and P. C. Becker, "High-gain erbium-doped traveling-wave fiber amplifier," Optics Letters **12**, 888-890 (1987).

[9] Coblentz-Society, "Evaluated Infrared Reference Spectra," in *NIST Chemistry WebBook, NIST Standard Reference Database Number 69*, P. J. Linstrom and W. G. Mallard, eds. (National Institute of Standards and Technology, 1988).

[10] S. D. Lord, "A new software tool for computing Earth's atmospheric transmission of near-and far-infrared radiation," (NASA Technical Memorandum 103957, 1992).

[11] R. L. McCally, J. Bonney-Ray, Z. de la Cruz, and W. R. Green, "Corneal endothelial injury thresholds for exposures to 1.54 μm radiation," Health physics **92**, 205-211 (2007).

[12] R. Kaufmann and R. Hibst, "Pulsed 2.94 μm erbium-YAG laser skin ablation-experimental results and first clinical application," Clinical and Experimental Dermatology **15**, 389-393 (1990).

[13] O. Svelto, *Principles of Lasers* (Springer, 2010).

[14] S. A. McDaniel, A. Lancaster, J. W. Evans, A. K. Kar, and G. Cook, "Power scaling of ultrafast laser inscribed waveguide lasers in chromium and iron doped zinc selenide," Optics Express **24**, 3502-3512 (2016).

[15] G. P. Agrawal, *Nonlinear fiber optics* (Academic press, 2007).

[16] J. Faist, F. Capasso, D. L. Sivco, C. Sirtori, A. L. Hutchinson, and A. Y. Cho, "Quantum cascade laser," Science **264**, 553-556 (1994).

[17] R. Ostendorf, L. Butschek, S. Hugger, F. Fuchs, Q. Yang, J. Jarvis, C. Schilling, M. Rattunde, A. Merten, J. Grahmann, D. Boskovic, T. Tybussek, K. Rieblinger, and J. Wagner, "Recent Advances and Applications of External Cavity-QCLs towards Hyperspectral Imaging for Standoff Detection and Real-Time Spectroscopic Sensing of Chemicals," Photonics **3**, 28 (2016).

[18] G. Tao, H. Ebendorff-Heidepriem, A. M. Stolyarov, S. Danto, J. V. Badding, Y. Fink, J. Ballato, and A. F. Abouraddy, "Infrared fibers," Advances in Optics and Photonics **7**, 379 (2015).

[19] J. R. Sparks, R. He, N. Healy, M. Krishnamurthi, A. C. Peacock, P. J. Sazio, V. Gopalan, and J. V. Badding, "Zinc selenide optical fibers," Advanced Materials **23**, 1647-1651 (2011).

[20] R. He, P. J. A. Sazio, A. C. Peacock, N. Healy, J. R. Sparks, M. Krishnamurthi, V. Gopalan, and J. V. Badding, "Integration of gigahertz-bandwidth semiconductor devices inside microstructured optical fibres," Nature Photonics **6**, 174 (2012).

[21] R. R. Gattass, R. Thapa, F. H. Kung, L. E. Busse, L. B. Shaw, and J. S. Sanghera, "Review of infrared fiber-based components," Applied Optics **54**, F25-34 (2015).

[22] T. Schadle and B. Mizaikoff, "Mid-Infrared Waveguides: A Perspective," Applied Spectroscopy **70**, 1625-1638 (2016).

[23] Z. G. Lian, W. Pan, D. Furniss, T. M. Benson, A. B. Seddon, T. Kohoutek, J. Orava, and T. Wagner, "Embossing of chalcogenide glasses: monomode rib optical waveguides in evaporated thin films," Optics Letters **34**, 1234-1236 (2009).

[24] C. Tsay, Y. Zha, and C. B. Arnold, "Solution-processed chalcogenide glass for integrated single-mode mid-infrared waveguides," Optics Express **18**, 26744-26753 (2010).

[25] T. Hu, B. W. Dong, X. S. Luo, T. Y. Liow, J. F. Song, C. Lee, and G. Q. Lo, "Silicon photonic platforms for mid-infrared applications [Invited]," Photonics Research **5**, 417-430 (2017).

[26] V. Mittal, A. Aghajani, L. G. Carpenter, J. C. Gates, J. Butement, P. G. Smith, J. S. Wilkinson, and G. S. Murugan, "Fabrication and characterization of high-contrast mid-infrared $GeTe_4$ channel waveguides," Optics Letters **40**, 2016-2019 (2015).

[27] D. Choudhury, W. T. Ramsay, R. Kiss, N. A. Willoughby, L. Paterson, and A. K. Kar, "A 3D mammalian cell separator biochip," Lab Chip **12**, 948-953 (2012).

[28] P. Mitchell, G. Brown, R. R. Thomson, N. Psaila, and A. Kar, "57 Channel (19x3) Spatial Multiplexer Fabricated using Direct Laser Inscription," in *Optical Fiber Communication Conference*, OSA Technical Digest (online) (Optical Society of America, 2014), M3K.5.

[29] T. A. Birks, I. Gris-Sánchez, S. Yerolatsitis, S. G. Leon-Saval, and R. R. Thomson, "The photonic lantern," Advances in Optics and Photonics **7**, 107 (2015).

[30] B. Guan, R. P. Scott, C. Qin, N. K. Fontaine, T. Su, C. Ferrari, M. Cappuzzo, F. Klemens, B. Keller, M. Earnshaw, and S. J. Yoo, "Free-space coherent optical communication with orbital angular, momentum multiplexing/demultiplexing using a hybrid 3D photonic integrated circuit," Optics Express **22**, 145-156 (2014).

[31] J. Gottmann, M. Hermans, N. Repiev, and J. Ortmann, "Selective Laser-Induced Etching of 3D Precision Quartz Glass Components for Microfluidic Applications-Up-Scaling of Complexity and Speed," Micromachines **8**, 110 (2017).

[32] L. A. Fernandes, J. R. Grenier, J. S. Aitchison, and P. R. Herman, "Fiber optic stress-independent helical torsion sensor," Optics Letters **40**, 657-660 (2015).

[33] F. Xia, M. Rooks, L. Sekaric, and Y. Vlasov, "Ultra-compact high order ring resonator filters using submicron silicon photonic wires for on-chip optical interconnects," Optics Express **15**, 11934 (2007).

[34] K. Richardson, D. Krol, and K. Hirao, "Glasses for Photonic Applications," International Journal of Applied Glass Science **1**, 74-86 (2010).

[35] H. Hauser, *The Current and Future Role of Technology and Innovation Centres in the UK: A Report* (Department for Business Innovation and Skills, 2010).

[36] E. Hecht, "Optics, 4th," International edition, Addison-Wesley, San Francisco (2002).

[37] R. W. Boyd, *Nonlinear optics* (Academic press, 2003).

[38] R. G. Hunsperger, "Integrated Optics," Integrated Optics: Theory and Technology, ISBN 978-0-387-89774-5. Springer-Verlag New York, 2009 (2009).

[39] P. A. Franken, G. Weinreich, C. W. Peters, and A. E. Hill, "Generation of Optical Harmonics," Physical Review Letters **7**, 118-& (1961).

[40] P. E. Powers, T. J. Kulp, and S. E. Bisson, "Continuous tuning of a continuous-wave periodically poled lithium niobate optical parametric oscillator by use of a fan-out grating design," Optics Letters **23**, 159-161 (1998).

[41] R. R. Alfano, *The Supercontinuum Laser Source: The Ultimate White Light,* 3rd ed. ed. (Springer, New York, 2016).

[42] L. F. Mollenauer, R. H. Stolen, and J. P. Gordon, "Experimental Observation of Picosecond Pulse Narrowing and Solitons in Optical Fibers," Physical Review Letters **45**, 1095-1098 (1980).

[43] J. Dudley and R. Taylor, *Supercontinuum generation in optical fibers* (Cambridge University Press, 2010).

[44] A. Heidt, "Efficient Adaptive Step Size Method for the Simulation of Supercontinuum Generation in Optical Fibers," Journal of Lightwave Technology **27**, 3984-3991 (2009).

[45] D. Swinehart, "The beer-lambert law," Journal of chemical education **39**, 333 (1962).

[46] M. Bass, C. DeCusatis, J. M. Enoch, V. Lakshminarayanan, G. Li, C. MacDonald, V. N. Mahajan, and E. Van Stryland, *Handbook of Optics, Second Edition Volume IV: Fiber Optics & Nonlinear Optics* (McGraw-Hill 2009).

[47] L. Keldysh, "Ionization in the field of a strong electromagnetic wave," Soviet Physics JETP **20**, 1307-1314 (1965).

[48] M. Ams, G. D. Marshall, P. Dekker, M. Dubov, V. K. Mezentsev, I. Bennion, and M. J. Withford, "Investigation of Ultrafast Laser-Photonic Material Interactions: Challenges for Directly Written Glass Photonics," IEEE Journal of Selected Topics in Quantum Electronics **14**, 1370-1381 (2008).

[49] R. R. Gattass and E. Mazur, "Femtosecond laser micromachining in transparent materials," Nature Photonics **2**, 219-225 (2008).

[50] C. B. Schaffer, "Interaction of femtosecond laser pulses with transparent materials," (Harvard University, 2001).

[51] M. Beresna, M. Gecevicius, and P. G. Kazansky, "Ultrafast laser direct writing and nanostructuring in transparent materials," Advances in Optics and Photonics **6**, 293-339 (2014).

[52] G. Smith, K. Kalli, and K. Sugden, "Advances in Femtosecond Micromachining and Inscription of Micro and Nano Photonic Devices," in *Frontiers in Guided Wave Optics and Optoelectronics* (IntechOpen, 2010).

[53] A. C. Tien, S. Backus, H. Kapteyn, M. Murnane, and G. Mourou, "Short-pulse laser damage in transparent materials as a function of pulse duration," Physical Review Letters **82**, 3883-3886 (1999).

[54] J. Lapointe, M. Gagné, M.-J. Li, and R. Kashyap, "Making smart phones smarter with photonics," Optics Express **22**, 15473 (2014).

[55] J. Hu and C. R. Menyuk, "Understanding leaky modes: slab waveguide revisited," Advances in Optics and Photonics **1**, 58-106 (2009).

[56] K. Hirao and K. Miura, "Writing waveguides and gratings in silica and related materials by a femtosecond laser," Journal of Non-Crystalline Solids **239**, 91-95 (1998).

[57] A. Saliminia, R. Vallée, and S. L. Chin, "Waveguide writing in silica glass with femtosecond pulses from an optical parametric amplifier at 1.5μm," Optics Communications **256**, 422-427 (2005).

[58] J. W. Chan, T. Huser, S. Risbud, and D. M. Krol, "Structural changes in fused silica after exposure to focused femtosecond laser pulses," Optics Letters **26**, 1726-1728 (2001).

[59] S. Kanehira, K. Miura, and K. Hirao, "Ion exchange in glass using femtosecond laser irradiation," Applied Physics Letters **93**, 023112 (2008).

[60] A. Rodenas, A. Benayas, J. R. Macdonald, J. Zhang, D. Y. Tang, D. Jaque, and A. K. Kar, "Direct laser writing of near-IR step-index buried channel waveguides in rare earth doped YAG," Optics Letters **36**, 3395-3397 (2011).

[61] C. Grivas, C. Corbari, G. Brambilla, and P. G. Lagoudakis, "Tunable, continuous-wave Ti:sapphire channel waveguide lasers written by femtosecond and picosecond laser pulses," Optics Letters **37**, 4630-4632 (2012).

[62] D. Choudhury, J. R. Macdonald, and A. K. Kar, "Ultrafast laser inscription: perspectives on future integrated applications," Laser & Photonics Reviews **8**, 827-846 (2014).

[63] R. Osellame, G. Cerullo, and R. Ramponi, *Femtosecond Laser Micromachining: Photonic and Microfluidic Devices in Transparent Materials*, Topics in Applied Physics (Springer, 2012), Vol. 123.

[64] S. Juodkazis, K. Nishimura, H. Misawa, T. Ebisui, R. Waki, S. Matsuo, and T. Okada, "Control over the crystalline state of sapphire," Advanced Materials **18**, 1361–1364 (2006).

[65] D. Choudhury, A. Rodenas, L. Paterson, F. Diaz, D. Jaque, and A. K. Kar, "Three-dimensional microstructuring of yttrium aluminum garnet crystals for laser active optofluidic applications," Applied Physics Letters **103**(2013).

[66] R. Taylor, C. Hnatovsky, E. Simova, D. Rayner, M. Mehandale, V. Bhardwaj, and P. Corkum, "Ultra-high resolution index of refraction profiles of femtosecond laser modified silica structures," Optics Express **11**, 775-781 (2003).

[67] Y. Shimotsuma, P. G. Kazansky, J. Qiu, and K. Hirao, "Self-organized nanogratings in glass irradiated by ultrashort light pulses," Physical Review Letters **91**, 247405 (2003).

[68] P. P. Rajeev, M. Gertsvolf, E. Simova, C. Hnatovsky, R. S. Taylor, V. R. Bhardwaj, D. M. Rayner, and P. B. Corkum, "Memory in nonlinear ionization of transparent solids," Physical Review Letters **97**, 253001 (2006).

[69] S. Richter, C. Miese, S. Döring, F. Zimmermann, M. J. Withford, A. Tünnermann, and S. Nolte, "Laser induced nanogratings beyond fused silica - periodic nanostructures in borosilicate glasses and ULE™," Optical Materials Express **3**, 1161 (2013).

[70] Y. Shimotsuma, K. Hirao, J. R. Qiu, and K. Miura, "Nanofabrication in transparent materials with a femtosecond pulse laser," Journal of Non-Crystalline Solids **352**, 646-656 (2006).

[71] R. Taylor, C. Hnatovsky, and E. Simova, "Applications of femtosecond laser induced self-organized planar nanocracks inside fused silica glass," Laser & Photonics Reviews **2**, 26-46 (2008).

[72] D. W. Hewak, "Chalcogenide glasses for photonics device applications," in *Photonic glasses and glass-ceramics*, G. S. Murugan, ed. (Research Signpost, 2010).

[73] B. J. Eggleton, B. Luther-Davies, and K. Richardson, "Chalcogenide photonics," Nature Photonics **5**, 141-148 (2011).

[74] M. Yamane and Y. Asahara, *Glasses for photonics* (Cambridge University Press, 2000).

[75] G. Lenz, J. Zimmermann, T. Katsufuji, M. E. Lines, H. Y. Hwang, S. Spalter, R. E. Slusher, S. W. Cheong, J. S. Sanghera, and I. D. Aggarwal, "Large Kerr effect in bulk Se-based chalcogenide glasses," Optics Letters **25**, 254-256 (2000).

[76] J.-L. Adam and X. Zhang, *Chalcogenide Glasses: Preparation, Properties and Applications* (Woodhead Publishing, 2014).

[77] F. Smektala, C. Quemard, V. Couderc, and A. Barthelemy, "Non-linear optical properties of chalcogenide glasses measured by Z-scan," Journal of Non-Crystalline Solids **274**, 232-237 (2000).

[78] J. Requejo-Isidro, A. K. Mairaj, V. Pruneri, D. W. Hewak, M. C. Netti, and J. J. Baumberg, "Self refractive non-linearities in chalcogenide based glasses," Journal of Non-Crystalline Solids **317**, 241-246 (2003).

[79] A. Zakery and S. R. Elliott, "Optical properties and applications of chalcogenide glasses: a review," Journal of Non-Crystalline Solids **330**, 1-12 (2003).

[80] V. Lyubin, "Chalcogenide glassy photoresists: History of development, properties, and applications," Physica Status Solidi B-Basic Solid State Physics **246**, 1758-1767 (2009).

[81] A. K. Mairaj, H. Ping, H. N. Rutt, and D. W. Hewak, "Fabrication and characterization of continuous wave direct UV (λ=244 nm) written channel waveguides in chalcogenide (Ga:La:S) glass," Journal of Lightwave Technology **20**, 1578-1584 (2002).

[82] A. A. Lagatsky, O. L. Antipov, and W. Sibbett, "Broadly tunable femtosecond Tm:Lu_2O_3 ceramic laser operating around 2070 nm," Optics Express **20**, 19349-19354 (2012).

[83] P. Koopmann, S. Lamrini, K. Scholle, P. Fuhrberg, K. Petermann, and G. Huber, "Efficient diode-pumped laser operation of Tm:Lu_2O_3 around 2 μm," Optics Letters **36**, 948-950 (2011).

[84] M. J. Weber, *Handbook of optical materials*, Laser and Optical Science and Technology Series (CRC press, 2002), Vol. 19.

[85] D. E. Zelmon, J. M. Northridge, N. D. Haynes, D. Perlov, and K. Petermann, "Temperature-dependent Sellmeier equations for rare-earth sesquioxides," Applied Optics **52**, 3824-3828 (2013).

[86] R. Peters, "Ytterbium-dotierte Sesquioxide als hocheffiziente Lasermaterialien," (University of Hamburg, 2009).

[87] E. Mix, "Kristallzüchtung, Spektroskopie und Lasereigenschaften Yb-dotierter Sesquioxide," (University of Hamburg, 1999).

[88] P. Koopmann, "Thulium- and Holmium-doped Sesquioxides for 2 μm Lasers," (University of Hamburg, 2012).

[89] C. Krankel, "Rare-Earth-Doped Sesquioxides for Diode-Pumped High-Power Lasers in the 1-, 2-, and 3- μm Spectral Range," IEEE Journal of Selected Topics in Quantum Electronics **21**, 250-262 (2015).

[90] J. Sanghera, W. Kim, G. Villalobos, B. Shaw, C. Baker, J. Frantz, B. Sadowski, and I. Aggarwal, "Ceramic Laser Materials," Materials **5**, 258-277 (2012).

[91] R. Peters, C. Kränkel, S. T. Fredrich-Thornton, K. Beil, K. Petermann, G. Huber, O. H. Heckl, C. R. E. Baer, C. J. Saraceno, T. Südmeyer, and U. Keller, "Thermal analysis and efficient high power continuous-wave and mode-locked thin disk laser operation of Yb-doped sesquioxides," Applied Physics B **102**, 509-514 (2011).

[92] V. Peters, "Growth and spectroscopy of ytterbium doped sesquioxides," (University of Hamburg, 2001).

[93] K. Petermann, G. Huber, L. Fornasiero, S. Kuch, E. Mix, V. Peters, and S. A. Basun, "Rare-earth-doped sesquioxides," Journal of Luminescence **87-89**, 973-975 (2000).

[94] E. V. Ivakin, I. G. Kisialiou, and O. L. Antipov, "Laser ceramics Tm:Lu_2O_3. Thermal, thermo-optical, and spectroscopic properties," Optical Materials **35**, 499-503 (2013).

[95] A. Ikesue, Y. L. Aung, T. Taira, T. Kamimura, K. Yoshida, and G. L. Messing, "Progress in ceramic lasers," Annual Review of Materials Research **36**, 397-429 (2006).

[96] A. Ikesue and Y. L. Aung, "Synthesis and performance of advanced ceramic lasers," Journal of the American Ceramic Society **89**, 1936-1944 (2006).

[97] O. L. Antipov, A. A. Novikov, N. G. Zakharov, and A. P. Zinoviev, "Optical properties and efficient laser oscillation at 2066 nm of novel Tm:Lu_2O_3 ceramics," Optical Materials Express **2**, 183-189 (2012).

[98] S. Gross, M. Ams, D. G. Lancaster, T. M. Monro, A. Fuerbach, and M. J. Withford, "Femtosecond direct-write uberstructure waveguide Bragg gratings in ZBLAN," Optics Letters **37**, 3999-4001 (2012).

[99] R. Thomson, C. Leburn, and D. T. Reid, *Ultrafast Nonlinear Optics*, Scottish Graduate Series (Springer International Publishing, 2013).

[100] A. Marcinkevicius, V. Mizeikis, S. Juodkazis, S. Matsuo, and H. Misawa, "Effect of refractive index-mismatch on laser microfabrication in silica glass," Applied Physics A - Materials Science & Processing **76**, 257-260 (2003).

[101] C. Hnatovsky, R. S. Taylor, E. Simova, V. R. Bhardwaj, D. M. Rayner, and P. B. Corkum, "High-resolution study of photoinduced modification in fused silica produced by a tightly focused femtosecond laser beam in the presence of aberrations," Journal of Applied Physics **98**, 013517 (2005).

[102] R. D. Simmonds, P. S. Salter, A. Jesacher, and M. J. Booth, "Three dimensional laser microfabrication in diamond using a dual adaptive optics system," Optics Express **19**, 24122-24128 (2011).

[103] O. Caulier, D. Le Coq, L. Calvez, E. Bychkov, and P. Masselin, "Free carrier accumulation during direct laser writing in chalcogenide glass by light filamentation," Optics Express **19**, 20088-20096 (2011).

[104] R. R. Thomson, H. T. Bookey, N. D. Psaila, A. Fender, S. Campbell, W. N. Macpherson, J. S. Barton, D. T. Reid, and A. K. Kar, "Ultrafast-laser inscription of a three dimensional fan-out device for multicore fiber coupling applications," Optics Express **15**, 11691-11697 (2007).

[105] R. Osellame, S. Taccheo, M. Marangoni, R. Ramponi, P. Laporta, D. Polli, S. De Silvestri, and G. Cerullo, "Femtosecond writing of active optical waveguides with astigmatically shaped beams," Journal of the Optical Society of America B - Optical Physics **20**, 1559-1567 (2003).

[106] M. Ams, G. Marshall, D. Spence, and M. Withford, "Slit beam shaping method for femtosecond laser direct-write fabrication of symmetric waveguides in bulk glasses," Optics Express **13**, 5676-5681 (2005).

[107] Y. Cheng, K. Sugioka, K. Midorikawa, M. Masuda, K. Toyoda, M. Kawachi, and K. Shihoyama, "Control of the cross-sectional shape of a hollow microchannel embedded in photostructurable glass by use of a femtosecond laser," Optics Letters **28**, 55-57 (2003).

[108] R. R. Thomson, A. S. Bockelt, E. Ramsay, S. Beecher, A. H. Greenaway, A. K. Kar, and D. T. Reid, "Shaping ultrafast laser inscribed optical waveguides using a deformable mirror," Optics Express **16**, 12786-12793 (2008).

[109] P. S. Salter, A. Jesacher, J. B. Spring, B. J. Metcalf, N. Thomas-Peter, R. D. Simmonds, N. K. Langford, I. A. Walmsley, and M. J. Booth, "Adaptive slit beam shaping for direct laser written waveguides," Optics Letters **37**, 470-472 (2012).

[110] J. McCarthy, H. Bookey, S. Beecher, R. Lamb, I. Elder, and A. K. Kar, "Spectrally tailored mid-infrared super-continuum generation in a buried waveguide spanning 1750 nm to 5000 nm for atmospheric transmission," Applied Physics Letters **103**, 151103 (2013).

[111] R. Mary, D. Choudhury, and A. K. Kar, "Applications of Fiber Lasers for the Development of Compact Photonic Devices," IEEE Journal of Selected Topics in Quantum Electronics **20**, 72-84 (2014).

[112] M. D. Mackenzie, J. M. Morris, C. R. Petersen, H. T. Bookey, O. Bang, and A. K. Kar, "GLS and GLSSe Ultrafast Laser Inscribed Waveguides for Mid-IR Supercontinuum Generation," Optical Materials Express (Under Preparation).

[113] A. Arriola, S. Gross, M. Ams, T. Gretzinger, D. Le Coq, R. P. Wang, H. Ebendorff-Heidepriem, J. Sanghera, S. Bayya, L. B. Shaw, M. Ireland, P. Tuthill, and M. J. Withford, "Mid-infrared astrophotonics: study of ultrafast laser induced index change in compatible materials," Optical Materials Express **7**, 698 (2017).

[114] G. Demetriou, D. W. Hewak, A. Ravagli, C. Craig, and A. Kar, "Nonlinear refractive index of ultrafast laser inscribed waveguides in gallium lanthanum sulphide," Applied Optics **56**, 5407-5411 (2017).

[115] T. Han, S. Madden, S. Debbarma, and B. Luther-Davies, "Improved method for hot embossing As_2S_3 waveguides employing a thermally stable chalcogenide coating," Optics Express **19**, 25447-25453 (2011).

[116] C. D'Amico, G. Cheng, C. Mauclair, J. Troles, L. Calvez, V. Nazabal, C. Caillaud, G. Martin, B. Arezki, E. LeCoarer, P. Kern, and R. Stoian, "Large-mode-area infrared guiding in ultrafast laser written waveguides in sulfur-based chalcogenide glasses," Optics Express **22**, 13091-13101 (2014).

[117] A. Arriola, S. Mukherjee, D. Choudhury, L. Labadie, and R. R. Thomson, "Ultrafast laser inscription of mid-IR directional couplers for stellar interferometry," Optics Letters **39**, 4820-4822 (2014).

[118] A. Rodenas, G. Martin, B. Arezki, N. Psaila, G. Jose, A. Jha, L. Labadie, P. Kern, A. Kar, and R. Thomson, "Three-dimensional mid-infrared photonic circuits in chalcogenide glass," Optics Letters **37**, 392-394 (2012).

[119] J. E. McCarthy, H. T. Bookey, N. D. Psaila, R. R. Thomson, and A. K. Kar, "Mid-infrared spectral broadening in an ultrafast laser inscribed gallium lanthanum sulphide waveguide," Optics Express **20**, 1545-1551 (2012).

[120] M. R. Karim, B. M. Rahman, and G. P. Agrawal, "Mid-infrared supercontinuum generation using dispersion-engineered $Ge_{11.5}As_{24}Se_{64.5}$ chalcogenide channel waveguide," Optics Express **23**, 6903-6914 (2015).

[121] M. R. Karim and B. M. A. Rahman, "Ultra-broadband mid-infrared supercontinuum generation using chalcogenide rib waveguide," Optical and Quantum Electronics **48**, 174 (2016).

[122] Y. Yu, X. Gai, P. Ma, D. Y. Choi, Z. Y. Yang, R. P. Wang, S. Debbarma, S. J. Madden, and B. Luther-Davies, "A broadband, quasi-continuous, mid-infrared supercontinuum generated in a chalcogenide glass waveguide," Laser & Photonics Reviews **8**, 792-798 (2014).

[123] Y. Yu, X. Gai, P. Ma, K. Vu, Z. Yang, R. Wang, D. Y. Choi, S. Madden, and B. Luther-Davies, "Experimental demonstration of linearly polarized 2-10 μm supercontinuum generation in a chalcogenide rib waveguide," Optics Letters **41**, 958-961 (2016).

[124] H. Lin, Z. Luo, T. Gu, C. Kimerling Lionel, K. Wada, A. Agarwal, and J. Hu, "Mid-infrared integrated photonics on silicon: a perspective," Nanophotonics **7**, 393–420 (2017).

[125] S. Beecher, "The Ultrafast Laser Inscription of Photonic Devices for Integrated Optical Applications," (Heriot-Watt University, 2012).

[126] D. E. Spence, P. N. Kean, and W. Sibbett, "60-fsec pulse generation from a self-mode-locked Ti:sapphire laser," Optics Letters **16**, 42-44 (1991).

[127] M. Sheik-Bahae, A. A. Said, and E. W. Van Stryland, "High-sensitivity, single-beam n_2 measurements," Optics Letters **14**, 955-957 (1989).

[128] S. Friberg and P. Smith, "Nonlinear optical glasses for ultrafast optical switches," IEEE Journal of Quantum Electronics **23**, 2089-2094 (1987).

[129] M. Moran, S. Chiao-Yao, and R. Carman, "Interferometric measurements of the nonlinear refractive-index coefficient relative to CS_2 in laser-system-related materials," IEEE Journal of Quantum Electronics **11**, 259-263 (1975).

[130] K. S. Bindra, H. T. Bookey, A. K. Kar, B. S. Wherrett, X. Liu, and A. Jha, "Nonlinear optical properties of chalcogenide glasses: Observation of multiphoton absorption," Applied Physics Letters **79**, 1939-1941 (2001).

[131] B. Gu, Y. X. Fan, J. Chen, H. T. Wang, J. He, and W. Ji, "Z-scan theory of two-photon absorption saturation and experimental evidence," Journal of Applied Physics **102**, 083101 (2007).

[132] J. McCarthy, "Nonlinear Optical Processes in Bulk and Waveguide Structures in the Infrared," (Heriot-Watt University, 2013).

[133] J. M. Burzler, S. Hughes, and B. S. Wherrett, "Split-step Fourier methods applied to model nonlinear refractive effects in optically thick media," Applied Physics B - Lasers and Optics **62**, 389-397 (1996).

[134] J. Wang, B. Gu, X. W. Ni, and H. T. Wang, "Z-scan theory with simultaneous two- and three-photon absorption saturation," Optics and Laser Technology **44**, 390-393 (2012).

[135] T. Wang, X. Gai, W. Wei, R. Wang, Z. Yang, X. Shen, S. Madden, and B. Luther-Davies, "Systematic z-scan measurements of the third order nonlinearity of chalcogenide glasses," Optical Materials Express **4**, 1011-1022 (2014).

[136] G. Demetriou, J.-P. Bérubé, R. Vallée, Y. Messaddeq, C. R. Petersen, D. Jain, O. Bang, C. Craig, D. W. Hewak, and A. K. Kar, "Refractive index and dispersion control of ultrafast laser inscribed waveguides in gallium lanthanum sulphide for near and mid-infrared applications," Optics Express **24**, 6350 (2016).

[137] C. R. Petersen, U. Møller, I. Kubat, B. Zhou, S. Dupont, J. Ramsay, T. Benson, S. Sujecki, N. Abdel-Moneim, Z. Tang, D. Furniss, A. Seddon, and O. Bang, "Mid-infrared supercontinuum covering the 1.4–13.3 μm molecular fingerprint region using ultra-high NA chalcogenide step-index fibre," Nature Photonics **8**, 830-834 (2014).

[138] J. M. Morris, M. D. Mackenzie, C. R. Petersen, G. Demetriou, A. K. Kar, O. Bang, and H. T. Bookey, "$Ge_{22}As_{20}Se_{58}$ glass ultrafast laser inscribed waveguides for mid-IR integrated optics," Optical Materials Express **8**, 1001 (2018).

[139] J. Morris, G. Demetriou, A. Lancaster, A. Kar, and H. Bookey, "3D Optical Waveguides in Ge22As20Se58 Glass - a Highly Nonlinear Material for the Mid-IR," in *Conference on Lasers and Electro-Optics*, OSA Technical Digest (2016) (Optical Society of America, 2016), JTh2A.82.

[140] J. M. Morris, M. D. Mackenzie, C. R. Petersen, A. K. Kar, O. Bang, and H. T. Bookey, "Mid-IR Supercontinuum Generation in Ultrafast Laser Inscribed Waveguides," in

Conference on Lasers and Electro-Optics, OSA Technical Digest (online) (Optical Society of America, 2018), SM3D.2.

[141] T. M. Squires and S. R. Quake, "Microfluidics: Fluid physics at the nanoliter scale," Reviews of Modern Physics **77**, 977 (2005).

[142] M. Paolo, O. Roberto, S. Cinzia, S. Zhao, F. G. Omenetto, B. G. Kristinn, H. Tommy, Z. Yibo, O. Aydogan, W. Adam, M. Frieder, S. Holger, T. Genni, B. Romeo, G. Jochen, L. Carlo, B.-S. Kirstine, C. Jian, P. Markus, X. Sha, L. Ai-Qun, S. Chia-Chann, F. Shih-Kang, E. David, and S. David, "Roadmap for optofluidics," Journal of Optics **19**, 093003 (2017).

[143] E. K. Sackmann, A. L. Fulton, and D. J. Beebe, "The present and future role of microfluidics in biomedical research," Nature **507**, 181-189 (2014).

[144] R. Osellame, H. J. W. M. Hoekstra, G. Cerullo, and M. Pollnau, "Femtosecond laser microstructuring: an enabling tool for optofluidic lab-on-chips," Laser & Photonics Reviews **5**, 442-463 (2011).

[145] V. K. Jagannadh, M. D. Mackenzie, P. Pal, A. K. Kar, and S. S. Gorthi, "Imaging Flow Cytometry With Femtosecond Laser-Micromachined Glass Microfluidic Channels," IEEE Journal of Selected Topics in Quantum Electronics **21**, 1-6 (2015).

[146] F. Bragheri, P. Minzioni, R. Martinez Vazquez, N. Bellini, P. Paie, C. Mondello, R. Ramponi, I. Cristiani, and R. Osellame, "Optofluidic integrated cell sorter fabricated by femtosecond lasers," Lab Chip **12**, 3779-3784 (2012).

[147] A. M. Streets and Y. Huang, "Chip in a lab: Microfluidics for next generation life science research," Biomicrofluidics **7**, 11302 (2013).

[148] K. Sugioka, J. Xu, D. Wu, Y. Hanada, Z. Wang, Y. Cheng, and K. Midorikawa, "Femtosecond laser 3D micromachining: a powerful tool for the fabrication of microfluidic, optofluidic, and electrofluidic devices based on glass," Lab Chip **14**, 3447-3458 (2014).

[149] G. M. Whitesides, "The origins and the future of microfluidics," Nature **442**, 368-373 (2006).

[150] V. K. Jagannadh, M. D. Mackenzie, P. Pal, A. K. Kar, and S. S. Gorthi, "Slanted channel microfluidic chip for 3D fluorescence imaging of cells in flow," Optics Express **24**, 22144-22158 (2016).

[151] M. Haque and P. R. Herman, "Chemical-assisted femtosecond laser writing of optical resonator arrays," Laser & Photonics Reviews, 1-10 (2015).

[152] P. Paie, F. Bragheri, R. M. Vazquez, and R. Osellame, "Straightforward 3D hydrodynamic focusing in femtosecond laser fabricated microfluidic channels," Lab Chip **14**, 1826-1833 (2014).

[153] V. Maselli, J. R. Grenier, S. Ho, and P. R. Herman, "Femtosecond laser written optofluidic sensor: Bragg Grating Waveguide evanescent probing of microfluidic channel," Optics Express **17**, 11719-11729 (2009).

[154] T. Schweizer, B. N. Samson, R. C. Moore, D. W. Hewak, and D. N. Payne, "Rare-earth doped chalcogenide glass fibre laser," Electronics Letters **33**, 414-416 (1997).

[155] G. Demetriou, F. Thorburn, A. Lancaster, C. Craig, E. Weatherby, D. W. Hewak, and A. K. Kar, "Fluorescence in Erbium doped Gallium Lanthanum Sulphide: Potential for mid-IR waveguide laser," in *2015 Conference on Lasers and Electro-Optics (CLEO)*, 2015), 1-2.

[156] P. Bastock, C. Craig, K. Khan, E. Weatherby, J. Yao, and D. W. Hewak, "Properties of gallium lanthanum sulphide glass," in *CLEO: Science and Innovations*, (Optical Society of America, 2015), STh1G. 1.

[157] "GLS Infrared Transmitting Glass Datasheet," (2018).

[158] T. Gretzinger, S. Gross, M. Ams, A. Arriola, and M. J. Withford, "Ultrafast laser inscription in chalcogenide glass: thermal versus athermal fabrication," Optical Materials Express **5**, 2862 (2015).

[159] M. Vlček, S. Schroeter, J. Čech, T. Wágner, and T. Glaser, "Selective etching of chalcogenides and its application for fabrication of diffractive optical elements," Journal of Non-Crystalline Solids **326-327**, 515-518 (2003).

[160] J. Orava, T. Wagner, A. Krbal, T. Kohoutek, M. Vlcek, and M. Frumar, "Selective wet-etching and characterization of chalcogenide thin films in inorganic alkaline solutions," Journal of Non-Crystalline Solids **353**, 1441-1445 (2007).

[161] J. Orava, T. Wagner, M. Krbal, T. Kohoutek, M. Vlcek, P. Klapetek, and M. Frumar, "Selective dissolution of $Ag_x(As_{0.33}S_{0.67-y}Se_y)_{100-x}$ chalcogenide thin films," Journal of Non-Crystalline Solids **354**, 533-539 (2008).

[162] V. A. Dan'ko, I. Z. Indutnyi, V. I. Min'ko, P. E. Shepelyavyi, O. V. Bereznyova, and O. S. Lytvyn, "Photoinduced etching of thin films of chalcogenide glassy semiconductors," Semiconductors **46**, 504-508 (2012).

[163] A. Feigel, M. Veinger, B. Sfez, A. Arsh, M. Klebanov, and V. Lyubin, "Three-dimensional simple cubic woodpile photonic crystals made from chalcogenide glasses," Applied Physics Letters **83**, 4480-4482 (2003).

[164] A. Kovalskiy, J. Cech, M. Vlcek, C. M. Waits, M. Dubey, W. R. Heffner, and H. Jain, "Chalcogenide glass e-beam and photoresists for ultrathin grayscale patterning," Journal of Micro/Nanolithography, MEMS, and MOEMS **8**, 043012-043012-043011 (2009).

[165] L. Su, C. J. Rowlands, T. H. Lee, and S. R. Elliott, "Fabrication of photonic waveguides in sulfide chalcogenide glasses by selective wet-etching," Electronics Letters **44**, 472-473 (2008).

[166] L. Su, C. J. Rowlands, and S. R. Elliott, "Nanostructures fabricated in chalcogenide glass for use as surface-enhanced Raman scattering substrates," Optics Letters **34**, 1645-1647 (2009).

[167] S. Wong, M. Deubel, F. Perez-Willard, S. John, G. A. Ozin, M. Wegener, and G. von Freymann, "Direct laser writing of three-dimensional photonic crystals with complete a photonic bandgap in chalcogenide glasses," Advanced Materials **18**, 265-269 (2006).

[168] S. H. Wong, M. Thiel, P. Brodersen, D. Fenske, G. A. Ozin, M. Wegener, and G. von Freymann, "Highly selective wet etch for high-resolution three-dimensional nanostructures in arsenic sulfide all-inorganic photoresist," Chemistry of Materials **19**, 4213-4221 (2007).

[169] P. Török, P. Varga, Z. Laczik, and G. R. Booker, "Electromagnetic diffraction of light focused through a planar interface between materials of mismatched refractive indices: an integral representation," Journal of the Optical Society of America A **12**, 325 (1995).

[170] J. M. Morris, A. Kar, and H. Bookey, "Gallium Lanthanum Sulphide Glass for Ultrafast Laser Inscribed Optofluidic Devices," in *Photon 16*, (IOP, 2016),

[171] T. Calmano and S. Muller, "Crystalline Waveguide Lasers in the Visible and Near-Infrared Spectral Range," IEEE Journal of Selected Topics in Quantum Electronics **21**, 401-413 (2015).

[172] F. Chen and J. R. V. de Aldana, "Optical waveguides in crystalline dielectric materials produced by femtosecond-laser micromachining," Laser & Photonics Reviews **8**, 251-275 (2014).

[173] R. Yingying, G. Brown, R. Mary, G. Demetriou, D. Popa, F. Torrisi, A. C. Ferrari, C. Feng, and A. K. Kar, "7.8-GHz Graphene-Based Monolithic Waveguide Laser," IEEE Journal of Selected Topics in Quantum Electronics **21**, 395-400 (2015).

[174] F. Fusari, R. R. Thomson, G. Jose, F. M. Bain, A. A. Lagatsky, N. D. Psaila, A. K. Kar, A. Jha, W. Sibbett, and C. T. Brown, "Lasing action at around 1.9 μm from an ultrafast laser inscribed Tm-doped glass waveguide," Optics Letters **36**, 1566-1568 (2011).

[175] D. G. Lancaster, S. Gross, H. Ebendorff-Heidepriem, A. Fuerbach, M. J. Withford, and T. M. Monro, "2.1 μm waveguide laser fabricated by femtosecond laser direct-writing in Ho^{3+}, Tm^{3+}:ZBLAN glass," Optics Letters **37**, 996-998 (2012).

[176] B. M. Walsh, "Review of Tm and Ho materials; spectroscopy and lasers," Laser Physics **19**, 855-866 (2009).

[177] D. G. Lancaster, S. Gross, H. Ebendorff-Heidepriem, M. J. Withford, T. M. Monro, and S. D. Jackson, "Efficient 2.9 μm fluorozirconate glass waveguide chip laser," Optics Letters **38**, 2588-2591 (2013).

[178] Y. Ren, G. Brown, A. Rodenas, S. Beecher, F. Chen, and A. K. Kar, "Mid-infrared waveguide lasers in rare-earth-doped YAG," Optics Letters **37**, 3339-3341 (2012).

[179] J. R. Macdonald, S. J. Beecher, P. A. Berry, G. Brown, K. L. Schepler, and A. K. Kar, "Efficient mid-infrared Cr:ZnSe channel waveguide laser operating at 2486 nm," Optics Letters **38**, 2194-2196 (2013).

[180] A. A. Lagatsky, X. Han, M. D. Serrano, C. Cascales, C. Zaldo, S. Calvez, M. D. Dawson, J. A. Gupta, C. T. Brown, and W. Sibbett, "Femtosecond (191 fs) $NaY(WO_4)_2$ Tm,Ho-codoped laser at 2060 nm," Optics Letters **35**, 3027-3029 (2010).

[181] D. P. Shepherd, A. Choudhary, A. A. Lagatsky, P. Kannan, S. J. Beecher, R. W. Eason, J. I. Mackenzie, X. Feng, W. Sibbett, and C. T. A. Brown, "Ultrafast High-Repetition-Rate Waveguide Lasers," IEEE Journal of Selected Topics in Quantum Electronics **22**, 16-24 (2016).

[182] S. Juodkazis, H. Misawa, and I. Maksimov, "Thermal accumulation effect in three-dimensional recording by picosecond pulses," Applied Physics Letters **85**, 5239-5241 (2004).

[183] J. A. Caird, S. A. Payne, P. Staber, A. Ramponi, L. Chase, and W. F. Krupke, "Quantum electronic properties of the $Na_3Ga_2Li_3F_{12}$: Cr^{3+} laser," IEEE Journal of Quantum Electronics **24**, 1077-1099 (1988).

[184] R. Mary, S. J. Beecher, G. Brown, R. R. Thomson, D. Jaque, S. Ohara, and A. K. Kar, "Compact, highly efficient ytterbium doped bismuthate glass waveguide laser," Optics Letters **37**, 1691-1693 (2012).

[185] J. Morris, N. K. Stevenson, H. T. Bookey, A. K. Kar, C. T. A. Brown, J. M. Hopkins, M. D. Dawson, and A. A. Lagatsky, "1.9 μm waveguide laser fabricated by ultrafast laser inscription in Tm:Lu_2O_3 ceramic," Optics Express **25**, 14910 (2017).

[186] N. K. Stevenson, J. Morris, H. T. Bookey, A. K. Kar, C. T. A. Brown, J. M. Hopkins, M. D. Dawson, and A. A. Lagatsky, "Waveguide Tm:Lu_2O_3 ceramic laser fabricated by ultrafast laser inscription," in *European Conference on Lasers and Electro-Optics - European Quantum Electronics Conference,* (OSA, Munich, Germany, 2017).

[187] D. G. Lancaster, S. Gross, H. Ebendorff-Heidepriem, K. Kuan, T. M. Monro, M. Ams, A. Fuerbach, and M. J. Withford, "Fifty percent internal slope efficiency femtosecond direct-written Tm^{3+}:ZBLAN waveguide laser," Optics Letters **36**, 1587-1589 (2011).